

Technical Report No. 32-834

*A Study of Secondary Injection of Gases Into
a Supersonic Flow*

*F. W. Spaid
E. E. Zukoski
R. Rosen*

FACILITY FORM 802

N66 32724
(ACCESSION NUMBER)

86
(PAGES)

CR-76891
(NASA CR OR TMX OR AD NUMBER)

(THRU)

(CODE)

12
(CATEGORY)

GPO PRICE \$ _____

CFSTI PRICE(S) \$ _____

Hard copy (HC) 2.50

Microfiche (MF) 1.75

ff 653 July 65



**JET PROPULSION LABORATORY
CALIFORNIA INSTITUTE OF TECHNOLOGY
PASADENA, CALIFORNIA**

August 1, 1966

Copyright © 1966
Jet Propulsion Laboratory
California Institute of Technology

Prepared Under Contract No. NAS 7-100
National Aeronautics & Space Administration

NATIONAL AERONAUTICS AND SPACE ADMINISTRATION

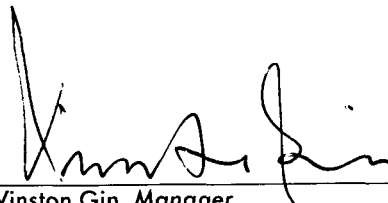
Technical Report No. 32-834

*A Study of Secondary Injection of Gases Into
a Supersonic Flow*

F. W. Spaid

E. E. Zukoski

R. Rosen

A handwritten signature in black ink, appearing to read 'Winston Gin', is written over a horizontal line.

Winston Gin, Manager
Solid Propellant Engineering Section

JET PROPULSION LABORATORY
CALIFORNIA INSTITUTE OF TECHNOLOGY
PASADENA, CALIFORNIA

August 1, 1966

FOREWORD

This Report presents the results of one phase of research conducted at the Jet Propulsion Laboratory for the National Aeronautics and Space Administration. The experiments reported were performed in the supersonic-wind-tunnel facilities at both the Jet Propulsion Laboratory and the California Institute of Technology. The work in part grew out of earlier experiments at JPL on thrust-vector control in rocket exhaust nozzles.¹ Results of those experiments pointed out the need for more detailed information concerning the interaction that occurs when a small secondary stream of gas is injected into a large supersonic flow. It was felt desirable to simplify the geometry so that the complex interaction phenomena could be studied in as simple a manner as possible. Hence, the interaction was studied by examining secondary injection into a uniform and supersonic flow over a flat plate or plane wall.

At the time this work was performed, Dr. F. W. Spaid was a graduate student at Caltech, and Mr. R. Rosen was employed at JPL. Dr. Spaid is now a member of the technical staff at Douglas Aircraft Company, Inc., Santa Monica, California, and Mr. Rosen is a graduate student at the University of Southern California. Dr. E. E. Zukoski is Professor of Jet Propulsion at the California Institute of Technology.

¹Ref. 16 of this Report.

CONTENTS

I. Introduction	1
II. Description of Experiments	2
III. Description of the Flow Field	4
IV. Analytic Model	12
V. Presentation of Experimental Data	15
A. Penetration Height	15
B. Shock Shapes	17
C. Concentration Profiles	21
D. Velocity and Total-Pressure Profiles	28
E. Wall-Pressure Distribution	30
F. Helium Injection	47
G. Scaling of Other Published Data	47
H. Two-Hole Injectors	53
VI. Discussion and Conclusions	61
A. Review of Flow Models	61
B. Review of the Flow-Field Characteristics	62
C. Applications of the Scaling Law to Scaling of Forces	63
Nomenclature	67
References	68

FIGURES

1. Typical Mach number profiles in the test section near the injector, no injection; Caltech supersonic wind tunnel	2
2. Section view of circular-hole injector	3
3a. Sketch of the flow field for hole injection, turbulent boundary layer	5
3b. Sketch of the flow field for hole injection, laminar boundary layer	5
3c. Schlieren photograph, nozzle wall; $M_\infty = 2.56$, $Re = 2.5 \times 10^5$ per in.; turbulent boundary layer	6
3d. Schlieren photograph, nozzle wall; $M_\infty = 2.56$, $Re = 1.3 \times 10^5$ per in.; laminar boundary layer	6

FIGURES (Cont'd)

4. Shadowgraph photographs, flat-plate test	7-12
5. Schematic diagrams of flow field for the model used in calculations	13
6. Penetration of secondary jet into primary flow, nozzle-wall data	16
7. Penetration of secondary jet into primary flow, flat-plate data	17
8. Shock shapes; comparison of nozzle-wall and flat-plate results	18
9. Shock shapes showing Mach number effect	18
10a. Linear comparison of normalized dimensions of shock shapes, showing axisymmetry of shock with three-dimensional injection; $M_\infty = 2.61$	19
10b. Polar plot of ratio of normalized shock dimensions from Fig. 10a as functions of position in injectant-plume cross section	19
10c. Comparison of off-centerline shock radii with centerline shock shapes measured from schlieren pictures (reference); $M_\infty = 2.61$	19
11a. Concentration measurements in the plane $(y/h) = 0$, injector region, with argon as injectant	20
11b. Concentration measurements in the plane $(y/h) = 0$, downstream region, with argon as injectant	21
12. Concentration profiles in several planes; $(y/h) = \text{constant}$, $M_\infty = 2.56$, $P_{0\infty} = 0.97 \text{ atm}$	22
13. Crossplots of argon-concentration profiles in planes for which $(z/h) = \text{constant}$, $M_\infty = 2.56$, $P_{0\infty} = 0.97 \text{ atm}$	23
14. Concentration contours in the planes $(x/h) = 2.08$ and $(x/h) = 12.3$; $M_\infty = 2.56$; $P_{0\infty} = 0.97 \text{ atm}$	24
15a. Concentration measurements in the plane $(y/h) = 0$, with helium as injectant	24
15b. Comparison of argon and helium concentration data	25
16. Concentration, total-pressure, and velocity profiles in the plane $(y/h) = 0$, flat-plate data, turbulent boundary layer	26, 27
17. Velocity, Mach number, and total-pressure profiles with argon as injectant for $(x/h) = 8.49$; $M_\infty = 2.61$; $V_\infty = 585 \text{ m/sec}$; $P_{0\infty} = 73.69 \text{ cm Hg}$; $(P_{0j}/P_{0\infty}) = 7.77$; and $h = 0.5202 \text{ cm}$	28
18. Velocity profiles with argon as injectant for $(x/h) = 10.49$; $M_\infty = 2.61$; $V_\infty = 585 \text{ m/sec}$; $P_{0\infty} = 73.69 \text{ cm Hg}$; $(P_{0j}/P_{0\infty}) = 7.77$; and $h = 0.5202 \text{ cm}$	28
19. Velocity and total-pressure profiles with argon as injectant and velocity profiles without injection for $(x/h) = 12.49$; $M_\infty = 2.61$; $V_\infty = 585 \text{ m/sec}$; $P_{0\infty} = 73.69 \text{ cm Hg}$; $(P_{0j}/P_{0\infty}) = 7.77$; and $h = 0.5202 \text{ cm}$	29

FIGURES (Cont'd)

20. Velocity profiles with argon as injectant for $(x/h) = 15.49$; $M_\infty = 2.61$; $V_\infty = 585$ m/sec; $P_{0_\infty} = 73.69$ cm Hg; $(P_{0_j}/P_{0_\infty}) = 7.77$; and $h = 0.5202$ cm	29
21. Concentration and total-pressure contours with argon as injectant; $M_\infty \approx 2.61$; $P_{0_\infty} = 0.974$ atm; $(P_{0_j}/P_{0_\infty}) = 7.77$; $h \approx 0.52$ cm; $(x/h) \approx 12$	30
22a. Pressure map for flat-plate measurements at $M_\infty = 2.61$ with nitrogen as injectant; turbulent boundary layer	31
22b. Flat-plate static-pressure measurements in the plane $(y/h) = 0$ with nitrogen as injectant; turbulent boundary layer	32
23. Flat-plate static-pressure measurements in the plane $(y/h) = 0$ at $M_\infty = 2.61$ with nitrogen as injectant; turbulent boundary layer	32
24. Nozzle-wall static-pressure measurements in the plane $(y/h) = 0$ with nitrogen and helium as injectant	33
25. Nozzle-wall static-pressure measurements in off-axis planes with nitrogen as injectant, $(y/h) = \text{constant}$	34
26. Nozzle-wall static-pressure measurements in off-axis planes with nitrogen as injectant, $(x/h) = \text{constant}$	34
27. Flat-plate static-pressure measurements in the plane $(y/h) = 0$ at $M_\infty = 2.01$ with nitrogen as injectant; turbulent boundary layer	34
28. Flat-plate static-pressure measurements in the plane $(y/h) = 0$ at $M_\infty = 2.61$ with nitrogen as injectant; laminar boundary layer	35
29. Flat-plate static-pressure measurements in the plane $(y/h) = 0$ at $M_\infty = 3.50$; turbulent boundary layer	35
30. Flat-plate static-pressure measurements in the plane $(y/h) = 0$ at $M_\infty = 3.50$ with nitrogen as injectant; laminar boundary layer	36
31. Flat-plate static-pressure measurements in the plane $(y/h) = 0$ at $M_\infty = 4.54$ with nitrogen as injectant; turbulent boundary layer	37
32. Flat-plate static-pressure measurements in the plane $(y/h) = 0$ at $M_\infty = 4.54$ with nitrogen as injectant; laminar boundary layer	38
33. Pressure map for flat-plate measurements at $M_\infty = 2.61$ with nitrogen as injectant; laminar boundary layer	39
34. Pressure map for flat-plate measurements at $M_\infty = 3.50$ with nitrogen as injectant; turbulent boundary layer	40
35. Pressure map for flat-plate measurements at $M_\infty = 3.50$ with nitrogen as injectant; laminar boundary layer	41
36. Pressure map for flat-plate measurements at $M_\infty = 4.54$ with nitrogen as injectant; turbulent boundary layer	42
37. Flat-plate static-pressure measurements in the plane $(y/h) = 0$ with nitrogen as injectant, turbulent boundary layer; data for small-diameter injector	43, 44

FIGURES (Cont'd)

38. Flat-plate static-pressure measurements in the plane $(y/h) = 0$ at $M_\infty = 2.61$ with nitrogen as injectant, turbulent boundary layer, showing effect of changing injector diameter	45
39a. Flat-plate static-pressure measurements in the plane $(y/h) = 0$ at $M_\infty = 2.61$ with nitrogen as injectant, turbulent boundary layer, showing effect of changing injector diameter when penetration distance is held fixed	45
39b. Pressure measurements in off-axis planes for conditions given in Fig. 39a	46
40. Flat-plate static-pressure measurements in the plane $(y/h) = 0$ at $M_\infty = 3.50$ with nitrogen as injectant, turbulent boundary layer, showing effect of changing injector diameter when penetration distance is held fixed	46
41. Effect of injectant properties on flat-plate static-pressure measurements in the plane $(y/h) = 0$ at $M_\infty = 2.61$ with nitrogen and helium as injectant; turbulent boundary layer	47
42a. Effect of injectant properties on flat-plate static-pressure measurements in the plane $(y/h) = 0$ at $M_\infty = 3.50$ with nitrogen and helium as injectant; turbulent boundary layer	48
42b. Pressure measurements in off-axis planes for conditions given in Fig. 42a	48
43. Effect of injectant properties on flat-plate static-pressure measurements in the plane $(y/h) = 0$ at $M_\infty = 3.50$ with nitrogen and helium as injectant; turbulent boundary layer	49
44. Pressure map for flat-plate measurements at $M_\infty = 2.61$ with helium as injectant; turbulent boundary layer	50
45. Pressure map for flat-plate measurements at $M_\infty = 3.50$ with helium as injectant; turbulent boundary layer	51
46. Pressure map for flat-plate measurements at $M_\infty = 3.50$ with helium as injectant; laminar boundary layer	52
47. Correlation of pressure data from Ref. 9	53
48. Shadowgraph photographs; flat-plate data; double-hole injectors	54, 55
49. Pressure map for flat-plate measurements at $M_\infty = 2.61$ with nitrogen as injectant; turbulent boundary layer; injection through two holes	56
50. Flat-plate static-pressure measurements in the plane $(y/h) = 0$ at $M_\infty = 2.61$ with nitrogen as injectant; turbulent boundary layer; injection through two holes, with the x-axis aligned with the centerline of one hole	57
51. Flat-plate static-pressure measurements in the plane $(y/h) = 0$ at $M_\infty = 2.61$ with nitrogen as injectant; turbulent boundary layer; injection through two holes, with the x-axis aligned with the centerline of one hole	57

FIGURES (Cont'd)

52. Pressure map for flat-plate measurements at $M_\infty = 4.54$ with nitrogen as injectant; injection through two holes; turbulent boundary layer	58
53. Pressure map for flat-plate measurements at $M_\infty = 4.54$ with nitrogen as injectant; injection through two holes; turbulent boundary layer	59
54. Pressure map for flat-plate measurements at $M_\infty = 4.54$ with helium as injectant; injection through two holes; turbulent boundary layer	60
55. Variation of side specific impulse with normalized distance from injector to nozzle exit	62
56. Correlation of rocket-motor thrust-vector-control performance for different gases and temperatures (from Ref. 21)	65
57. Correlation of rocket-motor thrust-vector-control data (from Ref. 22)	65
58. Correlation of rocket-motor thrust-vector-control data (from Ref. 17), present method	65
59. Correlation of rocket-motor thrust-vector-control data, method of Broadwell (from Ref. 23)	66

ABSTRACT

N66-32724

The flow field around the injection port for secondary injection of a gas normal to a supersonic stream has been studied in a series of wind-tunnel experiments. The experiments were conducted at free-stream Mach numbers of 1.38 to 4.54. Gaseous nitrogen, argon, and helium were injected through a circular hole and sonic flow was maintained at the injection orifice. Data presented include static-pressure distributions on the wall in the region of the injector, shock shapes, and injectant-mass-fraction, total-pressure, and velocity profiles downstream of the injector. A scale parameter has been calculated, based on a simple, inviscid model of the flow field. This scale parameter gives a good general correlation of the data. Use of this scale parameter allows the prediction of a simple scaling law for the normal forces on a wall produced by secondary injection, which is in approximate agreement with existing rocket-motor test results.

Author

I. INTRODUCTION

The description of the flow field set up by the injection of a secondary gas into a supersonic primary flow is a problem of current engineering interest. Flows of this type occur during thrust-vector control of rocket motors, during jet-reaction attitude control of vehicles moving through the atmosphere, and during fuel injection into a supersonic burner.

In all of these applications, when a gas is injected into the primary flow, a high-pressure region is set up on the wall in the neighborhood of the injector. The detailed mechanism that governs the magnitude of the resulting force on the wall is not yet thoroughly understood, but may be roughly described as follows. The injected material must be turned by the primary flow. Because the injectant acts as an obstruction it produces a strong shock wave in the primary flow. This shock interacts with the boundary layer on the wall and may cause it to separate. Both the initial shock and the resulting boundary-layer separation produce a region of high pressure near the point of injection. Further pressure changes may be produced further downstream by mixing of the primary and

secondary flows, and by expansion of the primary flow as it passes around the obstacle formed by the injectant.

The goal of the present study has been to obtain fundamental information concerning the processes of interaction that occur during secondary injection and, in particular, to determine similarity rules for the important phenomena. The situation chosen for experimental and theoretical study is the sonic injection of a gas through a wall and perpendicular to a primary flow that is uniform and rectilinear outside a wall boundary layer. The parameters changed during the tests include primary-flow Mach number, injector size, and injectant-composition and stagnation-pressure ratio. A model for the interaction region is presented and is compared with experimental data obtained by the authors and by other workers.

In addition to the work carried out with a single-hole injector, some information was also obtained with two-hole injectors.

II. DESCRIPTION OF EXPERIMENTS

Experiments were carried out in facilities at the California Institute of Technology (Caltech) and at the Jet Propulsion Laboratory (JPL). The series of experiments conducted at the California Institute of Technology were carried out in the 2.5-in. supersonic wind tunnel, which is described in detail in Ref. 1. The test section is 2.5 in. wide and about 2 in. high.

During these experiments, gaseous nitrogen, argon, and helium were injected through orifices in the test-section side walls. Test-section conditions consisted of Mach numbers 2.56 and 1.38, and Reynolds numbers per inch of 1.3×10^5 to 4.3×10^5 at the first Mach number and 4.5×10^5 at the second. At the Mach number 2.56 and below a Reynolds number per inch of 1.7×10^5 , the boundary layer on the test-section wall was found to be laminar; above that Reynolds number it was turbulent at the same Mach number. The tunnel could maintain quasi-steady-state flow in the test section at a Mach number of 1.38 for only approximately 10 sec. It was possible to perform experiments only at a single free-stream stagnation pressure, and therefore only at a single Reynolds number per inch. This Reynolds number resulted in a turbulent boundary layer in the region of the injection port.

Because of the very short test-time duration at the lower Mach number, surveys of the undisturbed flow in the test section were carried out only at the higher Mach number. Figure 1 shows Mach number profiles obtained at two axial stations in the test section for an intermediate Reynolds number that corresponded to a free-stream stagnation pressure of approximately 1 atm. These measurements were made in a plane equidistant from both of the glass side-walls of the test section and perpendicular to the wall containing the injector. The authors believe that these profiles are representative of the uniformity of the flow that existed for all of the tests, although a variation in test-section Mach number of the order of $\pm 1\%$ was observed when the nozzle blocks were removed and replaced for the purpose of changing injectors. Examination of schlieren pictures for various values of test-section Reynolds number indicated that the boundary-layer thickness exhibited by the profiles of Fig. 1, approximately 0.5 cm, is the correct order of magnitude for all of the test conditions. The data in Fig. 1 were obtained with a probe made from 0.065-in.-O.D. tubing, flattened and ground at one end to a tip that was approximately 0.10 in. wide by 0.006 in. high, with a hole 0.002 in.

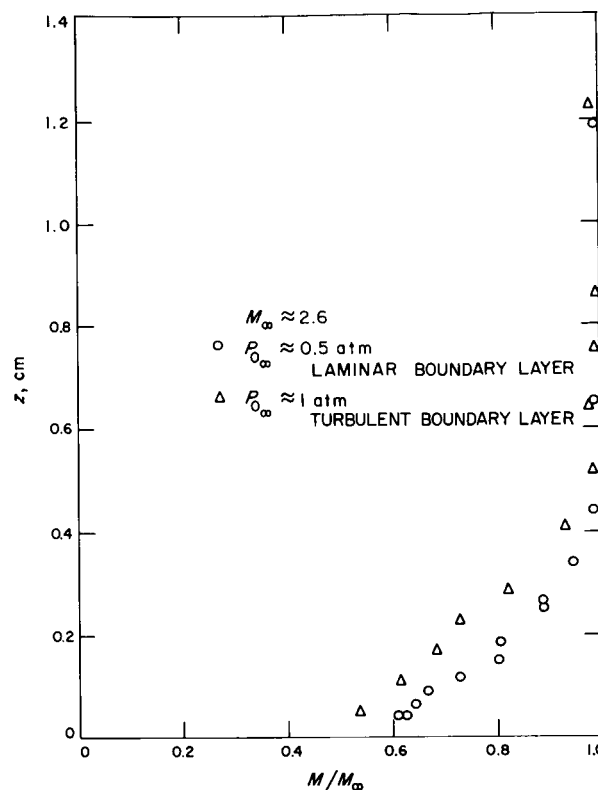


Fig. 1. Typical Mach number profiles in the test section near the injector, no injection; Caltech supersonic wind tunnel

high. Probe pressure was measured with a mercury manometer.

The experimental data collected during the tests with secondary injection consisted of test-section flow conditions, schlieren photographs, static-pressure distributions on the test-section wall in the region of injection, concentration and total-pressure measurements in the flow downstream of the injection port, and the injectant total pressure and mass flow rate. The static pressures were measured by mercury manometers, and the concentration measurements were obtained with a total-pressure probe and a Gow-Mac thermal conductivity cell. The total-pressure probe used for the concentration and total-pressure measurements for injection through a circular hole was a three-pronged probe with tips spaced 0.125 in. apart. The tips were circular, with a 0.031-in. O.D. and a 0.013 in.-diam. hole. The total-pressure profiles and the velocity profiles presented in this Report were obtained by H. Burden, and are reported in more detail in Ref. 2.

A section view of the circular-hole injector used for the majority of these experiments is shown in Fig. 2. The section is taken in a plane parallel to the test-section flow, the same one in which the Mach number and boundary-layer profiles of Fig. 1 were obtained. It can be seen in Fig. 2 that static-pressure taps were located on the wall as close to the injector as possible. One other injector, having a diameter of 0.114 in. and a configuration quite similar to that shown in Fig. 2, was also used, although the nozzle-block section in which this injector was installed was not instrumented with static-pressure taps. Discharge coefficients for each of these orifices were determined experimentally, and the injection pressures were corrected for losses caused by friction in the injector supply tube.

In addition to the experiments at Caltech, two series of experiments were conducted in the 20-in. supersonic wind tunnel at JPL. The first of these was part of a series of experiments conducted by M. W. Dowdy and J. F. Newton, Jr., (Ref. 3) in conjunction with the authors; the second was conducted by the authors alone.

In the first tests at JPL, gaseous nitrogen was injected through a sonic orifice 0.100 in. in diameter and normal to the surface of a sharp-edged flat plate. The orifice was located 7.00 in. to the rear of the leading edge. The surface of the plate in which the injector was located was

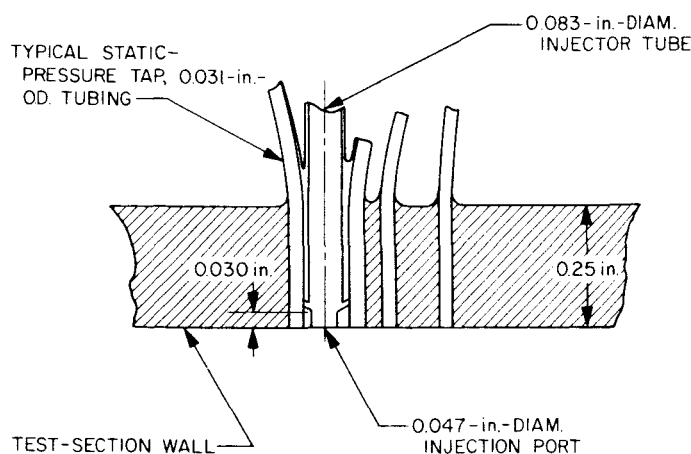


Fig. 2. Section view of circular-hole injector

parallel to the test-section flow, and a boundary-layer trip wire was attached near the leading edge of the plate. Tests were conducted at test-section Mach numbers of 4.54, 3.50, 2.61, and 2.01. The highest and the lowest practical tunnel stagnation pressures were utilized at each Mach number in an attempt to study the effect of test-section Reynolds number at a fixed Mach number. Reynolds numbers based upon the distance from the injection port to the leading edge covered the range 0.75×10^6 to 2.2×10^6 . In this test series, the experimental data consisted of schlieren and shadowgraph pictures, tunnel and injection conditions, and static-pressure measurements on the plate along a single line parallel to the flow and passing through the injector. The static pressures were measured by single transducers and a pressure-switching mechanism. Further details concerning the experimental apparatus and procedure are available in Ref. 3, and a description of the wind-tunnel facilities of the Jet Propulsion Laboratory is given in Ref. 4.

In the second test series at JPL, a similar flat plate was used, except that the static-pressure taps were distributed over a wide area around the injector ports. Nitrogen gas was the principal injectant, and data were also obtained with helium. The Mach numbers used were 2.61, 3.50, and 4.54, and both laminar and turbulent boundary layers were obtained at each Mach number. Data taken included schlieren and shadowgraph photographs, static-pressure measurements, and a few measurements of concentration profiles in the flow. In addition to data obtained with a single hole, some tests were carried out with two holes in order to study briefly the interaction of the two injectors.

Unfortunately, no boundary-layer profiles were taken in the JPL facility. Information concerning the boundary-layer thickness was obtained from shadowgraph photographs and from previous tests of similar flat plates in the same tunnel. Furthermore, the trip wire used on the plate and the well-known difficulties in interpretation of shadowgraph photographs make the results rather uncertain. Estimated values of the boundary-layer thickness at the injector location were 0.35 cm and 0.40 cm for the turbulent-flow conditions at Mach numbers of 2.61 and 3.50, respectively.

III. DESCRIPTION OF THE FLOW FIELD

A sketch of the flow field produced by injection through an orifice has been obtained by examination of schlieren and shadowgraph pictures of the interaction region. Figures 3a and 3b are scale drawings of two shadowgraph pictures taken at different free-stream stagnation pressures, but at the same ratio of jet stagnation pressure to free-stream stagnation pressure. The free-stream Mach number was 2.61 and the JPL flat-plate model was used here. Schlieren photographs of similar flow situations, taken in the Caltech facility, are shown in Fig. 3c and 3d. The injected material enters through a circular orifice with a static pressure much higher than the value in the undisturbed primary flow. The flow is sonic at the injector and expands rapidly through a strong Prandtl-Meyer fan. The interaction of the two streams produces a strong bow wave on the upstream side of the injector, and the shock-induced pressure field turns the injectant so that it moves approximately parallel to the wall.

The interaction of the bow shock wave with the boundary layer produces a region of boundary-layer separation upstream of the shock. For the case of a turbulent boundary layer, illustrated in Fig. 3a and 3c, the separated region is short, and the oblique shock produced by separation is often too weak to be observed. When the boundary layer is laminar, Fig. 3b and 3d, the separated region is much larger, and the angle between the separated flow and the wall is never more than a few degrees.

Some details of the flow near the injector are shown on the schlieren photographs. One feature which can be usually seen, e.g., Fig. 3c and 3d, and which is apparently the region of maximum concentration of the injectant, has the appearance of a streamline of the injectant. Determination of the maximum distance between this feature and the wall, later called the penetration height, gives a simple visual measure of the penetration of the secondary fluid into the primary flow. This feature is illustrated in Fig. 3a and 3b. The photographs in Fig. 3c and 3d illustrate flow conditions in which the distance of this feature from the wall is much greater than a characteristic boundary-layer dimension.

Under most conditions studied, the flow field is apparently steady; however, the separation process can be easily perturbed, and for high Mach numbers and laminar conditions some evidence of unsteady flows was observed. This unsteady behavior has also been reported by Amick and Hayes (Ref. 5).

A series of shadowgraph photographs taken during the first series of tests at the Jet Propulsion Laboratory has been published in Ref. 3, and a second group of pictures taken during the second test is presented here as Fig. 4a-4k. These photographs cover the range of test conditions discussed in this Report and include a set of pictures taken with no injection. These were used in making the determination of the boundary-layer thickness discussed at the end of Section II.

The change in shock structure produced by decreasing the injectant pressure ratio is illustrated in Fig. 4b-4e. These were obtained with nitrogen injectant and a turbulent boundary layer. In Fig. 4b, the scale of the disturbance is a maximum and hence the details of the flow are most clearly visible. In particular, note the shock structure and the turbulent motion of the gas in the neighborhood of the injector.

Figure 4f was taken with helium as injectant; hence comparison of this photograph with Fig. 4e indicates the influence of molecular weight and specific heat ratio on the interaction phenomena. The wavy shock shape in Fig. 4f is due to instability in the separation region and not to the properties of the injectant.

Injection with a laminar boundary layer is illustrated by Fig. 4h. The separation shock is too weak to be visible in this photograph, but comparison of Fig. 4h with the corresponding tare photograph, Fig. 4g, shows that the separation started at about -5 cm. Finally, the shock structure induced by injection of nitrogen at Mach 3.50 is shown in Fig. 4i and 4j, and the tare photograph for Mach number 4.54 is shown in Fig. 4k.

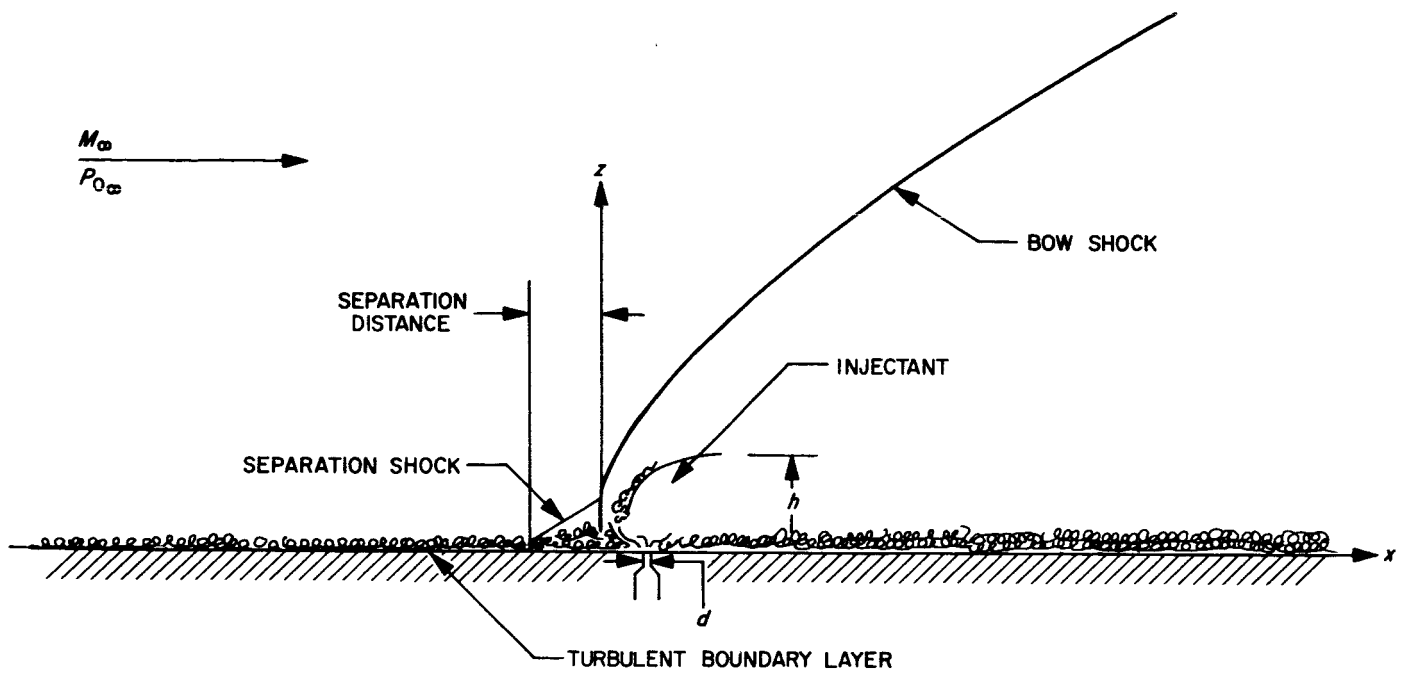


Fig. 3a. Sketch of the flow field for hole injection, turbulent boundary layer

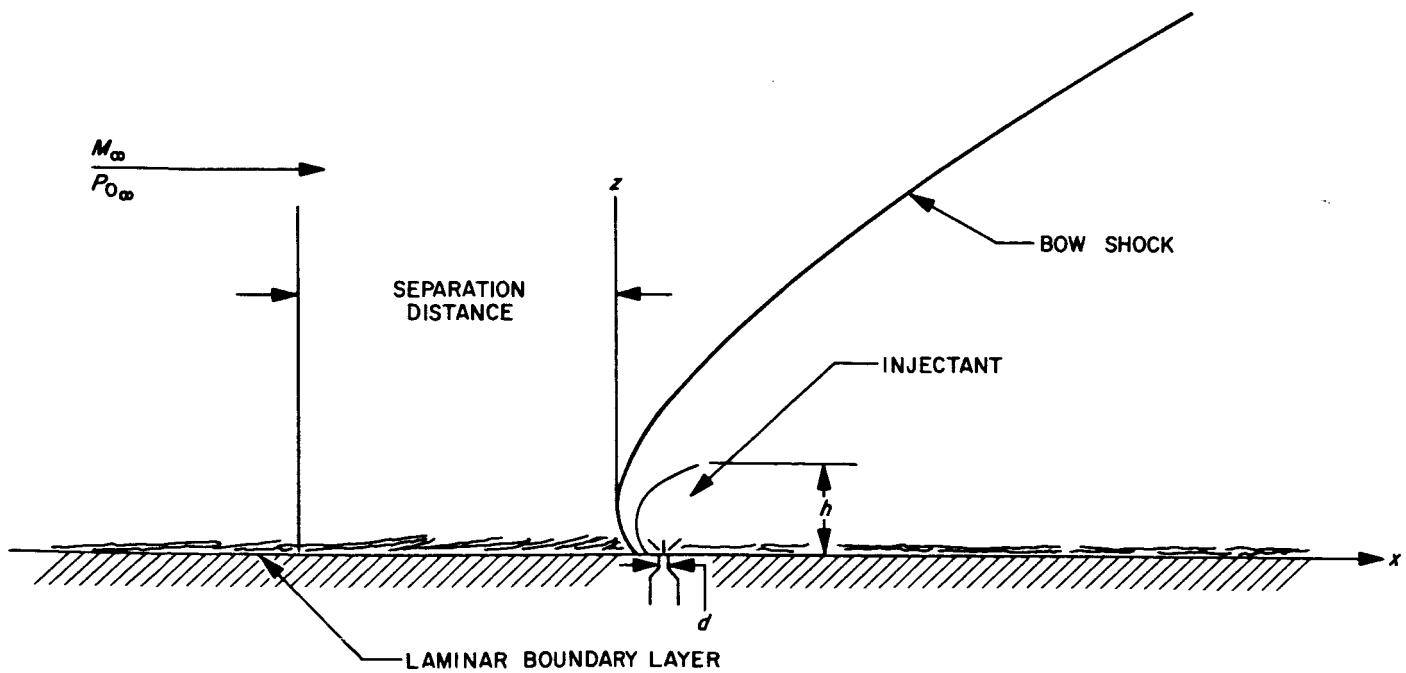


Fig. 3b. Sketch of the flow field for hole injection, laminar boundary layer

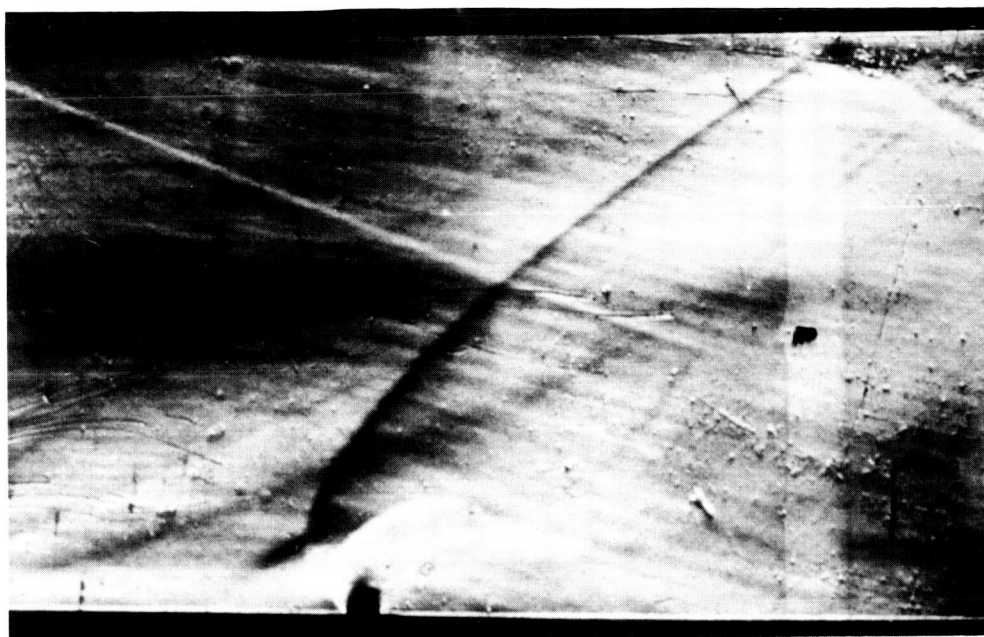


Fig. 3c. Schlieren photograph, nozzle wall; $M_\infty = 2.56$,
 $Re = 2.5 \times 10^5$ per in.; turbulent boundary layer

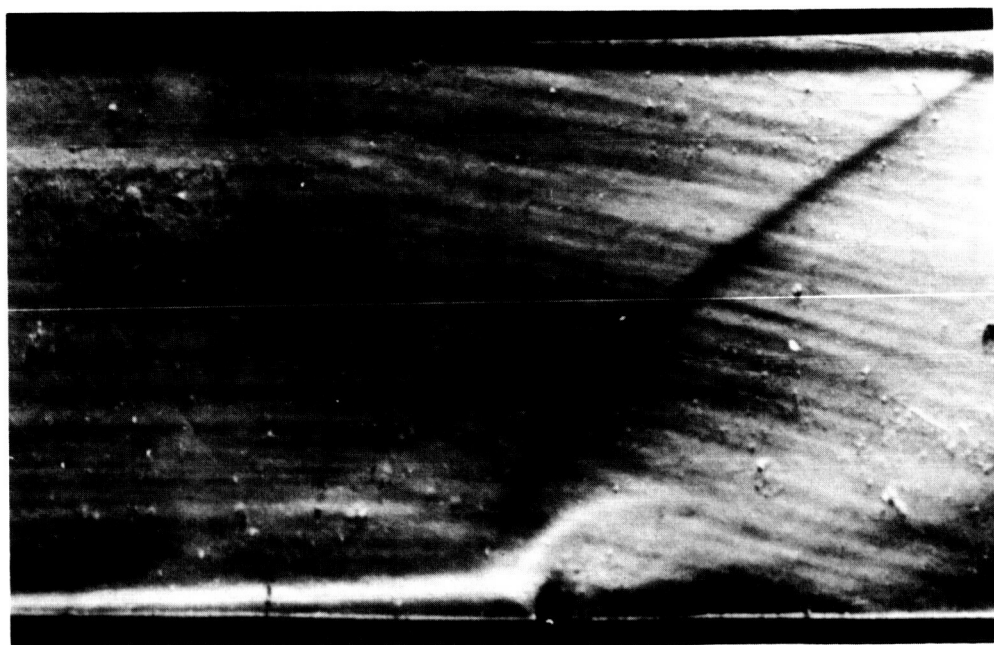


Fig. 3d. Schlieren photograph, nozzle wall; $M_\infty = 2.56$,
 $Re = 1.3 \times 10^5$ per in.; laminar boundary layer

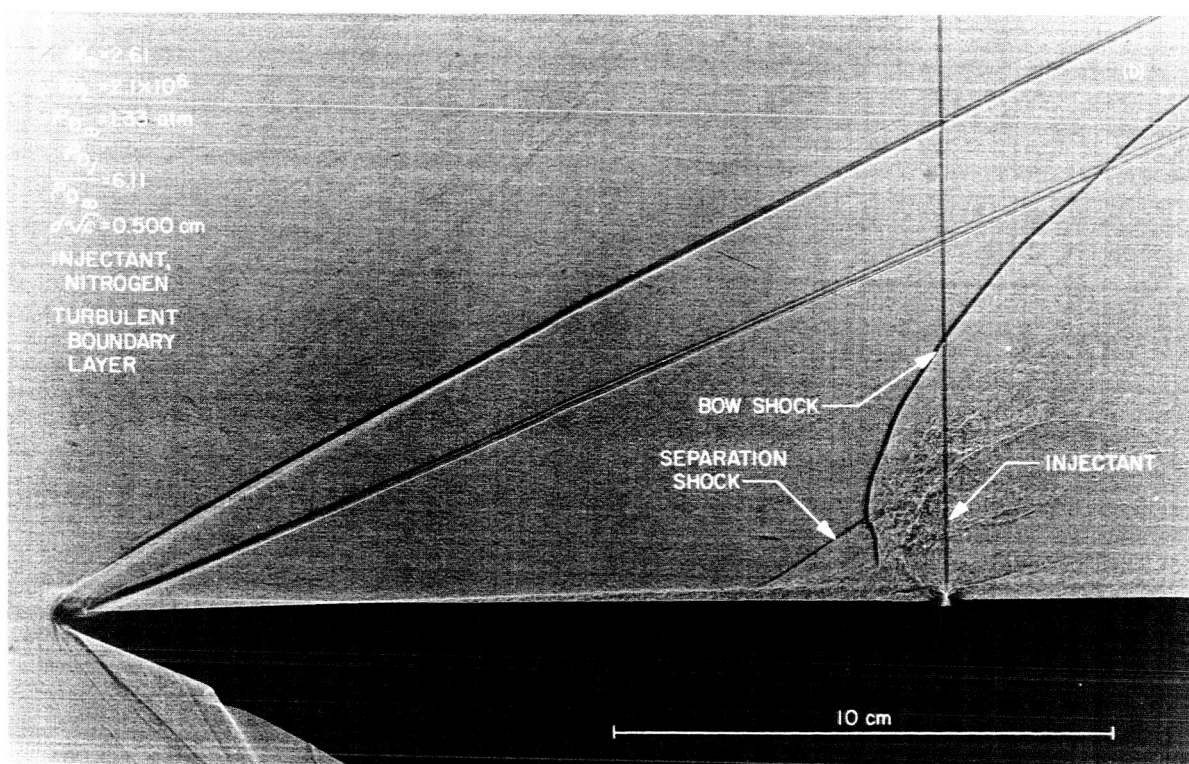
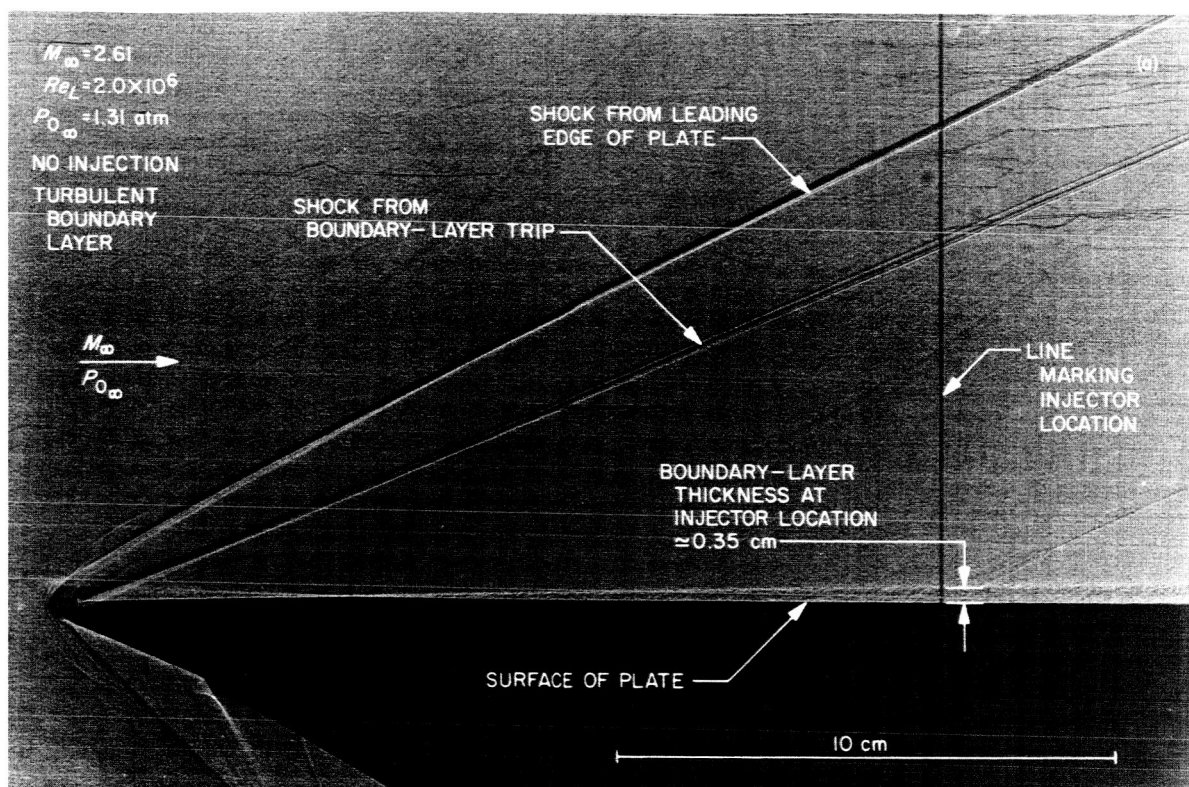


Fig. 4. Shadowgraph photographs, flat-plate test

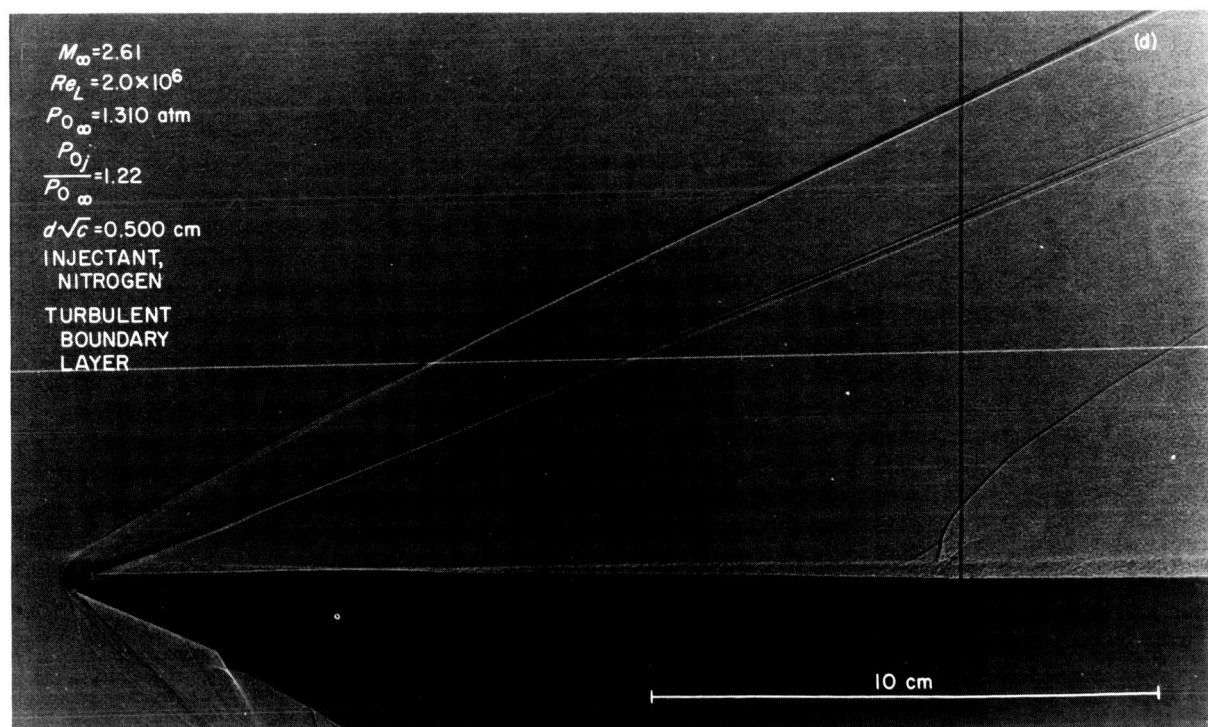
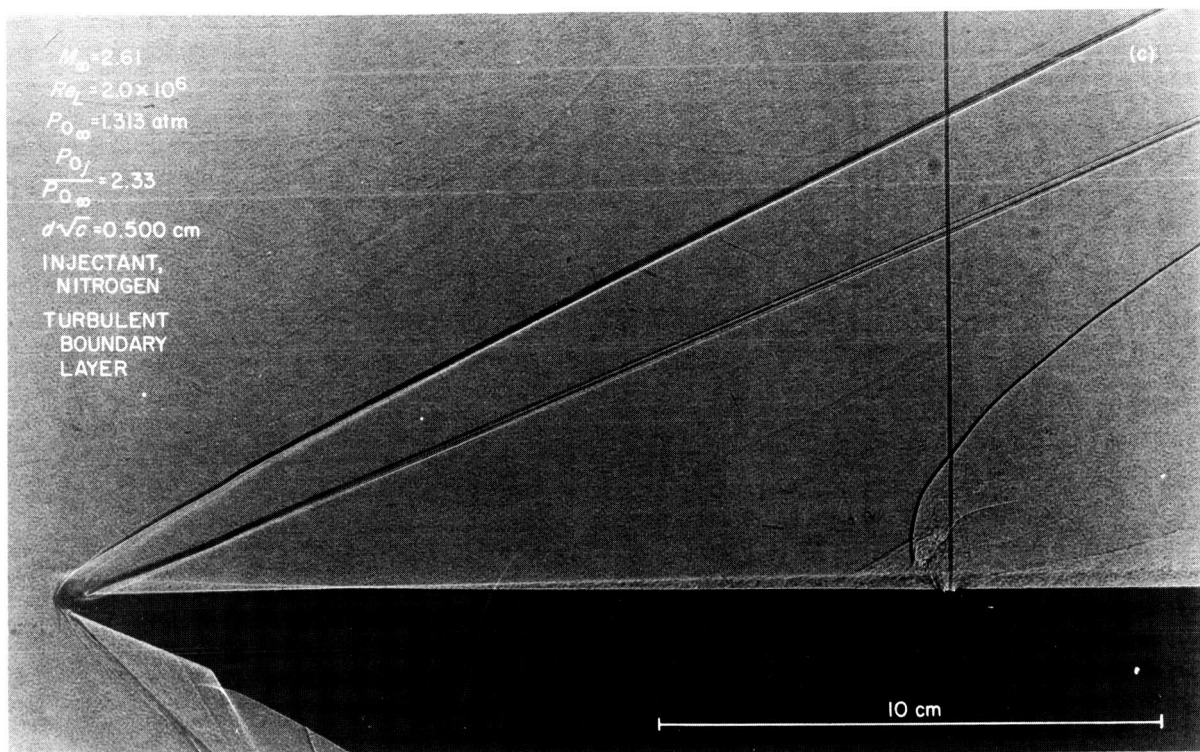


Fig. 4 (Cont'd)

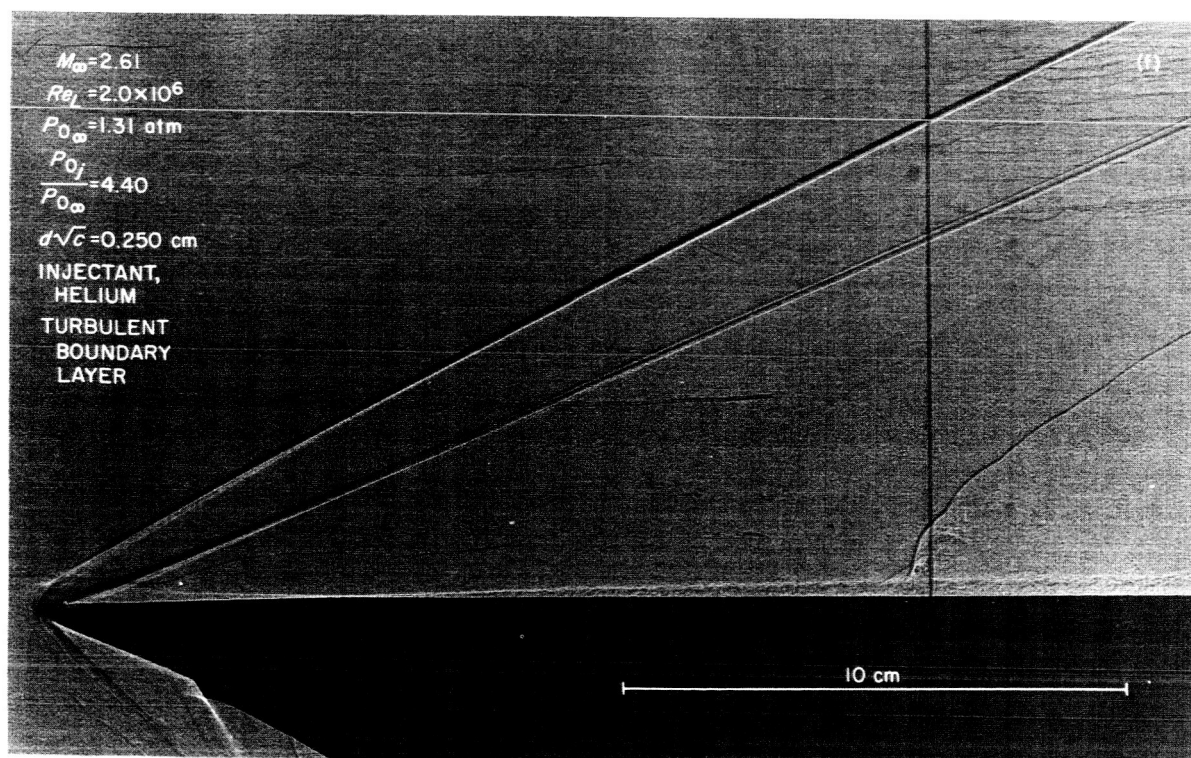
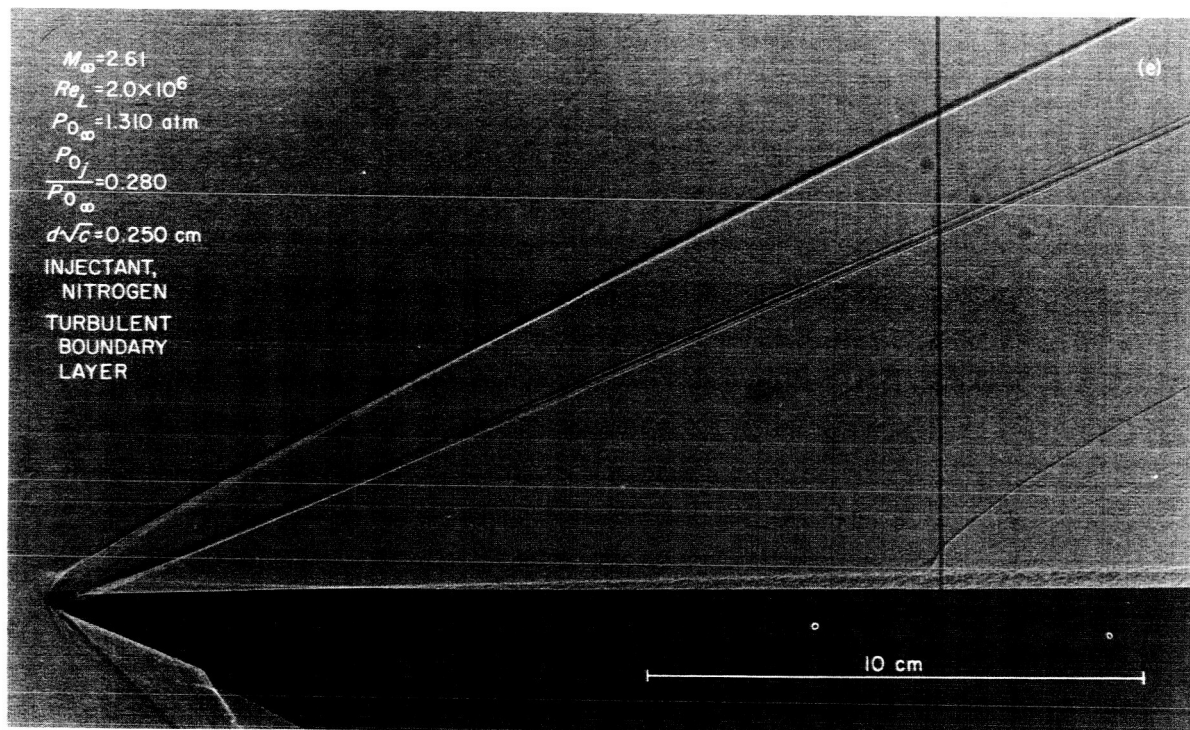


Fig. 4 (Cont'd)

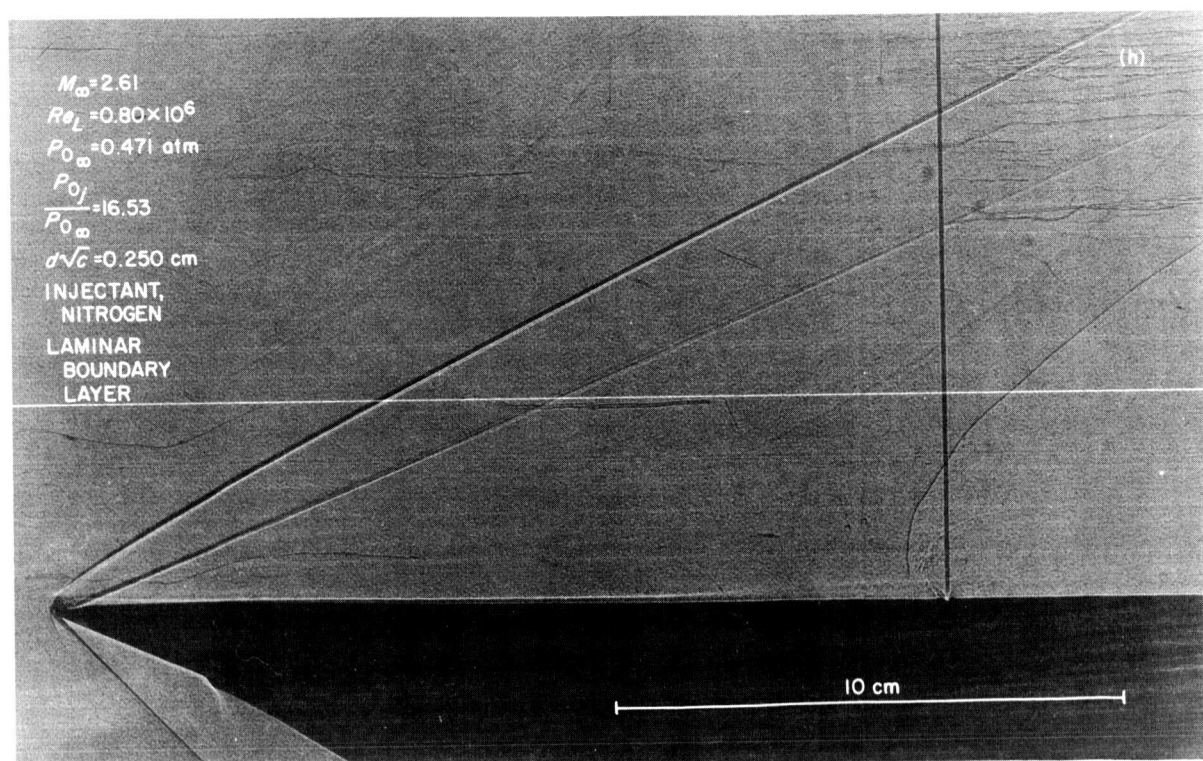
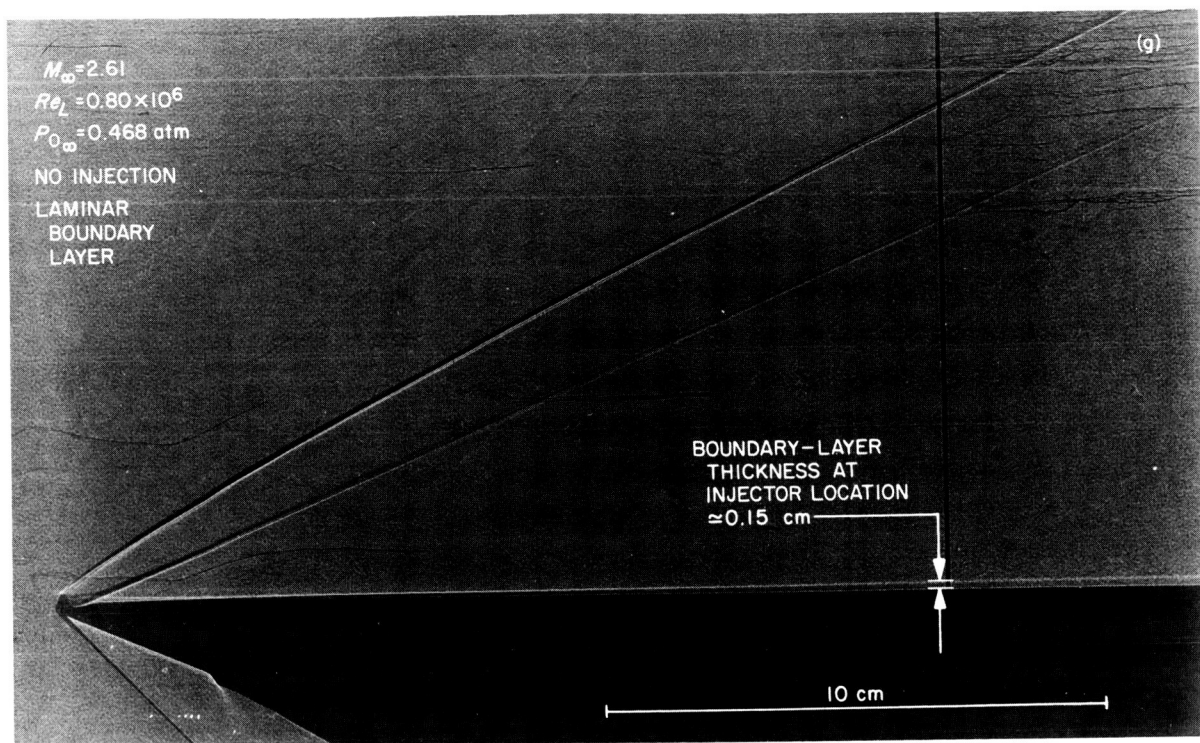


Fig. 4 (Cont'd)

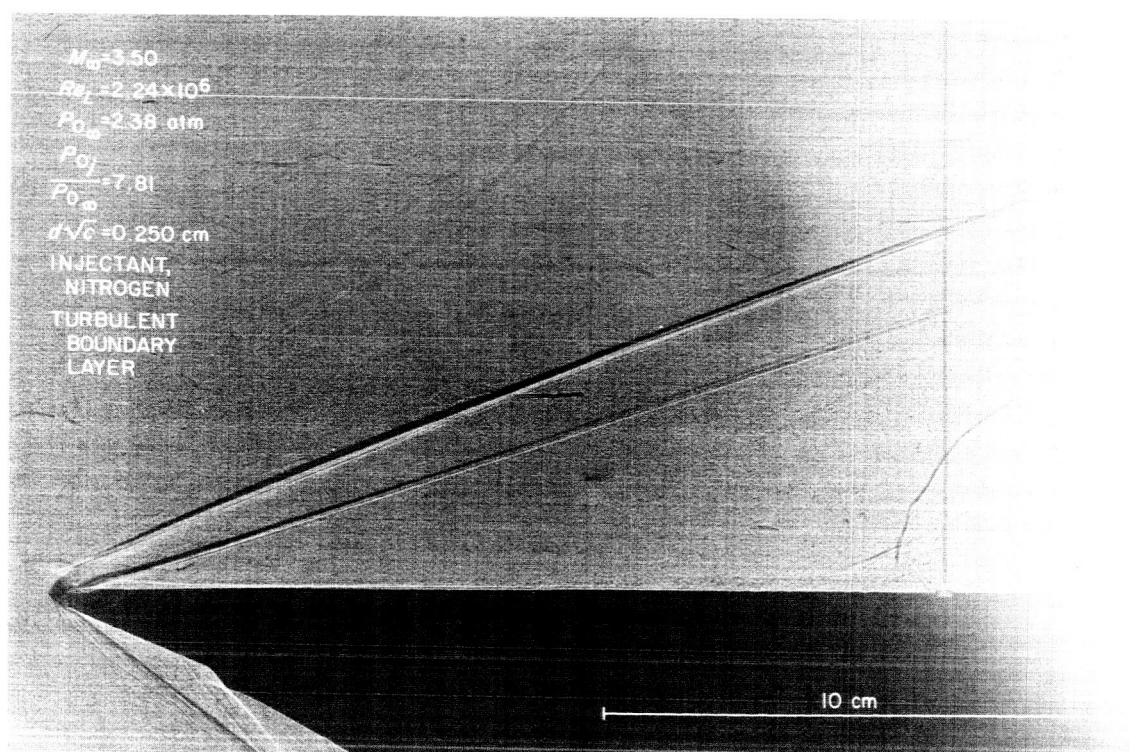
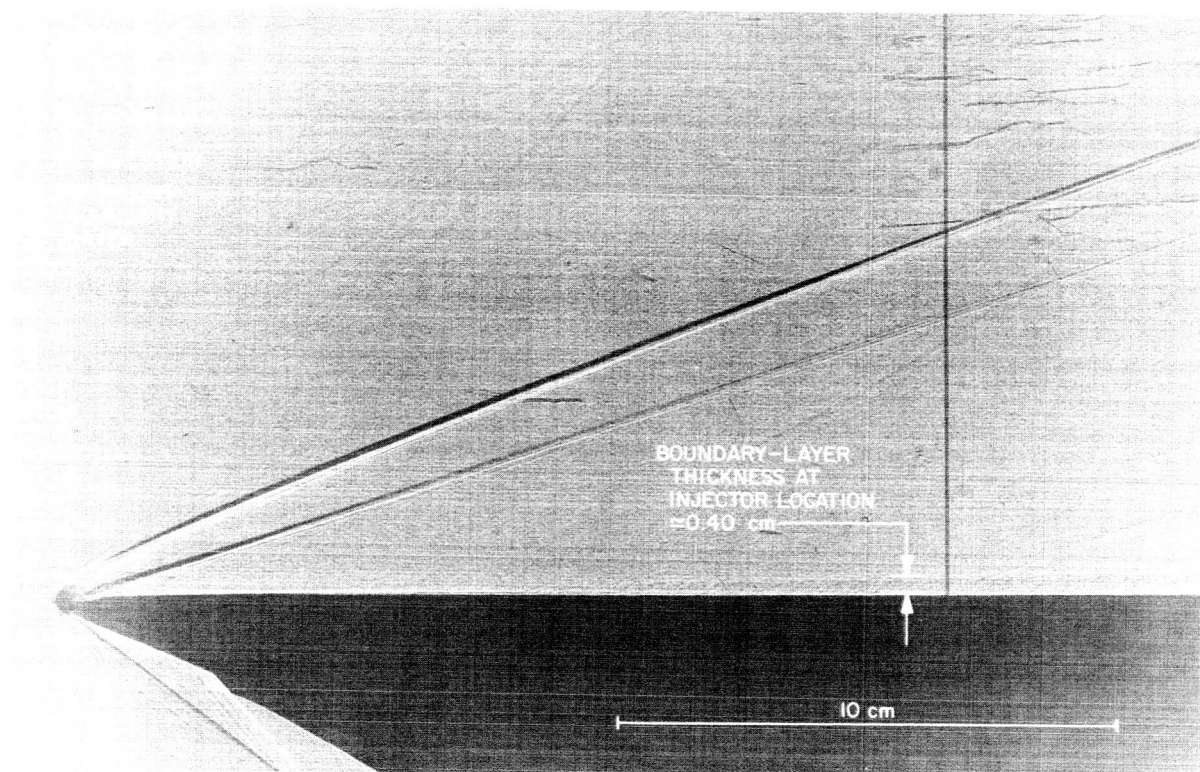


Fig. 4 (Cont'd)

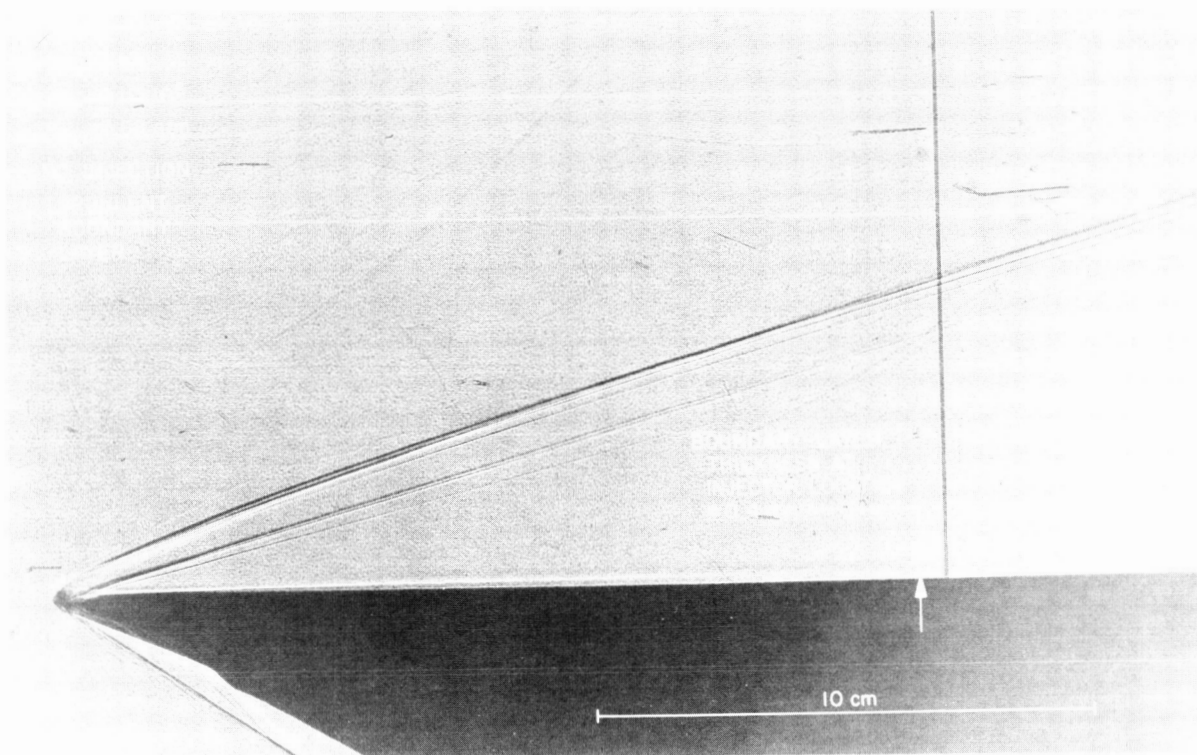


Fig. 4 (Cont'd)

IV. ANALYTIC MODEL

In investigating the shock patterns produced by secondary injection, one is reminded of shock shapes produced by blunt axisymmetric bodies. This fact suggested that some insight into the scaling laws for secondary injection could be obtained by setting up a simple model for a solid body, which would give a shock pattern similar to that produced by injection.

The scheme used here is to pick a shape for the nose of the equivalent body and then to calculate the characteristic dimension of the nose by balancing the drag of the nose section against the momentum flux of the injectant. The analysis is carried out for the momentum flux and force acting parallel to the wall, and the control volume chosen for the analysis is the nose section of the equivalent body, which lies close to the injectant orifice. It is expected that such a simple model may give a useful description of a scaling parameter without necessarily in-

cluding an accurate description of all the details of the flow. The salient features of the flow utilized in the model are the bluff nature of the effective interference body, the separated region immediately downstream of the injector, and the fact that the mixing between the injectant and other gas may be small in the immediate neighborhood of the injector.

The coordinate system used in describing the model is illustrated in Fig. 3a and b. Here, the x - z plane is shown with the y -axis perpendicular to the page. The origin of the coordinate system has been chosen so that the $y = 0$ plane includes the center of the injector and so that the origin lies at the intersection of the bow-shock wave with the wall.

For the purposes of this model it is assumed (1) that a sonic jet is injected into a uniform supersonic flow

with no wall boundary layer; (2) that no mixing occurs between the injectant and either the primary flow or the separated flow near the injector; (3) that the interface between the injectant and primary flows is a quarter sphere followed by an axisymmetric half body; and (4) that the interface between the separated flow downstream of the injector and the injectant always lies inside the surface described in item (3). Several features of this model are illustrated in a schematic manner in Fig. 5, where section views of the flow are shown. The first lies in the $y = 0$ plane and the second in the plane given by $x = h$.

The force balance is made on the control volume formed by the quarter-spherical nose, which is located with one plane surface in the x - y plane and the other in the y - z plane. It is further assumed that (5) the pressure forces on the sphere due to primary flow can be calculated by use of modified Newtonian flow, (6) that the injectant expands isentropically to the ambient pressure with its velocity parallel to the wall at the downstream face of the sphere, and (7) that the contribution to the momentum flux across the y - z plane due to flow in the separated region downstream of the injector can be neglected.

A brief description of the derivation of the equation for the penetration height is given here (see Ref. 6 for a more detailed derivation). First, consider the flow over the spherical nose. For Newtonian flow calculations, with the modification suggested by Lees (Ref. 7), the pressure

coefficient, $C_p \equiv (P - P_\infty)/\frac{1}{2}\rho_\infty V_\infty^2$, on the surface of the body is given by

$$\frac{C_p}{C_p^*} = \frac{\sin^2 \alpha}{\sin^2 \alpha^*}$$

where α is the angle between the local tangent to the surface and the undisturbed flow direction, and must lie between 0 and $\pi/2$. Here C_p^* and α^* are evaluated at the nose of the body. Hence, $\alpha^* = \pi/2$ and C_p^* is the pressure coefficient corresponding to the stagnation pressure behind a normal shock, found from the theory of supersonic flow of an ideal gas:

$$C_p^* = \frac{2}{\gamma_\infty M_\infty^2} \times \left[\left(\frac{\gamma_\infty + 1}{2} M_\infty^2 \right)^{\gamma_\infty/(\gamma_\infty - 1)} \left(\frac{\gamma_\infty + 1}{2\gamma_\infty M_\infty^2 - \gamma_\infty + 1} \right)^{1/(\gamma_\infty - 1)} - 1 \right] \quad (1)$$

In this case, the Newtonian calculation is applicable only to the surface of the quarter sphere. The total axial force on the control volume was obtained by integrating the pressure force in the x -direction over the spherically shaped nose of the equivalent body and the portion of the $x = \text{constant}$ plane just downstream of the nose. The contribution of this latter surface is $-(\pi/2)P_\infty h^2$, which is equal in magnitude but opposite in sign to one of the

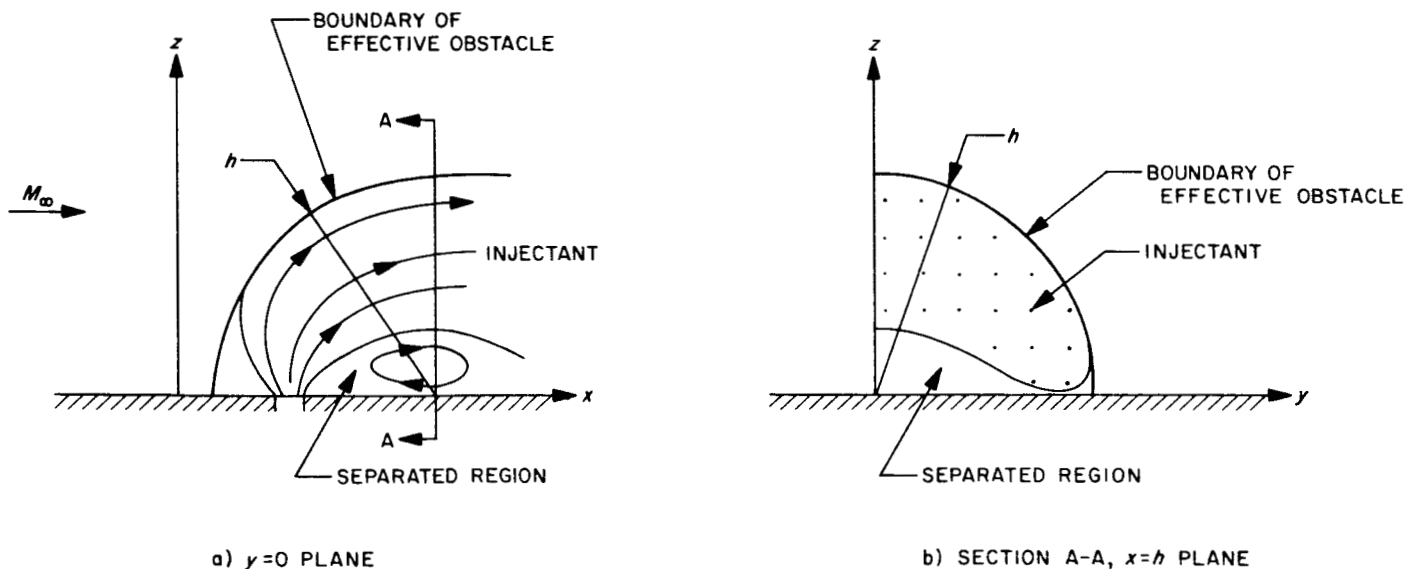


Fig. 5. Schematic diagrams of flow field for the model used in calculations

terms that results from the calculation of the force on the curved surface. The net result is

$$F_x = \frac{\pi}{8} M_\infty^2 \gamma_\infty C_p^* h^2 P_\infty \quad (2)$$

In order to calculate the net momentum outflow through the control volume, note that because the jet is injected normal to the wall, the only contribution is the total x -momentum of the injected gas after it has expanded isentropically to the free-stream static pressure. The analysis could easily be extended to the case of injection at an arbitrary angle to the free-stream flow, merely by including the x -component of the momentum of the injected gas at the injection orifice.

The momentum flux of the expanded secondary flow can be simply evaluated. First, the mass flow of injectant is calculated from the assumption that the injector flow is sonic and fills an area which is c times the actual injector area; that is, c is a discharge coefficient for the injector, and $d(c)^{1/2}$ is the equivalent diameter of the injector, and hence is the characteristic dimension of the injector. From this assumption it follows that

$$m_j = cA_j P_{0j} \left[\left(\frac{\gamma_j}{R_j T_{0j}} \right) \left(\frac{2}{\gamma_j + 1} \right)^{(\gamma_j + 1)/(\gamma_j - 1)} \right]^{1/2} \quad (3)$$

where cA_j is the equivalent injector area. The Mach number at the exit of the control volume is given by the expression for isentropic expansion from a stagnation pressure P_{0j} to a static pressure P_∞ . This expression can be solved for the velocity V_j and the result is

$$V_j = \left\{ \left(\frac{2\gamma_j R_j T_{0j}}{\gamma_j - 1} \right) \left[1 - \left(\frac{P_\infty}{P_{0j}} \right)^{(\gamma_j - 1)/\gamma_j} \right] \right\}^{1/2} \quad (4)$$

The momentum flux is $m_j V_j$, and consequently, the force balance is given by

$$F_x = m_j V_j \quad (5)$$

All the parameters in this equation are known except the radius h , and therefore, Eq. (5) can be solved for this parameter. The result is

$$\begin{aligned} \frac{h}{d(c)^{1/2}} &= \left\{ \left(\frac{1}{M_\infty} \right) \left(\frac{P_{0j}}{P_\infty} \right)^{\gamma_j} \left(\frac{2}{\gamma_\infty C_p^*} \right) \right. \\ &\times \left. \left[\frac{2}{\gamma_j - 1} \left(\frac{2}{\gamma_j + 1} \right)^{(\gamma_j + 1)/(\gamma_j - 1)} \left(1 - \left(\frac{P_\infty}{P_{0j}} \right)^{(\gamma_j - 1)/\gamma_j} \right) \right]^{1/4} \right\} \quad (6) \end{aligned}$$

Note that when the ratio P_{0j}/P_∞ is held fixed, the radius decreases with increasing Mach number. However, for rocket work, it is often more convenient to use the stagnation-pressure ratio $P_{0j}/P_{0\infty}$ as the independent variable.

The first two factors of Eq. (6) may be rewritten to give

$$\left[\frac{1}{M_\infty} \left(1 + \frac{\gamma_\infty - 1}{2} M_\infty^2 \right)^{(\gamma_\infty)/2(\gamma_\infty - 1)} \left(\frac{P_{0j}}{P_{0\infty}} \right)^{\gamma_j} \left(\frac{2}{\gamma_\infty C_p^*} \right)^{1/2} \right] \quad (7)$$

It is evident from this form of these terms that the radius increases with the square root of $P_{0j}/P_{0\infty}$ and, in a more complex manner, with M_∞ .

The variation of the terms in the square bracket of Eq. (6) and that of C_p^* with M_∞ or γ_∞ is not very rapid. Hence, the most important variation of the radius is approximately given by

$$h \propto [d(c)^{1/2}] \left(\frac{1}{M_\infty} \right) \left(\frac{P_{0j}}{P_\infty} \right)^{1/2} \quad (8)$$

In terms of the mass flow rate of injectant m_j , Eq. (8) can be written as

$$h \propto \frac{1}{M_\infty} \left(\frac{m_j}{P_\infty} \right)^{1/2} (R_j T_{0j})^{1/4} \quad (9)$$

Note that for simplicity, the complex dependence on γ_j and γ_∞ has been omitted here. Equations (8) and (9) are useful as long as $(P_\infty/P_{0j}) \ll 1$ and $M_\infty > 2$.

Although the derivation used to obtain Eq. (6) was based on the assumption of a spherical interface between primary and injectant flows, it should be noted that the functional form of Eq. (6) is not sensitive to the shape of the interface. For example, the derivation has been carried out for elliptical interface shapes with eccentricities ranging between 0 and 0.98. The equations for h obtained by this calculation had the same functional form given in Eq. (6) and differed from it by a multiplicative constant that depended on the eccentricity and that changed only by a factor of 2.3 for the range of eccentricities given above.

It is proposed that the calculated radius can be used as a measure of the scale of the disturbance produced by injection. Note that although the expression for h , given

in Eq. (6), contains no adjustable constants, the exact correspondence between values calculated from Eq. (6) and any measured feature of the flow, such as the penetration height mentioned in Section II, is purely fortuitous. However, if the model is correct, it is to be expected that changes in scale of flow features will be proportional to changes in h .

Since the boundary layer has not been considered at all in this analysis, it would be expected that h would have to be larger than a characteristic boundary-layer dimension in the immediate vicinity of the jet, i.e., a characteristic thickness of the boundary layer in the region of maximum separation, in order for the analysis to be applicable.

However, there is a difference between the observed flow field and the model that seems to make this limitation somewhat less severe. As the injectant expands just after leaving the orifice, it is initially conical in shape so that the actual obstruction shape as viewed from the front is probably similar to that of a frustum of a cone with its small end resting on the wall, and capped by a sphere.

This shape would be expected to produce considerably less of an obstacle to the boundary layer than a quarter sphere of the same projected area.

Figure 4 gives typical examples of the change in boundary-layer thickness caused by injection. The maximum thickness of the separated boundary layer upstream of the injector was never observed to be more than about twice the thickness of the undisturbed boundary layer at the same distance from the plate, as determined from the photographs.

To provide a basis for comparison, some experiments with solid objects of the same shape as that postulated in the analytic model have been conducted. These objects were attached to the nozzle wall, and schlieren pictures were taken at a test-section Mach number of 2.56. Photographs with the same shock shape were compared. The separation produced with both laminar and turbulent wall boundary layers was always considerably more extensive than that produced by injection, thus supporting the preceding supposition about the applicability of the model.

V. PRESENTATION OF EXPERIMENTAL DATA

Results are given of experiments concerning the flow-field geometry, concentration measurements, and static-pressure measurements on the wall. The data are presented in terms of space coordinates normalized by the radius, which is calculated from Eq. (6). This mode of presentation was used to facilitate the verification of the proposed scaling law.

A. Penetration Height

In most of the schlieren photographs taken of the flow with secondary injection of argon and nitrogen into air, a distinct feature appears that looks like the top or outer boundary of the jet. Although this feature, shown in Fig. 3c and 3d and also visible in some of the photographs

of Fig. 4, is probably the line of maximum concentration of injectant rather than the jet boundary, it has been selected as being characteristic of the scale of the disturbance produced by the jet, and hence is called the penetration height of the jet. That flow fields for different injection rates should be geometrically similar is, of course, an assumption that must be verified.

Values of the penetration heights determined directly from schlieren photographs made in the Caltech facility are shown in Fig. 6. Here, penetration heights normalized by the equivalent injector diameter $d(c)^{1/2}$ are given as a function of the ratio of injectant to primary-stream stagnation pressures; data are presented for two Mach numbers. Nitrogen and argon were used as injectants, and experiments were conducted with two injector diameters.

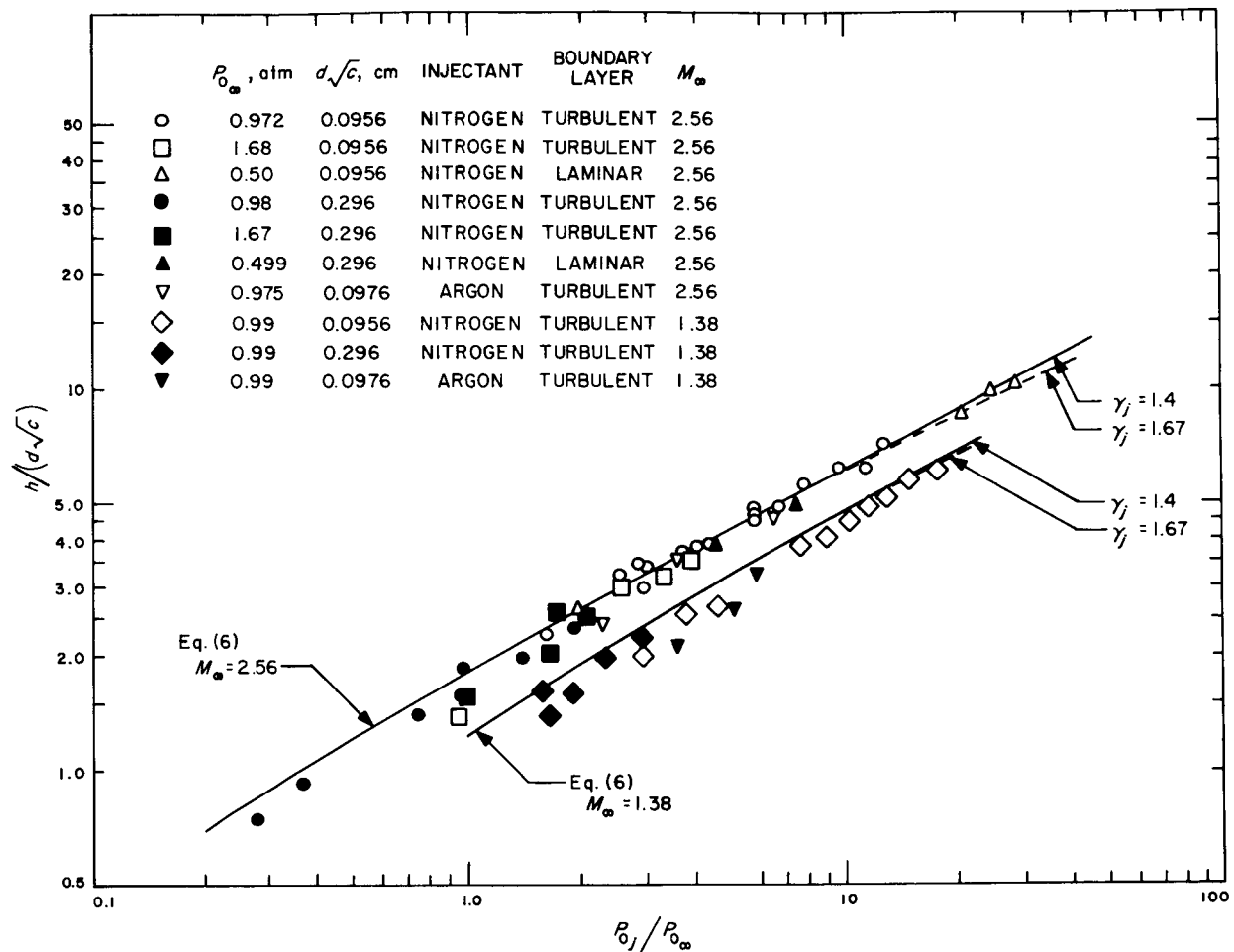


Fig. 6. Penetration of secondary jet into primary flow, nozzle-wall data

The magnitude of the penetration height was found to depend directly on the equivalent injector diameter and to vary approximately with $(P_{0j}/P_{0\infty})^{1/2}$. No dependence on injector molecular weight or specific heat ratio was noticed when penetration heights for a given total-pressure ratio were compared.

The data shown in Fig. 6 were obtained when the boundary layer was both laminar and turbulent. It is particularly interesting to note that measured values of the penetration height were not noticeably dependent on the state of the boundary layer, and comparison of the JPL and Caltech data indicates that they were not noticeably dependent upon the boundary-layer thickness for values of h that were greater than or equal to the boundary-layer thickness.

The data of Fig. 6 show that the height increases with increasing Mach number in the primary stream. This is a result of the fact that for a given primary stagnation

pressure, the local static pressure decreases rapidly with increasing Mach number.

Theoretical values of the scale parameter are also shown in Fig. 6 for both Mach numbers. The agreement between the calculated and measured quantities is good over the whole pressure-ratio range studied, and the dependence on specific heat ratio, molecular weight, and Mach number is correctly predicted.

Values of penetration heights were obtained in the JPL facility from shadowgraph photographs for a wide range of Mach number and pressure ratio. Comparison of these data with data obtained in the Caltech facility showed that the JPL flat-plate results were about 20% lower than the comparable Caltech nozzle-wall data. This systematic difference is probably due to differences in the optical systems. Also, in comparing the data with the results predicted from the model, it should be remembered

that the features examined on either schlieren or shadowgraph pictures are not the jet boundaries themselves, and hence that either the calculated scale factors or the measured penetration heights can only be viewed as being proportional to the actual characteristic scale of the flow.

Comparison of the flat-plate data and the results of Eq. (6) are shown in Fig. 7. Here, in order to facilitate the comparison of theory and experiment, all of the measured penetration heights are increased by 20%. The agreement between the trends predicted by theory and those found experimentally appears to be good, although the experimental data may have a slightly more rapid variation with Mach number than is predicted from Eq. (6).

Although the good absolute agreement between the predictions of Eq. (6) and measured values is fortuitous, the fact that the data agree so well in slope and shape over a range of injector diameter, injection pressure, and

primary-flow Mach number indicates that the value of the scale factor predicted by Eq. (6) is a useful measure of the scale of the interaction phenomena and suggests that the proposed model does include the pertinent physical phenomena. The success of this simple model in predicting the penetration heights also indicates that the gross features of the flow field can be characterized by a single dimension that is proportional to h .

B. Shock Shapes

As a further check on the suggestion that h is a characteristic dimension of the flow field, the shapes of the bow-shock waves, as seen from the side, were determined from schlieren and shadowgraph pictures for both the flat-plate and nozzle-wall data. In all cases, the shock coordinates were normalized by values of h calculated from Eq. (6). In Fig. 8, a few typical cases from the nozzle-wall data are compared. The shock shapes plotted here

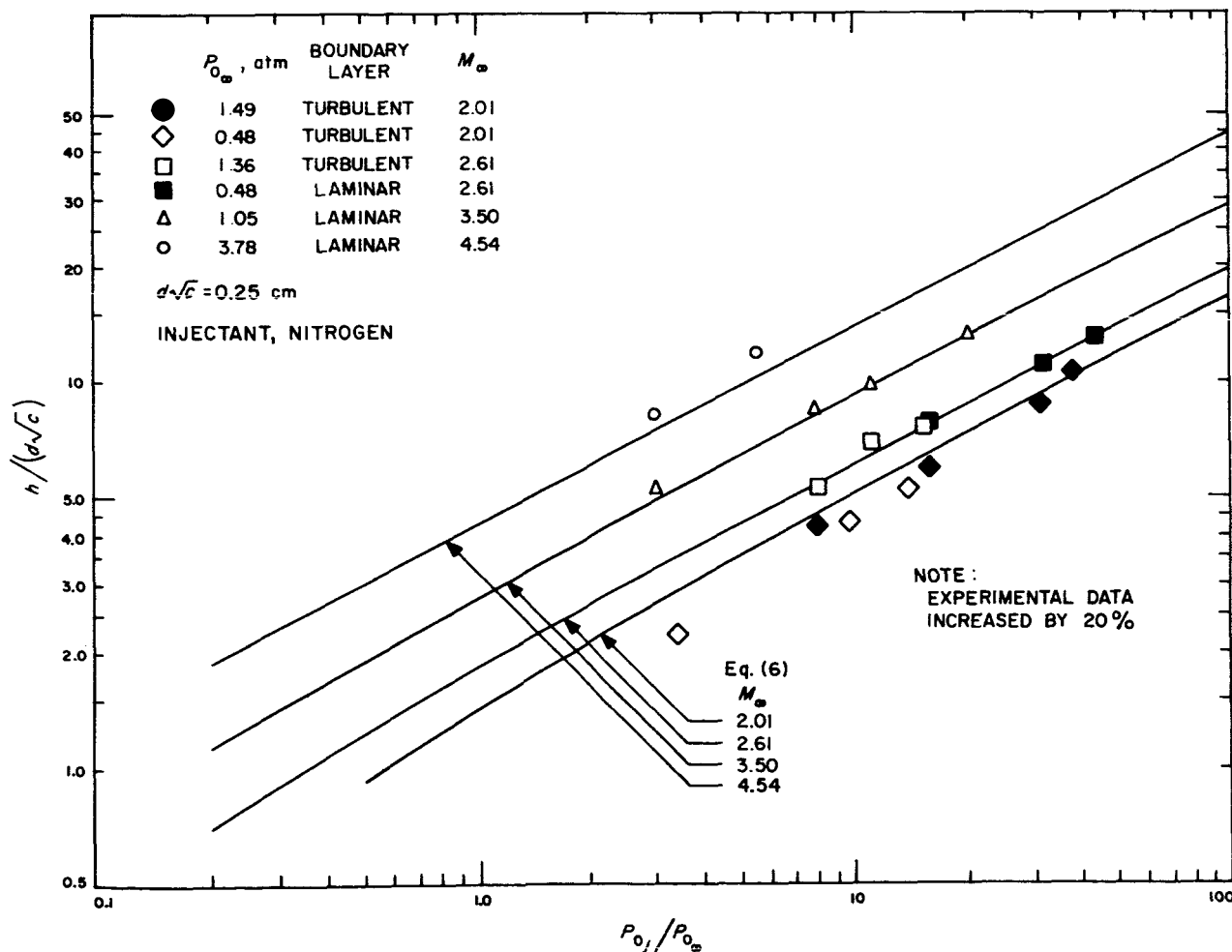


Fig. 7. Penetration of secondary jet into primary flow, flat-plate data

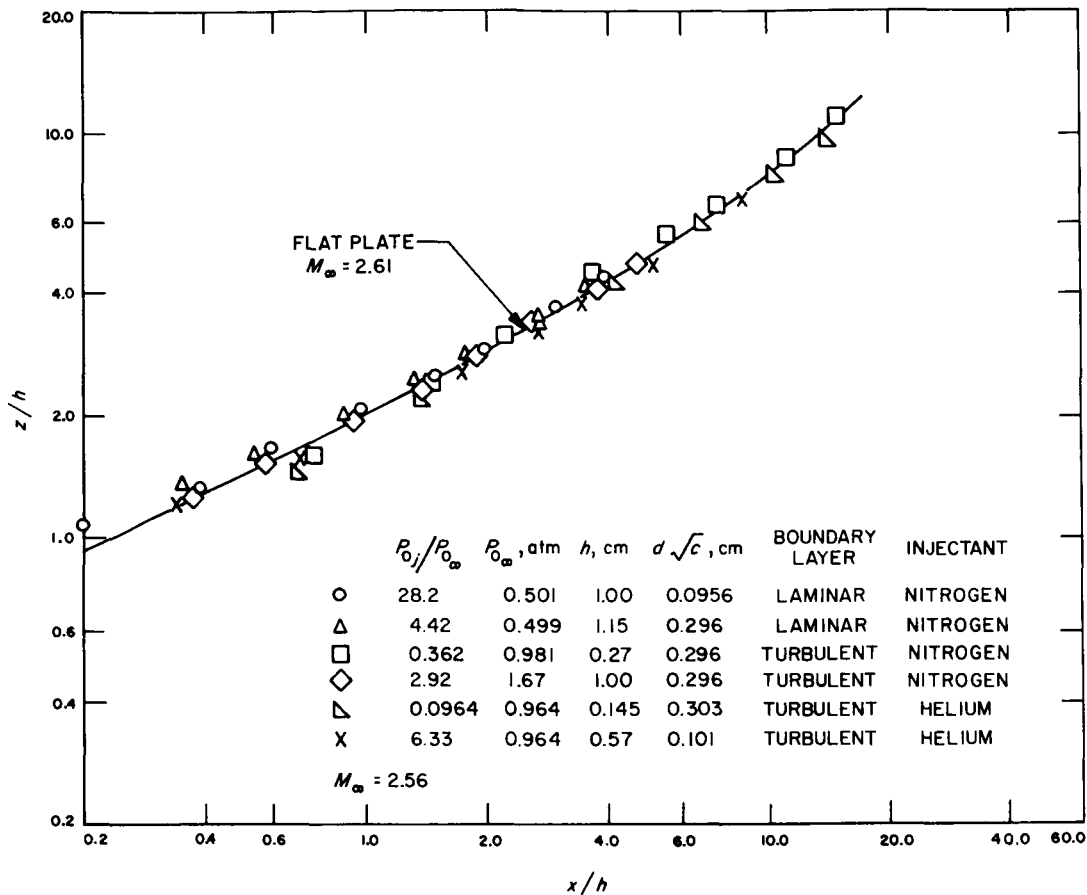


Fig. 8. Shock shapes; comparison of nozzle-wall and flat-plate results

cover the maximum range of parameters studied in the Caltech supersonic wind tunnel, and are typical of the measurements made from more than 50 schlieren photographs. The solid line in Fig. 8 represents the average of the data obtained from the JPL flat-plate experiments at a Mach number of 2.61. These data showed somewhat less scatter than did the nozzle-wall data plotted here.

In Fig. 9, shock coordinates are presented for a range of Mach numbers that represent averages of shock-shape data from the JPL flat-plate experiments. This method of data presentation was chosen because the curves lie so close together that it would have been very difficult to visualize the important features had the data points been plotted, yet their significance is lost if they are not directly compared. The scatter in the data is somewhat less than that shown in Fig. 7, except where the curves are dashed, in which case the difficulty in interpreting the photographs caused greater scatter. Some of this difficulty at the higher Mach numbers was caused by the unsteadiness in the flow field previously mentioned. The fact that the curves in Fig. 9 all approach a single curve

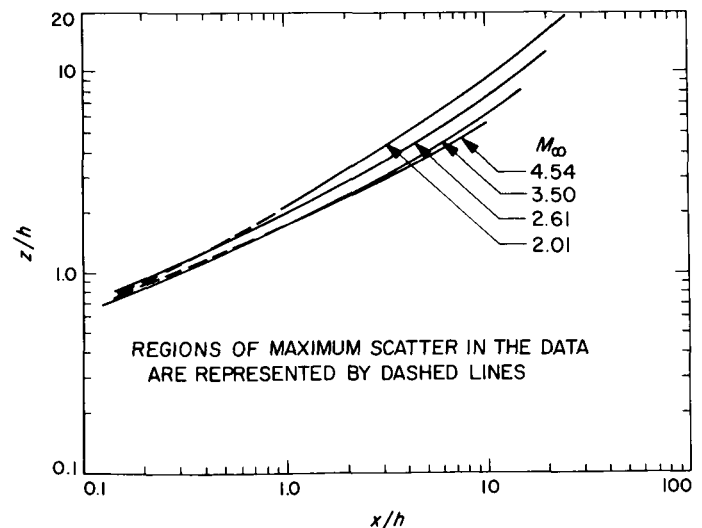


Fig. 9. Shock shapes showing Mach number effect

for small values of x/h indicates that the properly normalized shock shapes near the injector port are nearly identical. Now, the shock location near the nose

of a blunt body in a supersonic flow is very weakly dependent on Mach number (for Mach numbers larger than about 2.0), but is strongly dependent upon the size of the body. Thus, Fig. 7 indicates that the dependence of h upon the free-stream Mach number is correctly predicted by Eq. (6).

It is again evident from study of these data that the normalized coordinates agree well and that the agreement appears to be independent of pressure ratio, specific heat ratio, injector diameter, and the condition of the boundary layer. In addition, the fact that the data from schlieren and shadowgraph pictures agree well substantiates the assertion that the observed differences in penetration height from these sources is a result of the differences between these two flow-visualization techniques.

In order to check the influence of molecular weight on the process, some shock-shape data were obtained with helium as injectant. Unfortunately, schlieren and shadowgraph photographs taken with helium as injectant did not reveal the penetration distance directly. However, the bow shock was easily observed, e.g., in Fig. 4f, and in the normalized form agreed quite well with the other data. Here the data were normalized by values of penetration height calculated from Eq. (6) with experimentally determined values of the flow coefficient c . Hence, the characteristic dimension of the interaction that fixes the shock geometry is independent of molecular weight.

The data discussed above concern the shapes of the intersection of the shock-wave surface with the x - z plane.

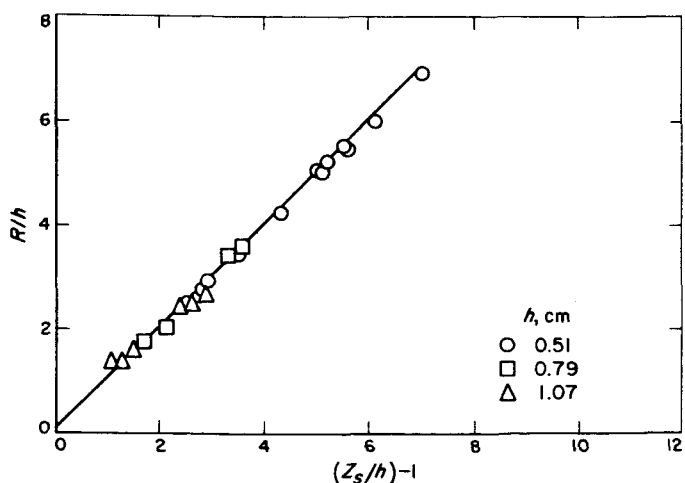


Fig. 10a. Linear comparison of normalized dimensions of shock shapes, showing axisymmetry of shock with three-dimensional injection; $M_\infty = 2.61$

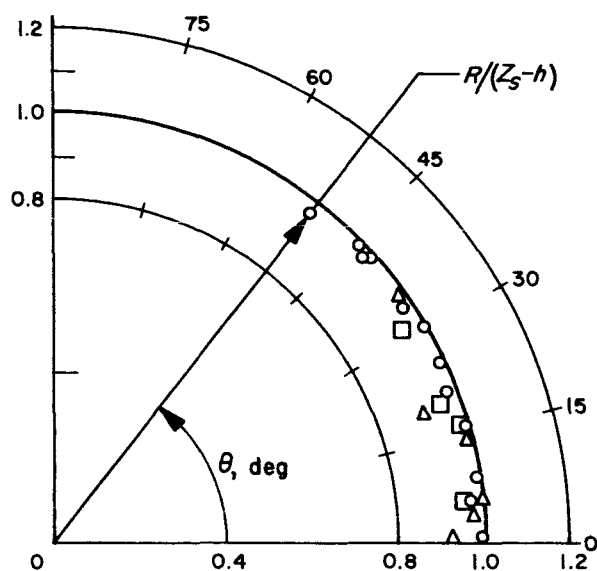


Fig. 10b. Polar plot of ratio of normalized shock dimensions from Fig. 10a as functions of position in injectant-plume cross section

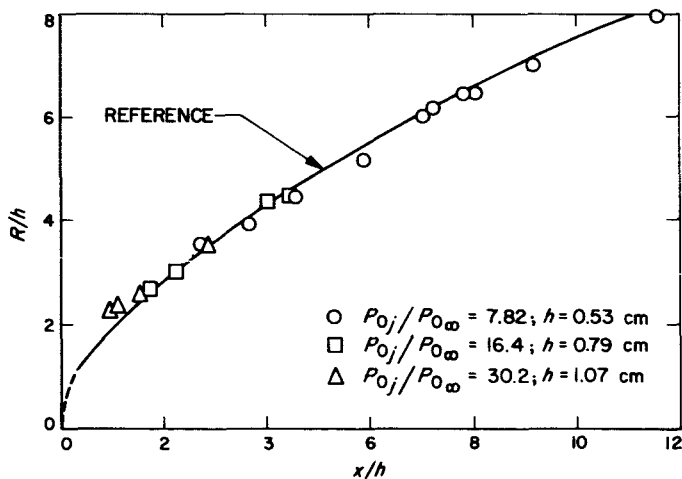


Fig. 10c. Comparison of off-centerline shock radii with centerline shock shapes measured from schlieren pictures (reference); $M_\infty = 2.61$

A three-dimensional picture of the shock shape produced by injection was obtained by Burden in the Caltech facility (Ref. 2) in the following manner. At three different injection-pressure ratios, and thus at three different values of h , position of the shock surface was measured at a number of points off the x - z plane. These measurements were made by locating the off-axis shock surface with a Pitot probe, and then obtaining the probe position from a photograph. The shock coordinates were compared with values obtained at the same axial x station, but for $y = 0$.

Both measurements were made from the same schlieren photograph. Analysis of the data indicates that the shock surface is axisymmetric about a centerline that is parallel to the x -axis and is about one h from the wall. Figures 10a and 10b illustrate this result by comparing values of Z_s/h and R . In Fig. 10a, Z_s/h is the height of the shock in the x - z plane, measured from the axis line, which lies h above the wall and is in the x - z plane. The radial distance between the hypothetical axis and the point at which the Pitot probes meet the shock is R . Both distances are

normalized by h in this figure. Shock shapes as measured above are also compared with those measured in the x - z plane (indicated as "reference") in Fig. 10c. In Fig. 10a and 10c the correlation of the data is quite good.

For the data presented in Fig. 10, the boundary layer is about 0.5 cm thick, and it is possible that δ and not h should be used as the offset for the shock centerline. However, use of δ instead of h as the offset distance for the axis leads to systematic errors in the correlation of shock

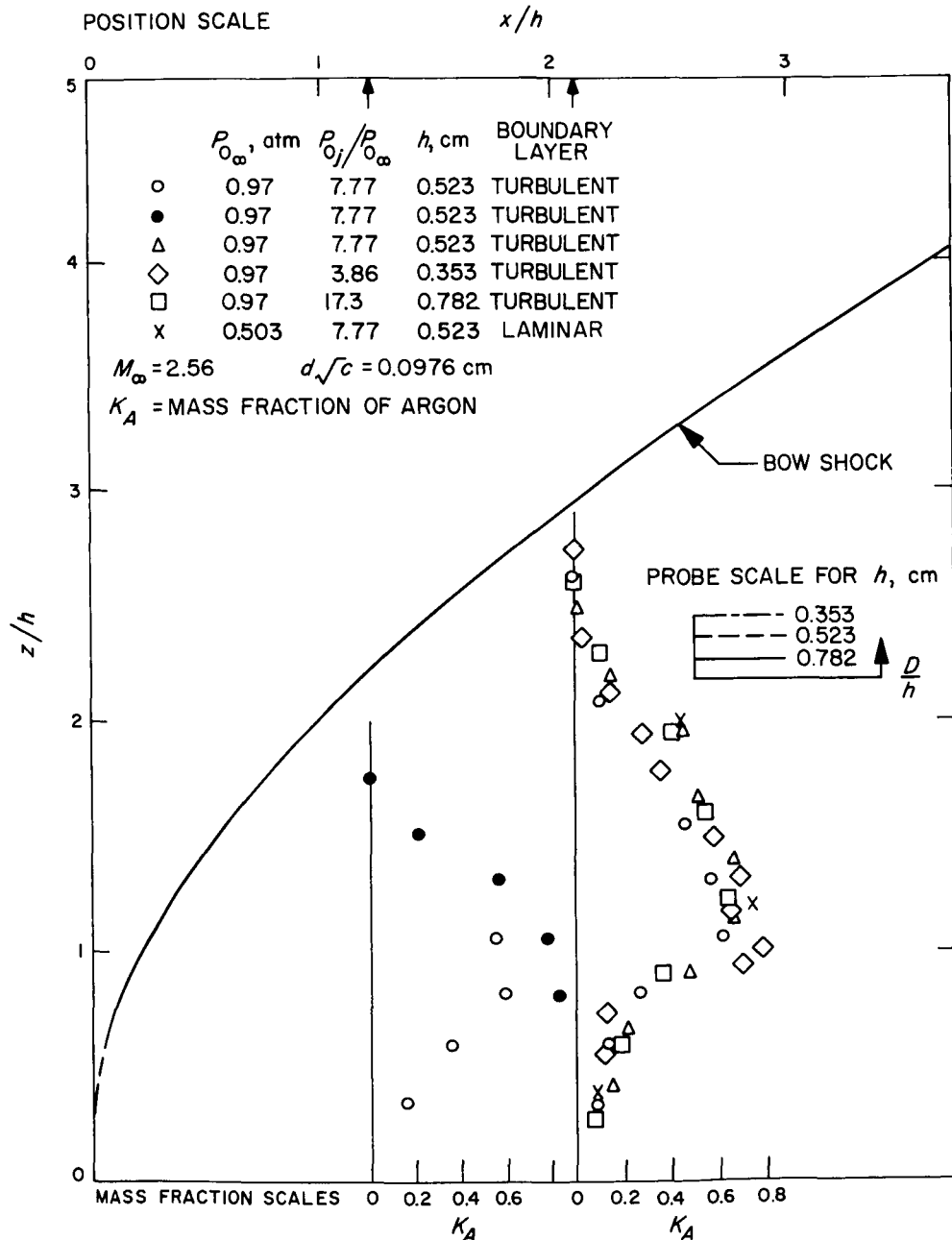


Fig. 11a. Concentration measurements in the plane $(y/h) = 0$, injector region, with argon as injectant

coordinates for the two higher values of h . Hence, the good correlation of the data shown in Fig. 10, with the axis of symmetry located at h off the wall, indicates that h and not the boundary-layer thickness is the proper distance for the location of the axis of symmetry.

In summary, the tests show that the shock shape is axisymmetric about an axis lying in the x - z plane, and parallel to the wall but displaced a distance h along the z -axis from the wall. Given this axis, the curve in Fig. 8 gives a complete description of the shock shape produced by injection at Mach 2.61. In addition, the shape appears to be independent of injectant molecular weight and boundary-layer condition as long as the penetration height is larger than the boundary-layer thickness.

C. Concentration Profiles

A different type of check on the proposed scaling law is given by examination of the flow pattern of the injectant. The mixing of the injectant and primary flows has been examined by making analyses of gas samples drawn from various locations in the flow field. Measurements were taken at Mach number 2.56 in the nozzle-wall injection system with argon and helium as injectant. The positions most thoroughly studied lie in the x - z plane, $y = 0$; a few positions for other values of y were also examined. In addition, a much smaller amount of data was obtained in the JPL facility at Mach 2.61 and 3.50 and with both helium and argon as injectant.

Data obtained with argon as injectant in the $y = 0$ plane are shown in Fig. 11a and 11b. Here, the origin

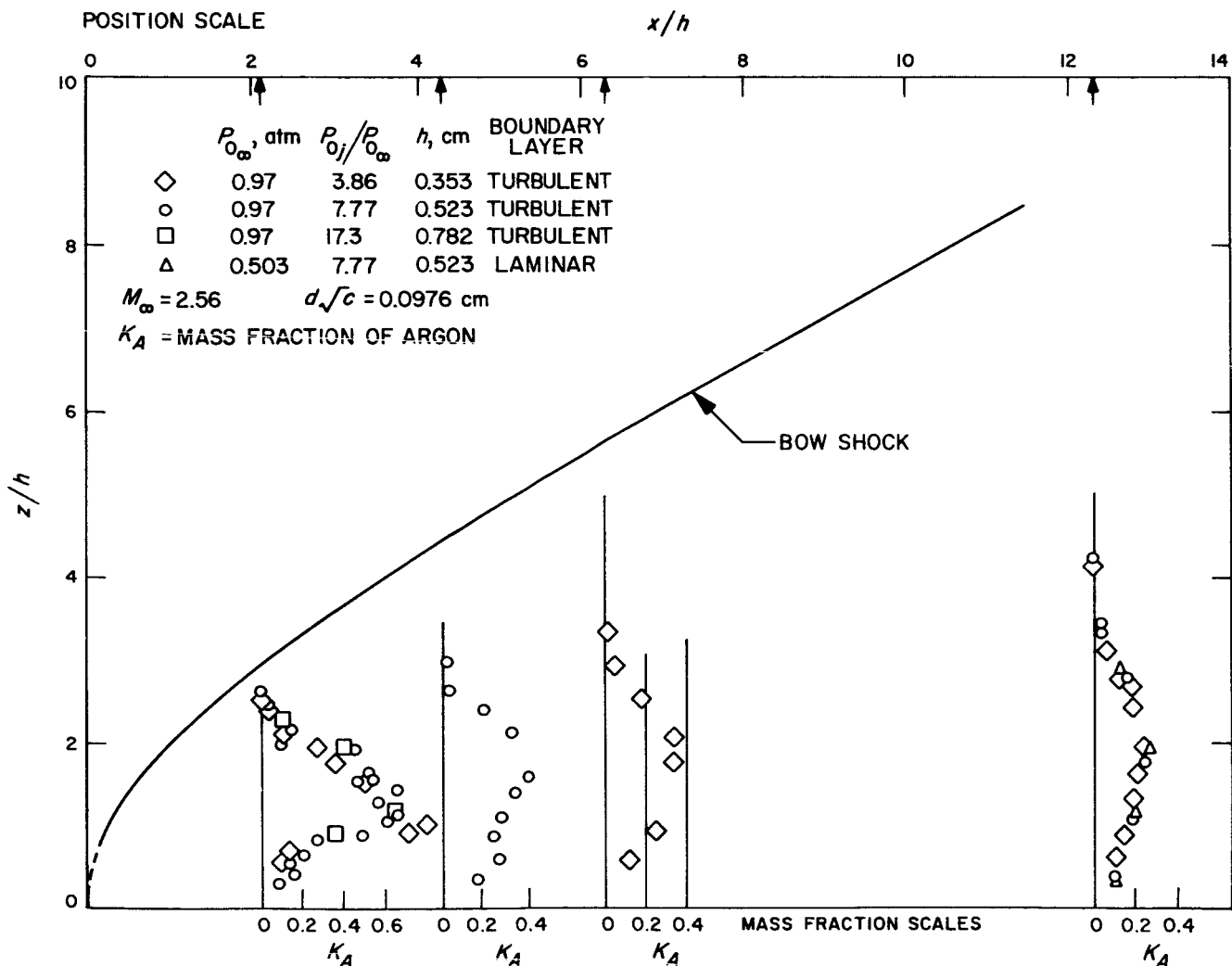


Fig. 11b. Concentration measurements in the plane $(y/h) = 0$, downstream region, with argon as injectant

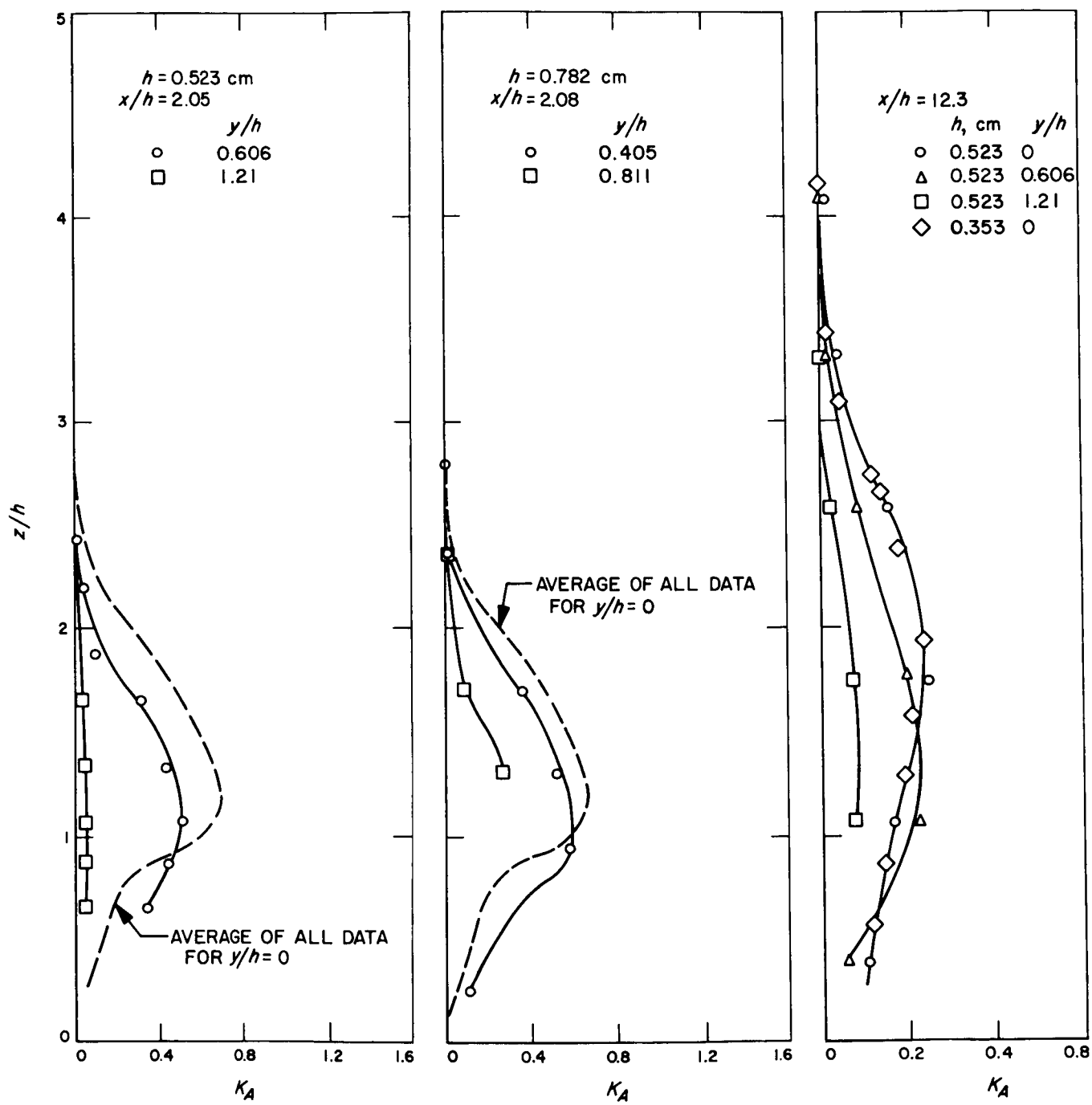


Fig. 12. Concentration profiles in several planes; $(y/h) = \text{constant}$, $M_\infty = 2.56$, $P_{u,\infty} = 0.97$ atm

of each concentration profile is superimposed at the appropriate position on a plot of the x - z plane, which also shows the bow-shock wave. In Fig. 11a, the region close to the injector is shown on an expanded scale, and the data points are presented in detail to illustrate the reproducibility of the experiments. All coordinates are normalized by calculated values of the scale parameter. The normalized diameter of the probe used to make these measurements is shown in Fig. 11a for each value of h used in the experiments.

The data in Fig. 11a and 11b show that near the injector the profile is sharply curved on the lower side of the maximum, but that downstream of $x/h \approx 4$, the profile is roughly Gaussian except for a slight wall-interference effect. It is obvious that the observed penetration height and calculated scale factor correspond much closer to the line of maximum concentration than to the outer edge of the injectant stream.

For $x/h \approx 2$, the maximum concentration was found to be less than 0.80; thus, even this close to the injector, the injectant is already substantially mixed with the primary flow. Further downstream, mixing is slower. From this result, it is obvious that the no-mixing approximation made in the model can only be useful close to the injector.

Measurements made on planes other than $y = 0$ are shown in Fig. 12 for two values of x/h . These data and those shown in Fig. 11 have been used to obtain the cross plots and concentration profiles shown in Fig. 13 and 14. In Fig. 13, cross plots of concentration vs y/h for a number of values of distance above the wall, z/h , and for two values of x/h are shown. Above the concentration maximum, the curves are again roughly Gaussian, but below it they have a definite concentration minimum on the $y/h = 0$ axis. This minimum is present at both x/h stations, but is much less marked at $x/h = 12.3$.

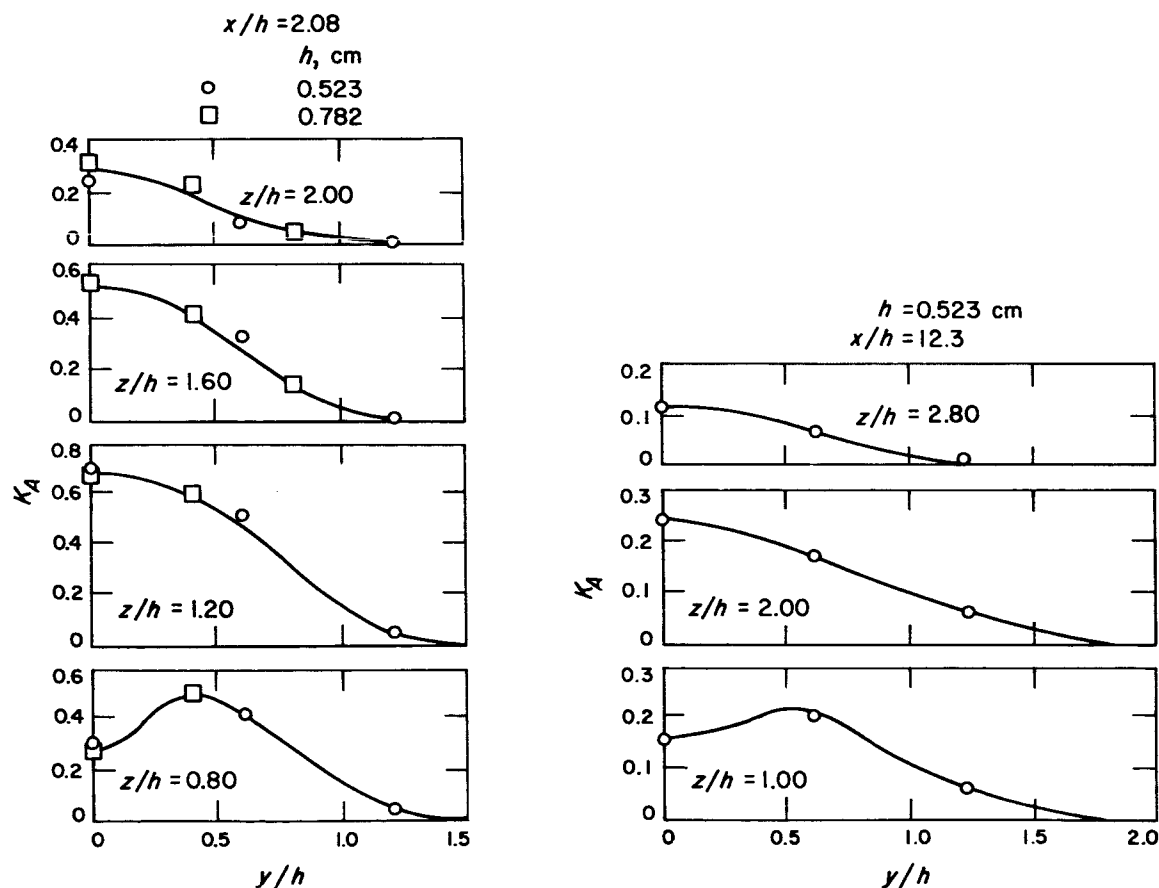


Fig. 13. Crossplots of argon-concentration profiles in planes for which $(z/h) = \text{constant}$, $M_\infty = 2.56$, $P_{0,\infty} = 0.97 \text{ atm}$

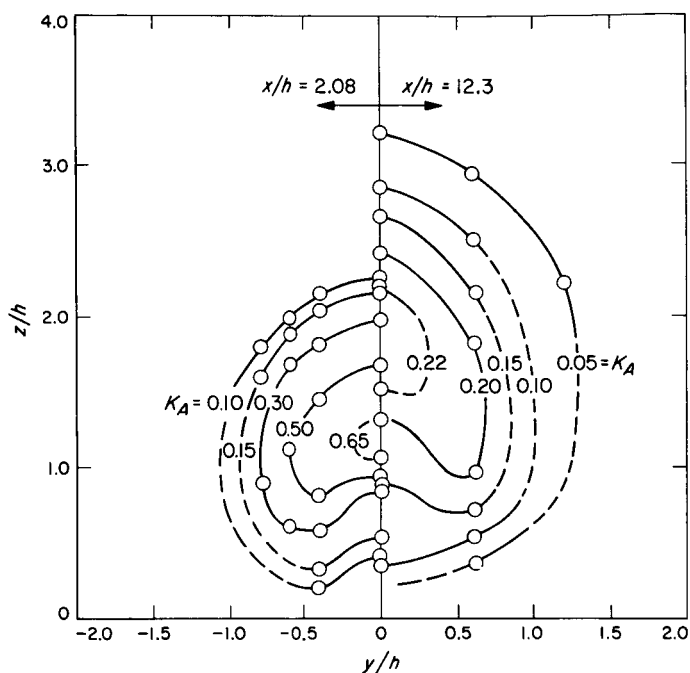


Fig. 14. Concentration contours in the planes $(x/h) = 2.08$ and $(x/h) = 12.3$; $M_\infty = 2.56$; $P_{0\infty} = 0.97$ atm

The concentration profiles of Fig. 14 show the extent of this minimum more clearly. Here, lines of constant concentration in the $(y/h)-(z/h)$ plane are presented. The solid points shown in Fig. 14 were obtained by interpolation of the data of Fig. 11 and 12, and the dashed curves are from a double interpolation of the data. The shapes of the two plots are roughly similar, although the x/h dimension appears to be growing slightly more rapidly than the y/h dimension.

The kidney-shaped cross section seen in the concentration profiles of Fig. 14 suggests that a vortex is shed from either side of the injectant jet. The vortex filaments appear to be roughly parallel to the wall, and with vorticity such that, near the wall, primary gas is swept in toward the centerline of the flow, i.e., toward $y/h = 0$. This type of vortex structure has been observed by other workers for subsonic injection into a subsonic stream (Ref. 8). Such vortices may explain the steep gradients in concentration observed at the $x/h \approx 2$ position.

The data presented in Fig. 11-14 were obtained with argon as injectant. Similar data obtained with helium are

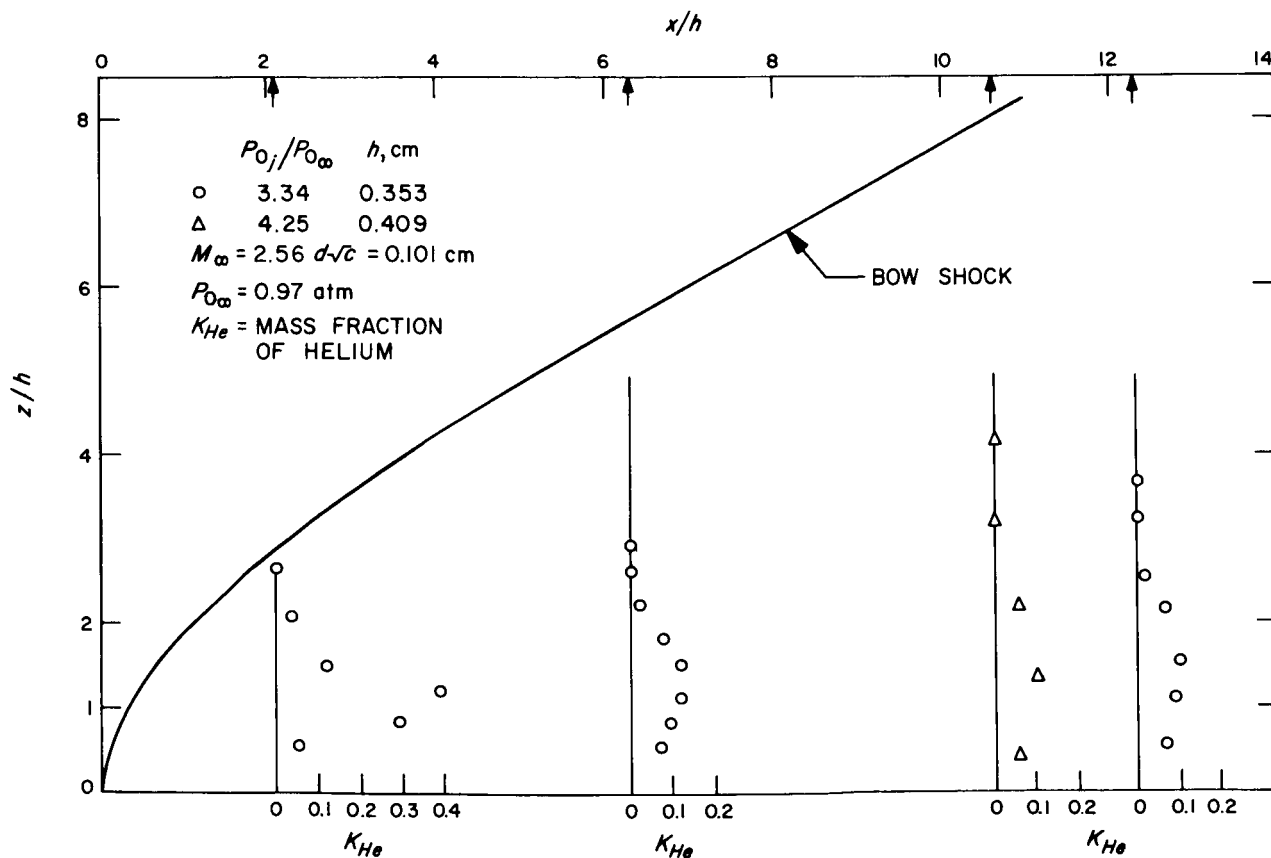


Fig. 15a. Concentration measurements in the plane $(y/h) = 0$, with helium as injectant

shown in Fig. 15a. As would be expected, these curves, presented in terms of mass fractions, are not identical with the argon data, since the two situations are not

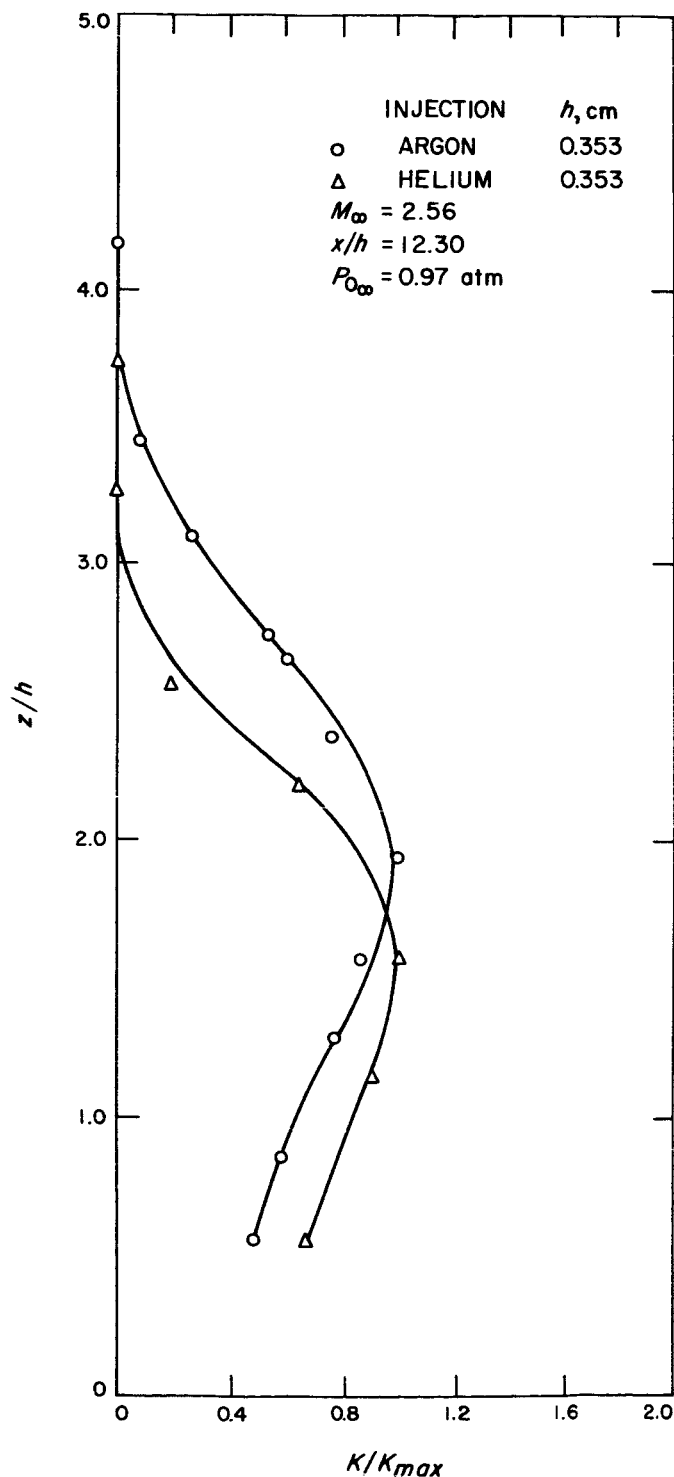


Fig. 15b. Comparison of argon and helium concentration data

directly comparable because of differences in molecular weight. The difference becomes more marked with increasing x/h . The nature of the difference is more clearly shown in Fig. 15b, in which the profiles for helium and argon at $x/h = 12.3$ are compared with the concentration values normalized by the maximum value. The curves are similar, but the helium profile is lower than that for argon.

Although the general shapes of the curves shown in Fig. 15b are quite similar, such features as jet width and distance of maximum concentration line from the wall are definitely smaller with helium as injectant. Hence, in the coordinates used here, the helium jet spreads more slowly than the argon jet.

Measurements made in the JPL facility are presented in Fig. 16a through 16d, in which data are given for helium and argon injection, and for Mach numbers 2.61 and 3.50. Fewer data points were obtained, and measurements are shown only for $x/h \approx 12$ and ≈ 20 . The data at Mach number 2.61 and $x/h = 12.3$ are compared in Fig. 16a with those obtained in the Caltech facility. The primary difference between the test conditions is that the ratio of penetration height to boundary-layer thickness h/δ is about 1 for the Caltech tests and about 1.7 and 3.4 for the JPL work. The data agree roughly at $x/h = 12$, but the curves corresponding to larger values of h/δ are slightly fuller near the wall, and it seems reasonable to ascribe this difference to a boundary-layer effect. Some data were also obtained for injection at Mach number 3.50. These are qualitatively similar to data already discussed. However, as the Mach number is increased, the spreading of the jet appears to be reduced somewhat.

To summarize the results of the concentration measurements, argon data have been presented for stagnation-pressure ratios that give about a 2.2:1 change in penetration height. The normalized concentration profiles shown in Fig. 11-14 are almost identical over this scale change. These data are also insensitive to the state of the boundary layer, since both laminar and turbulent layers are included. Hence, it is apparent that the scaling rule given by Eq. (6) is valid for the mixing process, too, when a single injectant is considered and when changes in scale by not more than a factor of 2 are considered; the good agreement of the data suggests that much larger changes could be adequately treated. There is a suggestion that the boundary-layer thickness may have a secondary effect on the profiles.

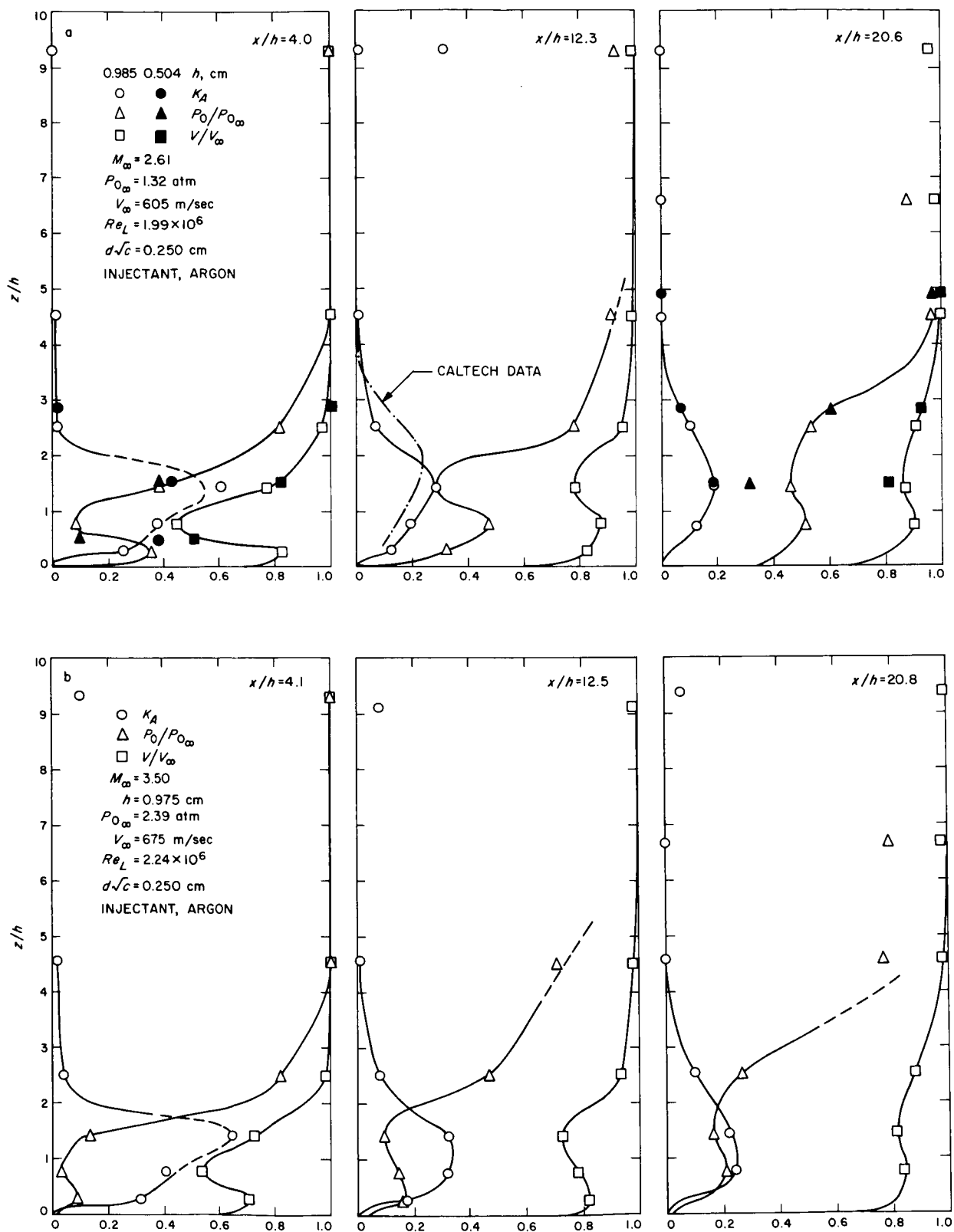


Fig. 16. Concentration, total-pressure, and velocity profiles in the plane $(y/h) = 0$, flat-plate data, turbulent boundary layer

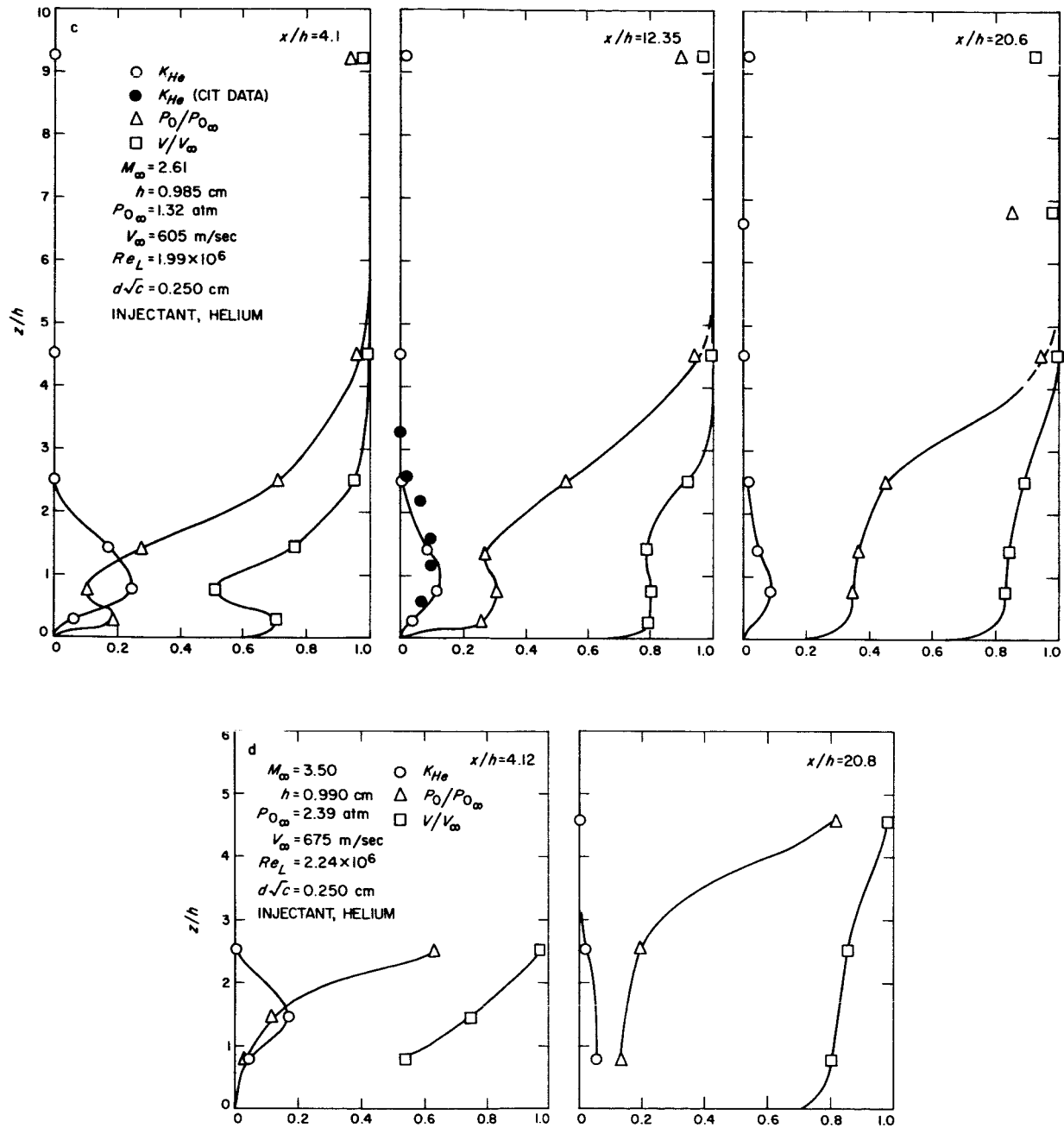


Fig. 16 (Cont'd)

D. Velocity and Total-Pressure Profiles

Measurements made in the Caltech facility (Ref. 2) for argon injection are presented in Fig. 17-20, which give velocity, Mach number, and total-pressure profiles normalized by the respective free-stream values. A single set of injection and free-stream conditions was maintained, and data are presented for four values of x/h between $x/h \approx 8$ and $x/h \approx 15$. At each axial station, data are

given at the centerline and at two off-axis positions. The argon-concentration data presented earlier were used to compute the effective specific heat ratio and molecular weight for each of the velocity, total-pressure, and Mach number data points. For the values of x/h at which argon concentration data had not been obtained the available concentration data were linearly interpolated or extrapolated. The results of these interpolations or extrapolations are presented as solid lines without data points

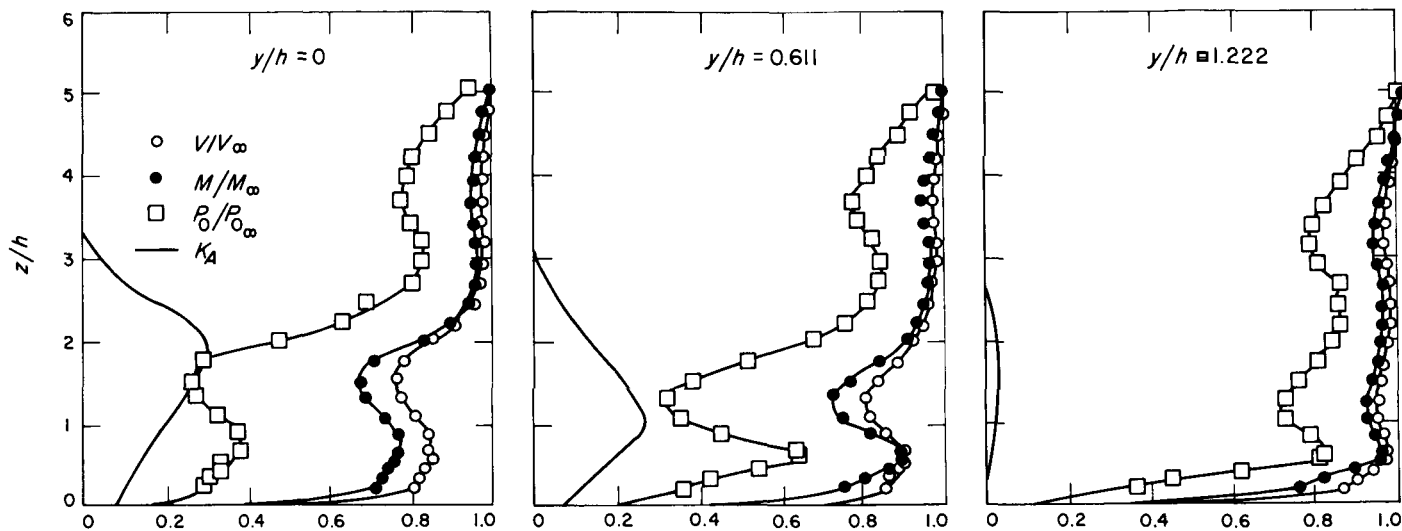


Fig. 17. Velocity, Mach number, and total pressure profiles with argon as injectant for $(x/h) = 8.49$; $M_\infty = 2.61$; $V_\infty = 585$ m/sec; $P_{0\infty} = 73.69$ cm Hg; $(P_{0j}/P_{0\infty}) = 7.77$; and $h = 0.5202$ cm

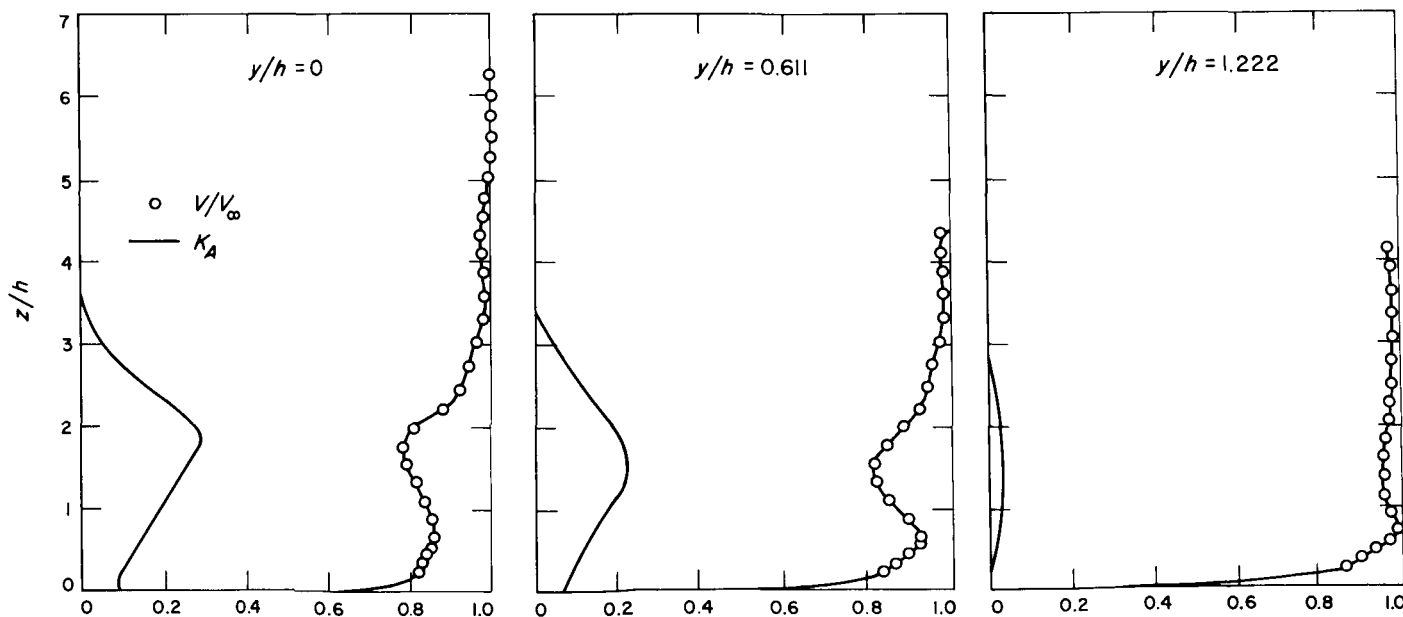


Fig. 18. Velocity profiles with argon as injectant for $(x/h) = 10.49$; $M_\infty = 2.61$; $V_\infty = 585$ m/sec; $P_{0\infty} = 73.69$ cm Hg; $(P_{0j}/P_{0\infty}) = 7.77$; and $h = 0.5202$ cm

in Fig. 17-20. The velocity, total-pressure, and Mach number profiles were found to be very insensitive to errors in argon concentration in the concentration range encountered, so that the interpolated or extrapolated values appeared to be quite satisfactory.

The local total pressure and Mach number were calculated with the assumption that the local static pressure was constant and equal to its value at the wall. Examination of wall static-pressure data shows the static pressure to be approximately constant and equal to the

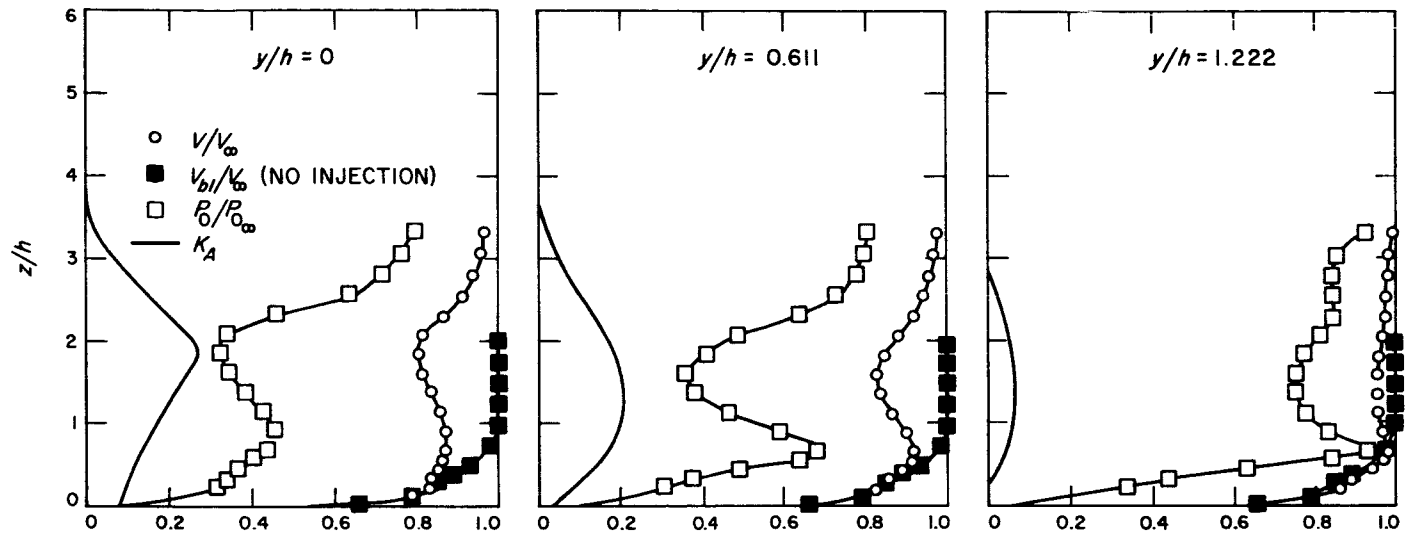


Fig. 19. Velocity and total-pressure profiles with argon as injectant and velocity profiles without injection for $(x/h) = 12.49$; $M_\infty = 2.61$; $V_\infty = 585$ m/sec; $P_{0_\infty} = 73.69$ cm Hg; $(P_{0_j}/P_{0_\infty}) = 7.77$; and $h = 0.5202$ cm

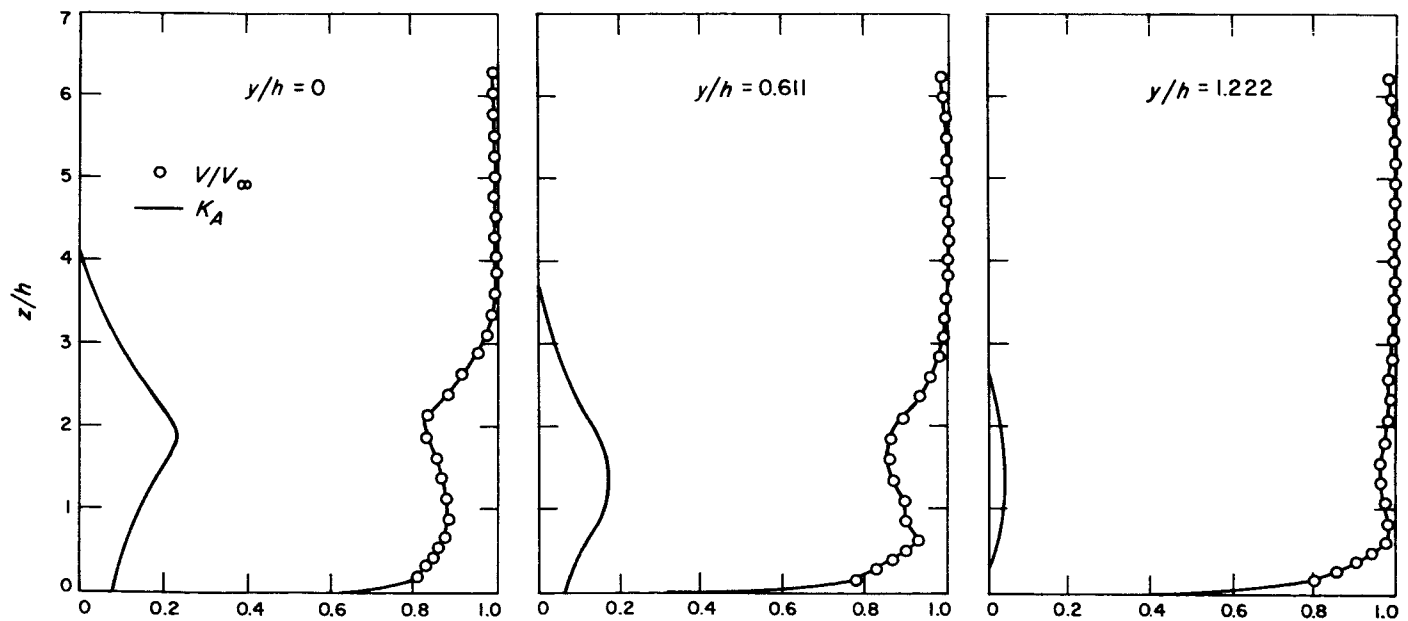


Fig. 20. Velocity profiles with argon as injectant for $(x/h) = 15.49$; $M_\infty = 2.61$; $V_\infty = 585$ m/sec; $P_{0_\infty} = 73.69$ cm Hg; $(P_{0_j}/P_{0_\infty}) = 7.77$; and $h = 0.5202$ cm

undisturbed static pressure for x/h greater than 8 and for y/h in the range of zero to at least 4.3. Because the wall static pressure was found to be nearly constant in this downstream region, the assumption of constant static pressure away from the wall is a reasonable one in this limited region.

Note that each of the velocity, total-pressure, and Mach number profiles in Fig. 17-20 exhibits two maxima at most locations and that these occur at the same values of z/h . Also, the curves have a minimum near the maximum value of argon concentration. This is reasonable, because the velocity which the argon would attain by expanding isentropically from its stagnation pressure to the free-stream static pressure is only about 89% of the free-stream velocity for this set of test conditions. However, note that the velocity attained is much less than 90% of V_∞ and the total pressure of the argon-air mixture is only about 25% of the free-stream pressure and about 3% of the P_{0j} . The very large total-pressure defect in this region indicates that most of the total pressure of the injectant has been dissipated in the turning process. Indeed, the observed velocity profile would be roughly given by assuming constant pressure mixing between the primary flow and the appropriate mass fraction of argon with no momentum in the x -direction.

The velocity profiles (Fig. 17-20) approach the free-stream velocity with increasing x/h , but there is still a substantial velocity defect at $x/h \approx 15$, and $y/h = 0$ and 0.611. In Fig. 19, boundary-layer profiles with no injection (the solid points) are superimposed upon the velocity profiles obtained with injection, and it can be seen that the flow near the wall is characteristic of the undisturbed boundary layer at the two off-axis stations and somewhat less so at the axis. Similar velocity and total-pressure data were obtained in the JPL facility for the conditions at which concentration data were presented. The results are quantitatively similar to those discussed above.

A composite plot of argon-concentration contours and total-pressure contours at $x/h \approx 12$ is given in Fig. 21. The concentration contours are the same as those in Fig. 14 for this axial station. It can be seen that the shapes of these contours are similar, but the kidney shape is somewhat less pronounced in the case of the total-pressure contours. The shape of the total-pressure contours is a further indication of the presence of the two vortices mentioned earlier. It is clear from Fig. 21 that the momentum defect is closely associated with the injectant flow.

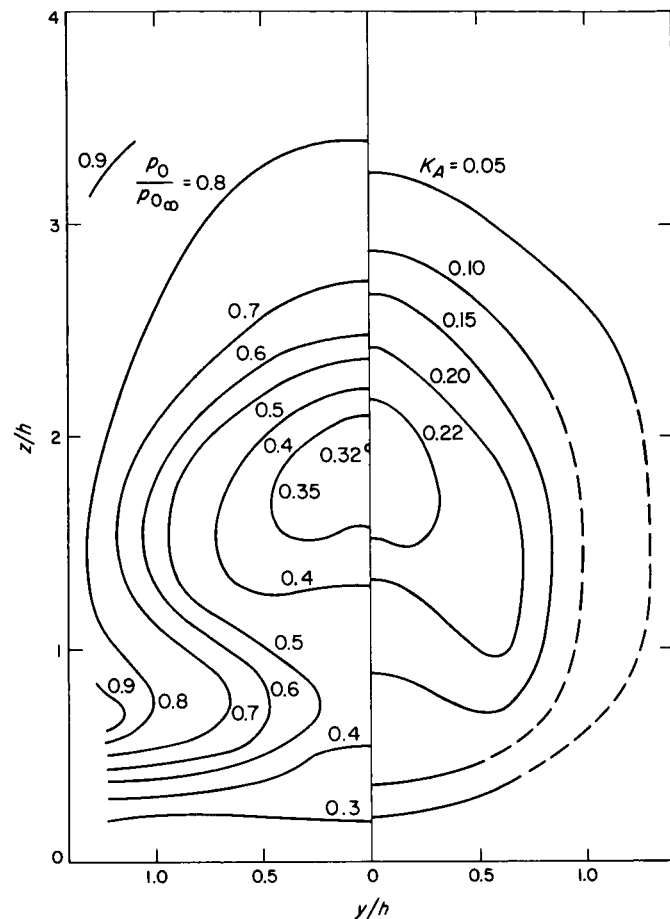


Fig. 21. Concentration and total-pressure contours with argon as injectant; $M_\infty \approx 2.61$; $P_{0\infty} \approx 0.974$ atm; $(P_{0j}/P_{0\infty}) = 7.77$; $h \approx 0.52$ cm; $(x/h) \approx 12$

E. Wall-Pressure Distribution

The experimental results discussed up to this point concern the gross features of the flow field produced by secondary injection. It has been shown that these features are approximately independent of the state of the boundary layer and of the boundary-layer thickness for values of h as small as the boundary-layer thickness or somewhat less, and that a simple model of the flow leads to the calculation of a single characteristic dimension, h , which is a satisfactory scaling parameter. In contrast, when examining the flow field near the wall, the state of the boundary layer is very important because of its influence on the interaction between the bow shock and the boundary layer.

For example, when the layer is laminar, the interaction between the bow shock and the boundary layer causes the layer to separate far upstream of the interaction

region, and the separation angle is quite small (see Fig. 4). However, when the layer is turbulent, the separation point is much closer to the interaction region, and the separation angle is much larger. Hence, it is evident that the static-pressure distribution on the wall under the separated regions will be quite different for turbulent and laminar boundary layers. In addition to the state of the boundary layer, two other parameters might be expected to play an important role in fixing the pressure distribution. These are the boundary-layer thickness and the injector diameter.

In this Section, it will first be shown to what extent simple scaling with h leads to a correlation of the data for laminar and turbulent boundary layers. Then the influence of the ratios of injector diameter to h and boundary-layer thickness to h will be examined. Before examining the influence of various parameters on the wall-pressure distribution, it will be useful to examine

the typical set of data shown in Fig. 22a and 22b. Here, a pressure map and the pressure distribution along the x -axis are given for a turbulent boundary layer and a Mach number of 2.61. The injectant is nitrogen and the ratios of penetration distance to hole size and boundary-layer thickness are 4.03 and 2.9. In both figures, pressures are normalized by the free-stream static pressure and all scales are normalized by calculated values of the penetration height.

Consider first the pressure map in Fig. 22a. The pressure rises beneath the intersection of the shock system and the wall. The rise is highest just upstream of the injector and dies off as the distance along the shock from the forward stagnation point increases. Between this region of high pressure and the centerline, $y = 0$, the gas pressure drops below the ambient value. The pressure decrease is most marked just downstream of the injector and dies out as the distance from the injector

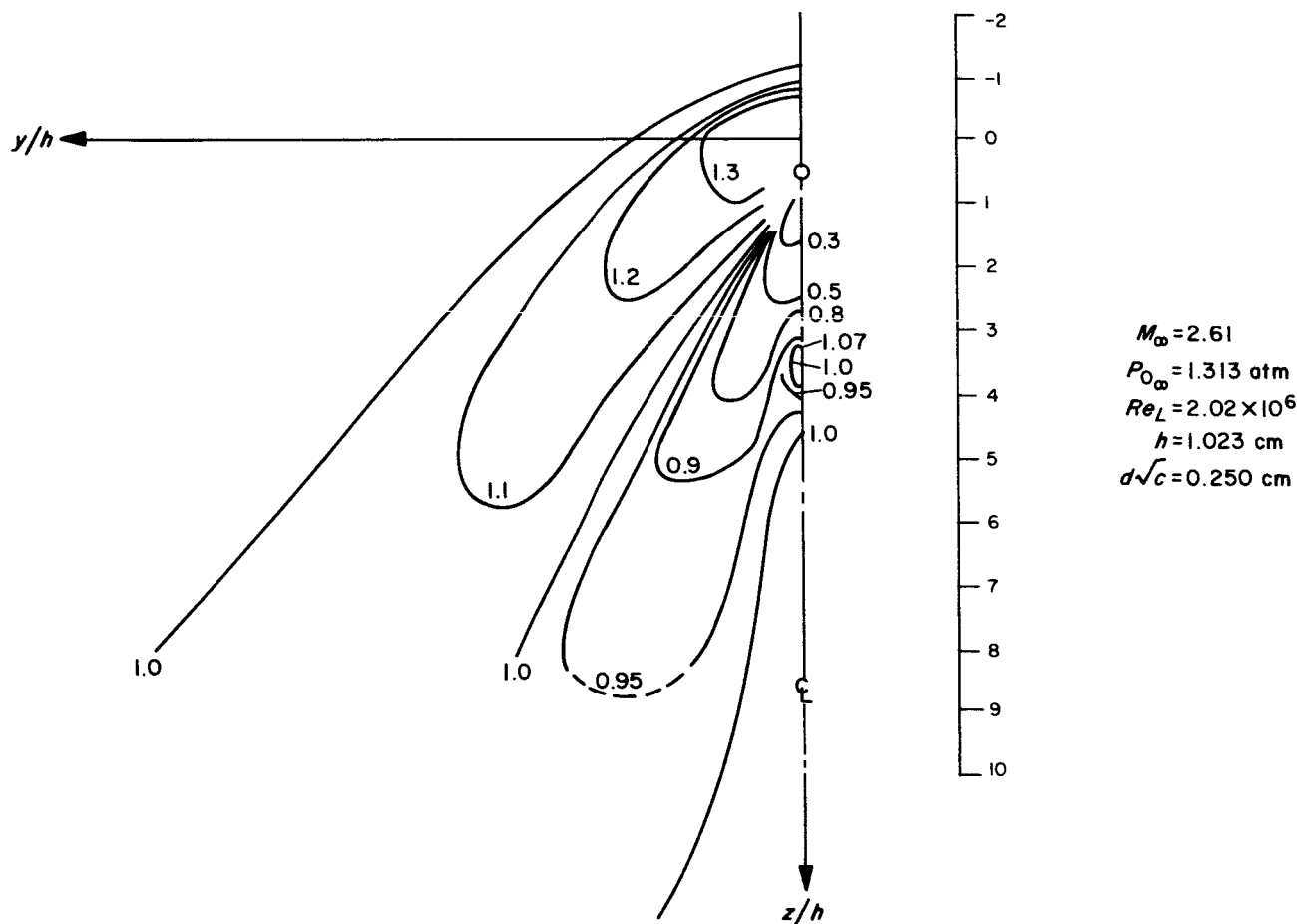


Fig. 22a. Pressure map for flat-plate measurements at $M_{\infty} = 2.61$ with nitrogen as injectant; turbulent boundary layer

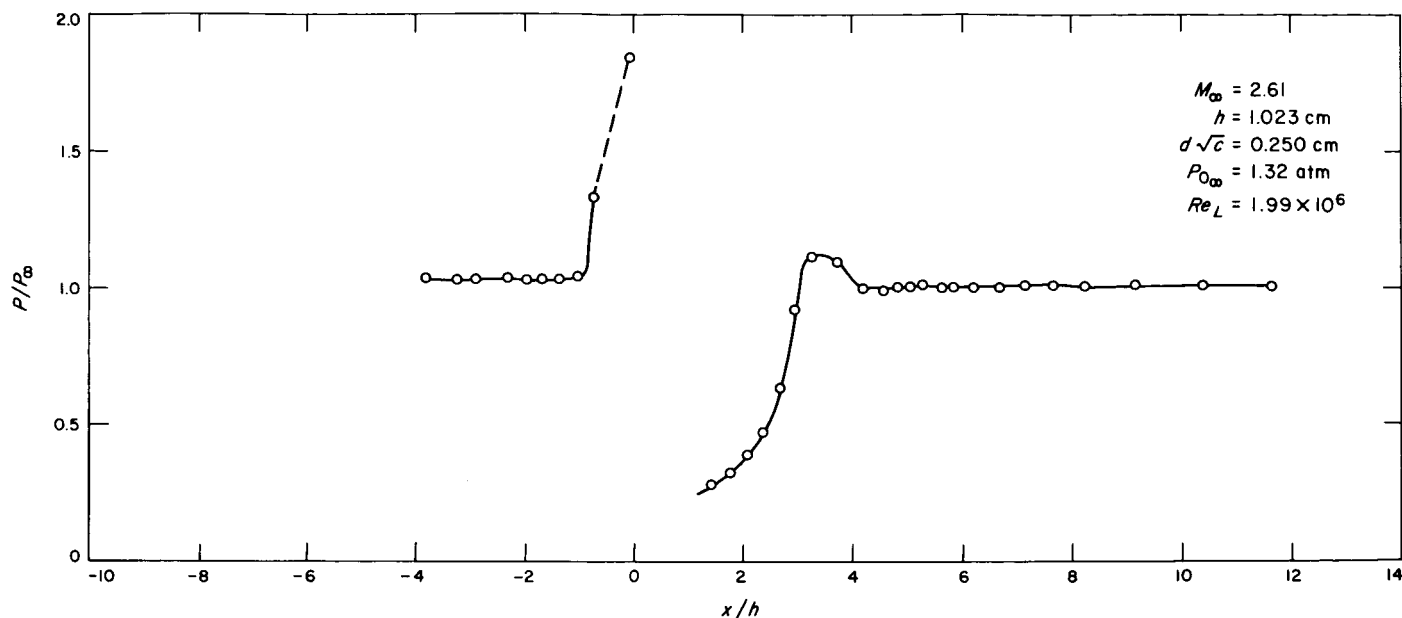


Fig. 22b. Flat-plate static-pressure measurements in the plane $(y/h) = 0$ with nitrogen as injectant; turbulent boundary layer

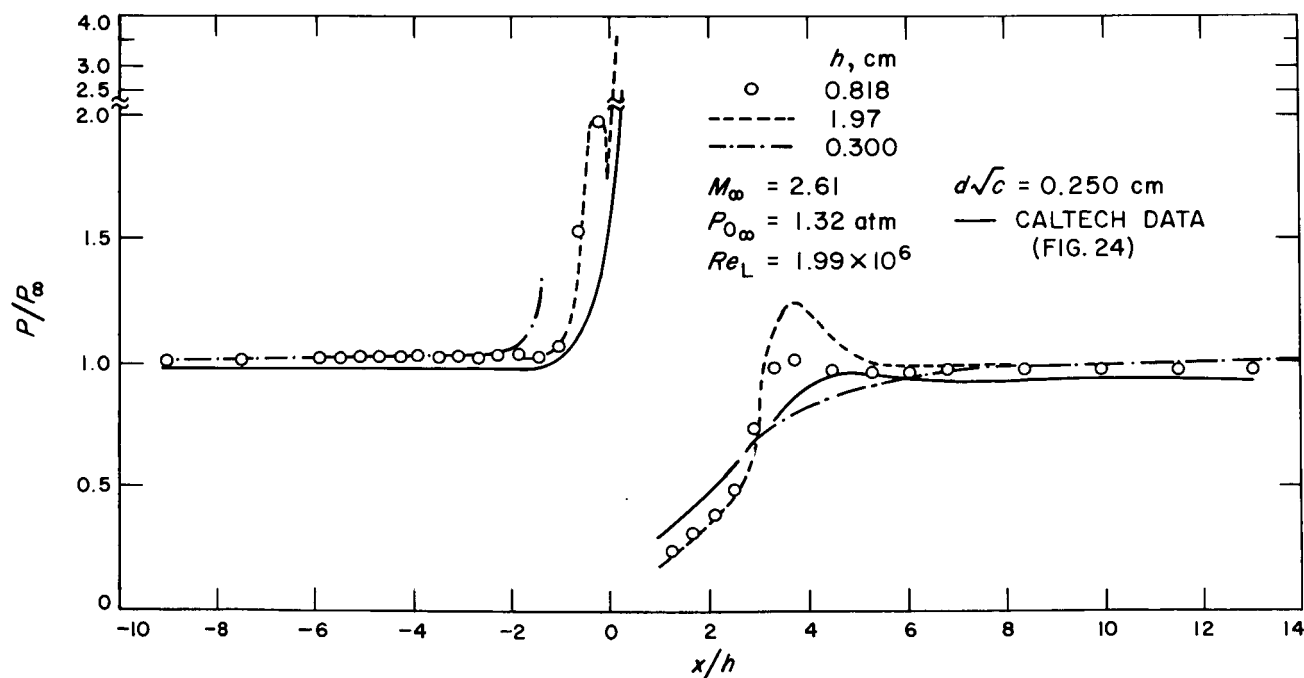


Fig. 23. Flat-plate static-pressure measurements in the plane $(y/h) = 0$ at $M_\infty = 2.61$ with nitrogen as injectant; turbulent boundary layer

increases. Finally, some distance downstream of the injector, a spreading region of ambient pressure lies on either side of the centerline and forms the downstream boundary of the low-pressure region. Although details vary with experimental conditions, this pressure map is

typical of all those obtained in the present experimental program.

The pressure variation is most rapid along the x -axis and hence pressure data obtained along this axis can be

used to compare the distributions obtained under various test conditions. A plot of this type is shown in Fig. 22b for the test conditions given in Fig. 22a. The pressure rise upstream of the injector is very rapid, and because of the finite number of pressure taps in this region, it is not always precisely defined. The pressure gradient downstream of the injector is smaller and is much better defined by the data.

In presenting the data obtained along the x -axis (Fig. 22b), it was not always possible to show all of the data points or even data from all of the injectant conditions tested. To keep the figures intelligible, representative injection conditions are used (usually maximum, intermediate, and minimum injection pressure) and in some of the figures only one set of data points is shown. The scatter in the data for which only average curves are given is similar to that of the data which are presented.

To check the scaling of the wall-pressure field with penetration height, plots of the form shown in Fig. 23 were compared for data obtained at a fixed Mach number

and a range of hole sizes, injectant total pressure and molecular weight, and free-stream total pressure. Data obtained in the Caltech facility at Mach number 2.56 are shown in Fig. 24. Upstream of the injector located at $x/h \approx 0.49$, the data are scattered partly due to experimental technique and partly due to the dependence of the separation phenomena on the state of the boundary layer. Downstream of the injector, the pressure data are again somewhat scattered, but the scatter in values of x/h at which the pressure returns to the ambient value is only about 30%. This is certainly small compared to the 7:1 variation in penetration heights used in these experiments. Off-axis data presented in Fig. 25 and 26 show a similar agreement. It is evident that simple scaling of the pressure field with the penetration height gives a good general correlation of the data and also that certain discrepancies in scaling are present.

Examination of the JPL data for which more detailed pressure distributions could be obtained (Fig. 23, 27-32) gives the same results. Consider Fig. 23 in which data obtained at Mach number 2.61 for a turbulent boundary

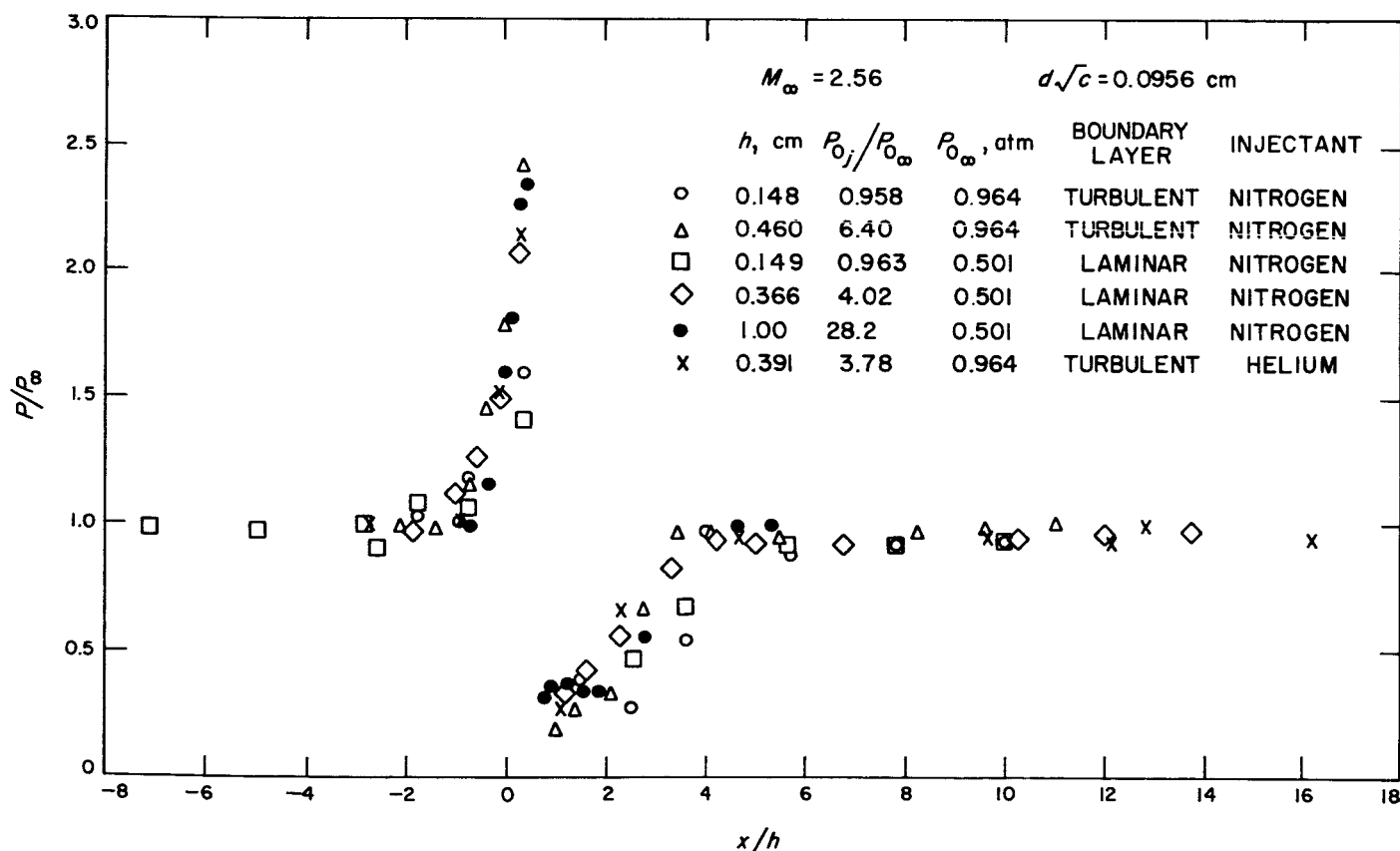


Fig. 24. Nozzle-wall static-pressure measurements in the plane $(y/h) = 0$ with nitrogen and helium as injectant

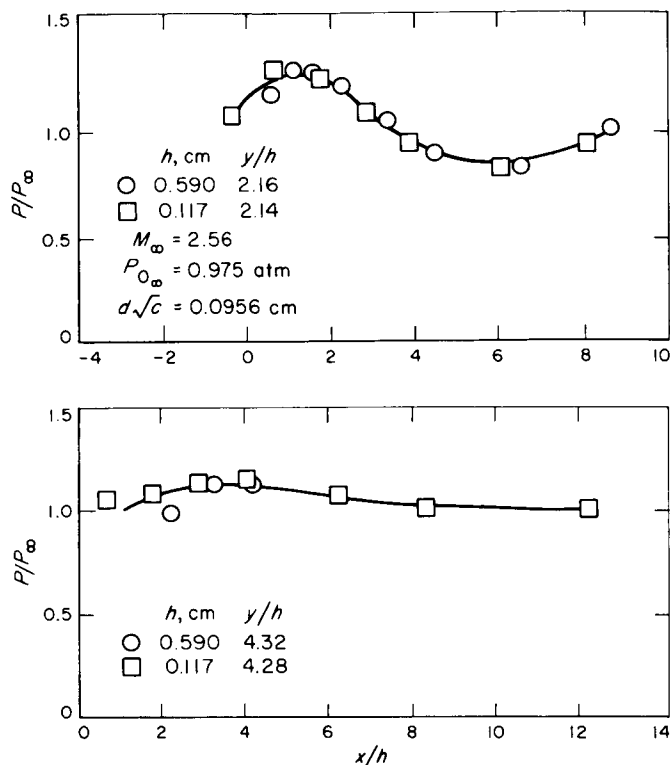


Fig. 25. Nozzle-wall static-pressure measurements in off-axis planes with nitrogen as injectant, $(y/h) = \text{constant}$

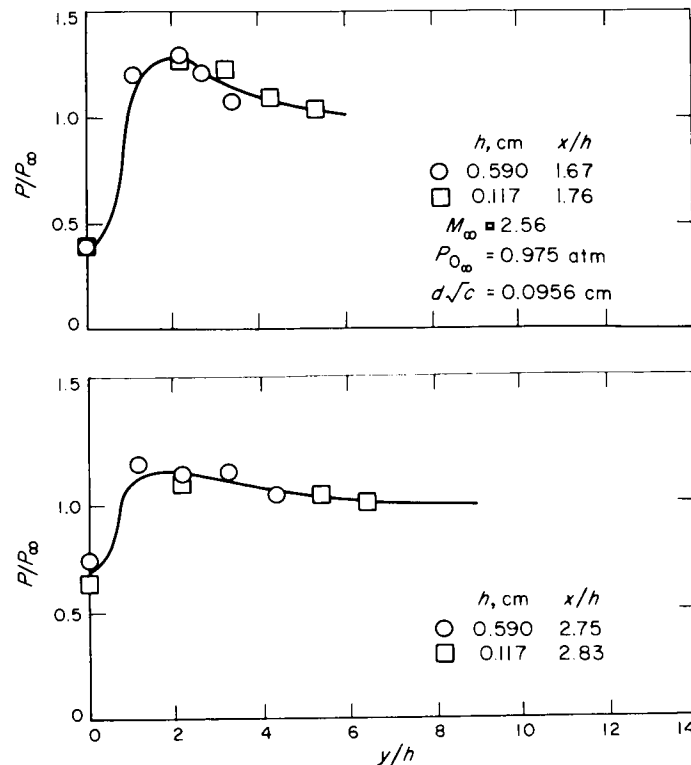


Fig. 26. Nozzle-wall static-pressure measurements in off-axis planes with nitrogen as injectant, $(x/h) = \text{constant}$

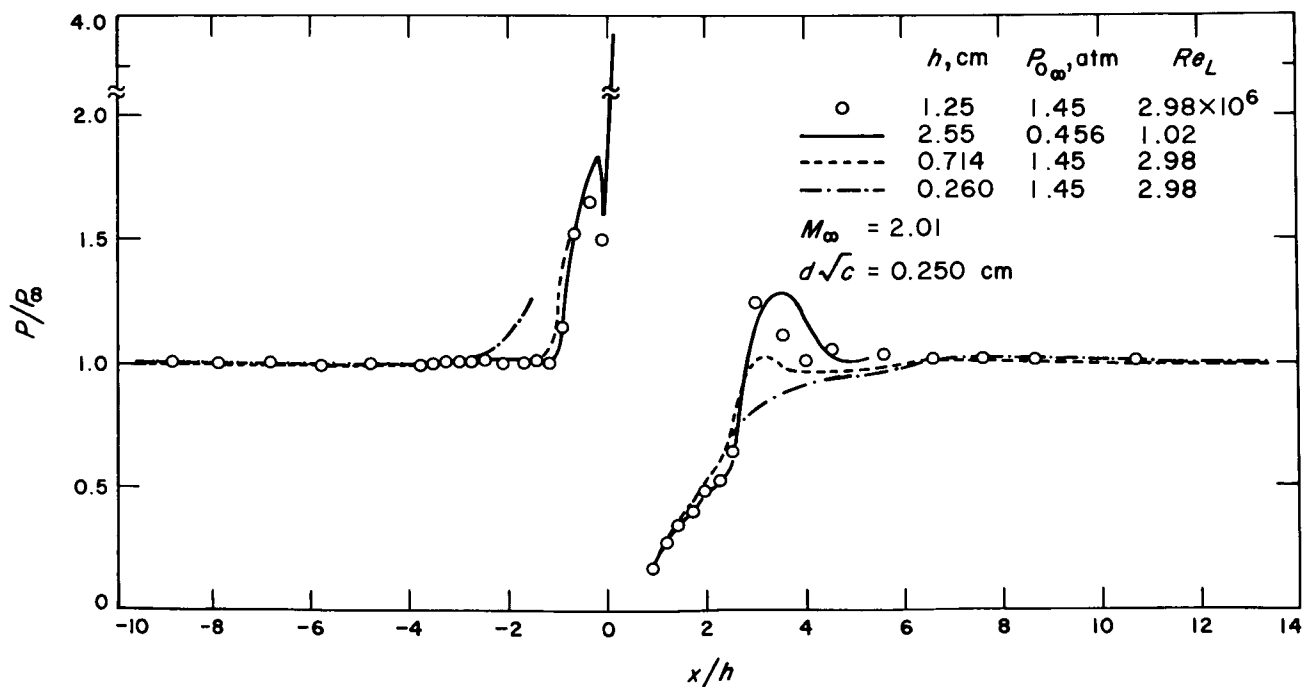


Fig. 27. Flat-plate static-pressure measurements in the plane $(y/h) = 0$ at $M_\infty = 2.01$ with nitrogen as injectant; turbulent boundary layer

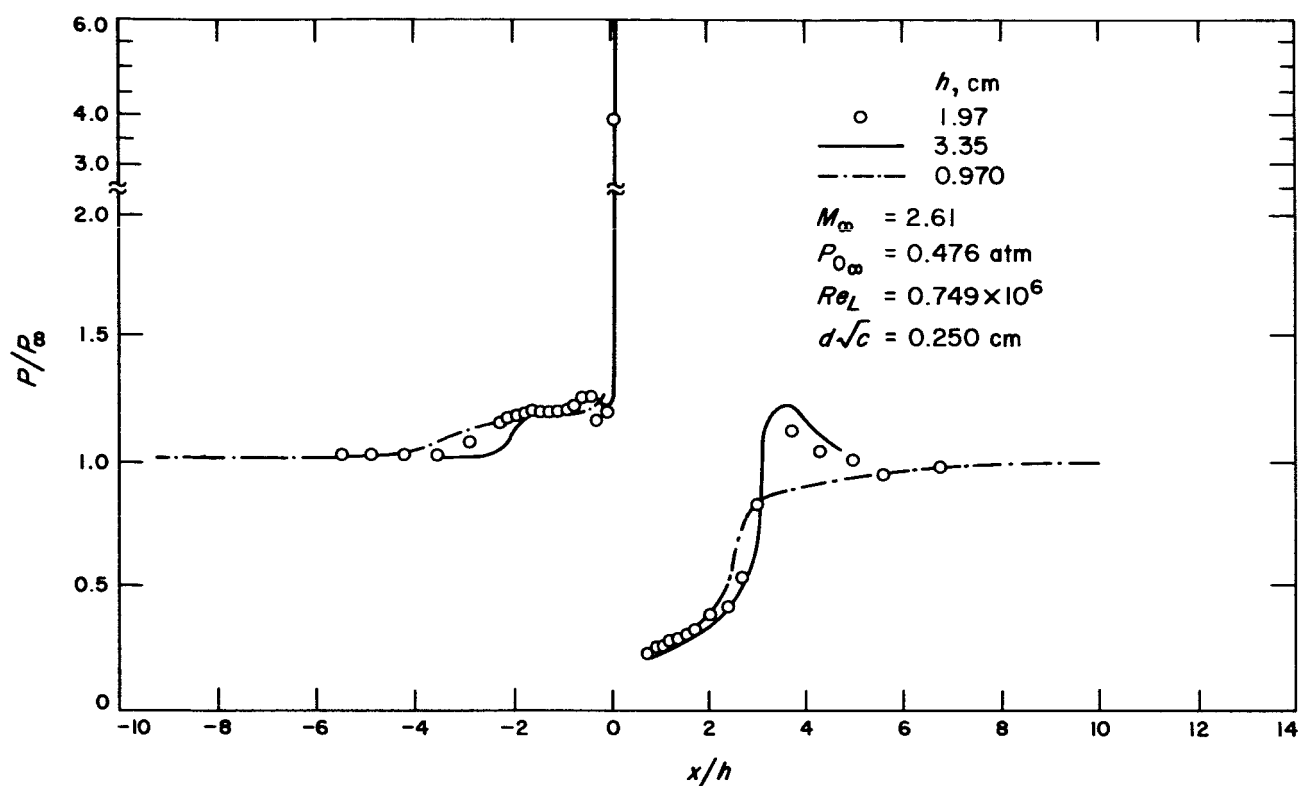


Fig. 28. Flat-plate static pressure measurements in the plane $(y/h) = 0$ at $M_\infty = 2.61$ with nitrogen as injectant; laminar boundary layer

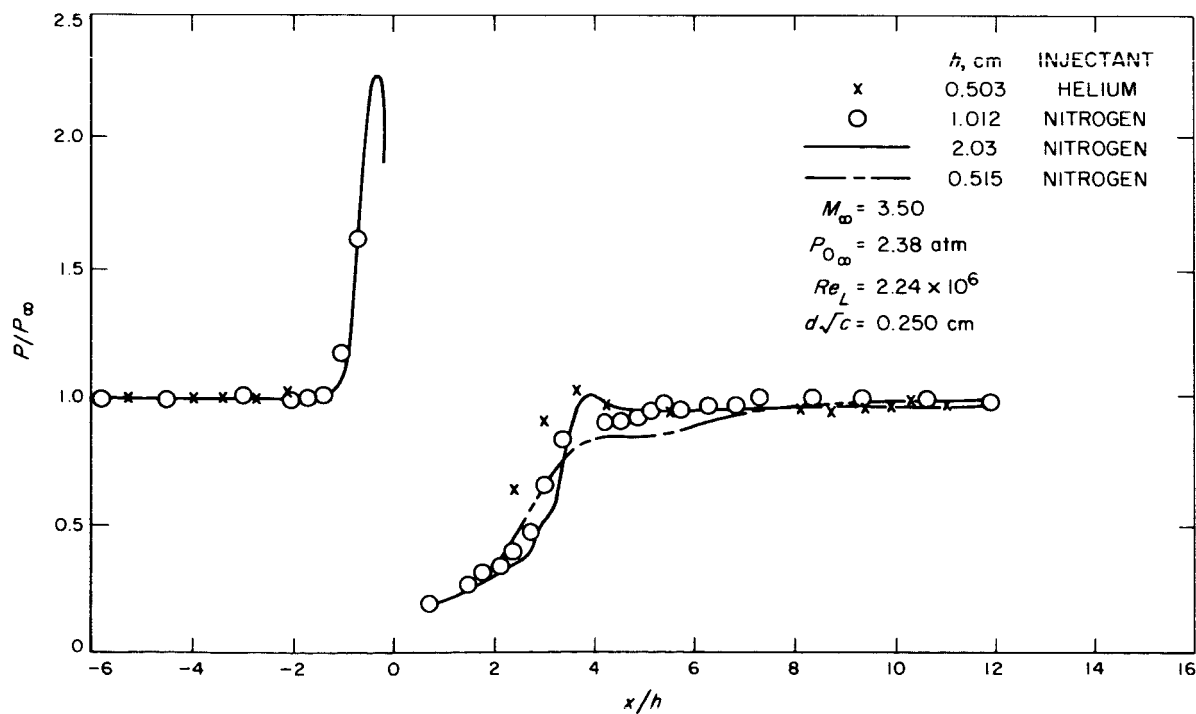


Fig. 29. Flat-plate static-pressure measurements in the plane $(y/h) = 0$ at $M_\infty = 3.50$; turbulent boundary layer

layer are shown. The data fall into two groups: first, for $h > 0.4$ cm, good correlation of the data was found. These data are represented by the data for $h = 0.818$ and 1.97 in Fig. 23. Second, when $h < 0.4$ cm, the scaling failed in the region upstream of the injector. As h decreased, the value of x/h at which separation started became more negative. These data are represented by the data for $h = 0.30$ cm given in Fig. 23. Data from the Caltech facility are also shown for comparison.

The only region in which the "large" h data do not scale well is in the reattachment region around $x/h \approx 4$. There is a systematic variation in the maximum pressure obtained in this region. As h increases, the peak pressure in this region also increases.

The results discussed in the last few paragraphs are typical of those obtained at Mach numbers of 2.01, 3.50, and 4.54. Data for these Mach numbers and a turbulent boundary layer are shown in Fig. 27, 29 and 31.

Note that the pressure distribution along the x -axis is surprisingly similar for this range of Mach numbers. The static pressure first returns to the ambient value in the neighborhood of $x/h \approx 2.7$ at Mach 2.01 and $x/h \approx 3.5$ at Mach 4.54. However, note that the pressure overshoot is most apparent for the lower Mach numbers and for large values of h , and that for the values of h obtained at Mach 4.54 no overshoot was obtained. In addition, the off-axis data (Fig. 25 and 26) show that for $y/h > 1.5$ the differences became negligible again at all Mach numbers. In general, the correlation between the off-axis data was similar to that presented in Fig. 23 and 27-32 for the x -axis data.

When the boundary layer is turbulent, scaling appears to be excellent so long as h is greater than a lower limit of about 0.5 cm with the exception of the variation in the small region about $x/h \approx 4$. However, scaling for the laminar case is less satisfactory. The problem is shown in Fig. 28, 30, and 32, in which data for Mach numbers

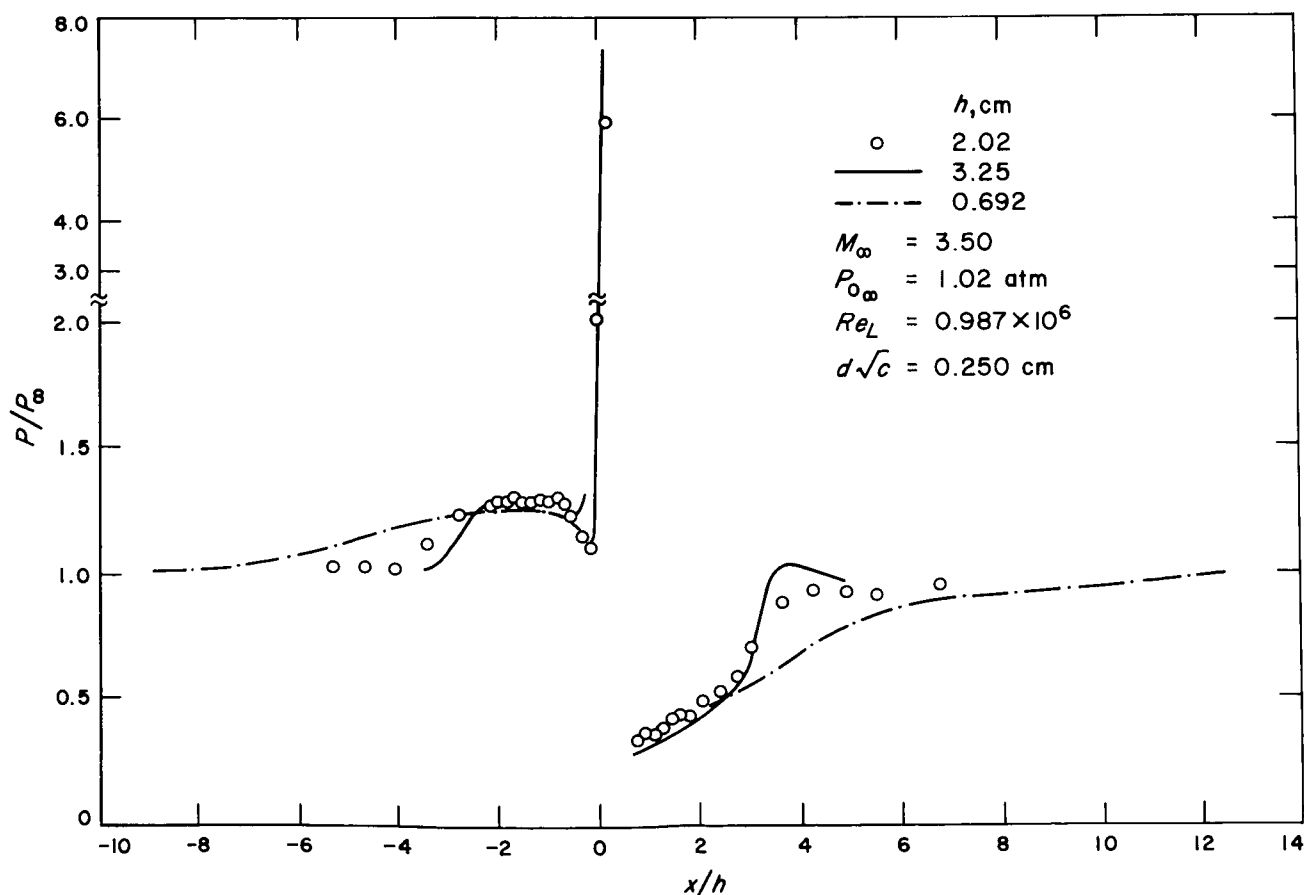


Fig. 30. Flat-plate static-pressure measurements in the plane (y/h) = 0 at $M_\infty = 3.50$ with nitrogen as injectant; laminar boundary layer

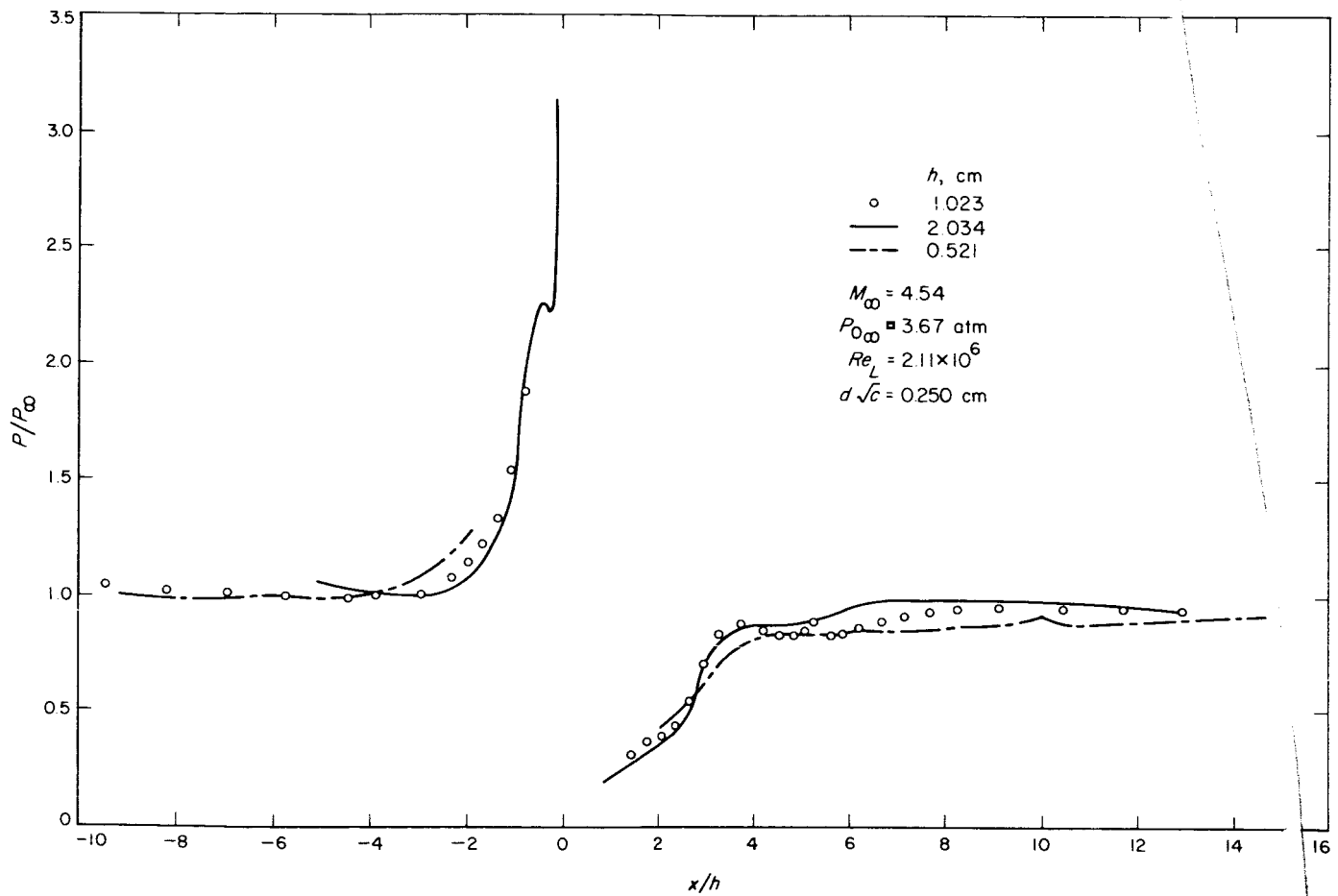


Fig. 31. Flat-plate static-pressure measurements in the plane $(y/h) = 0$ at $M_\infty = 4.54$ with nitrogen as injectant; turbulent boundary layer

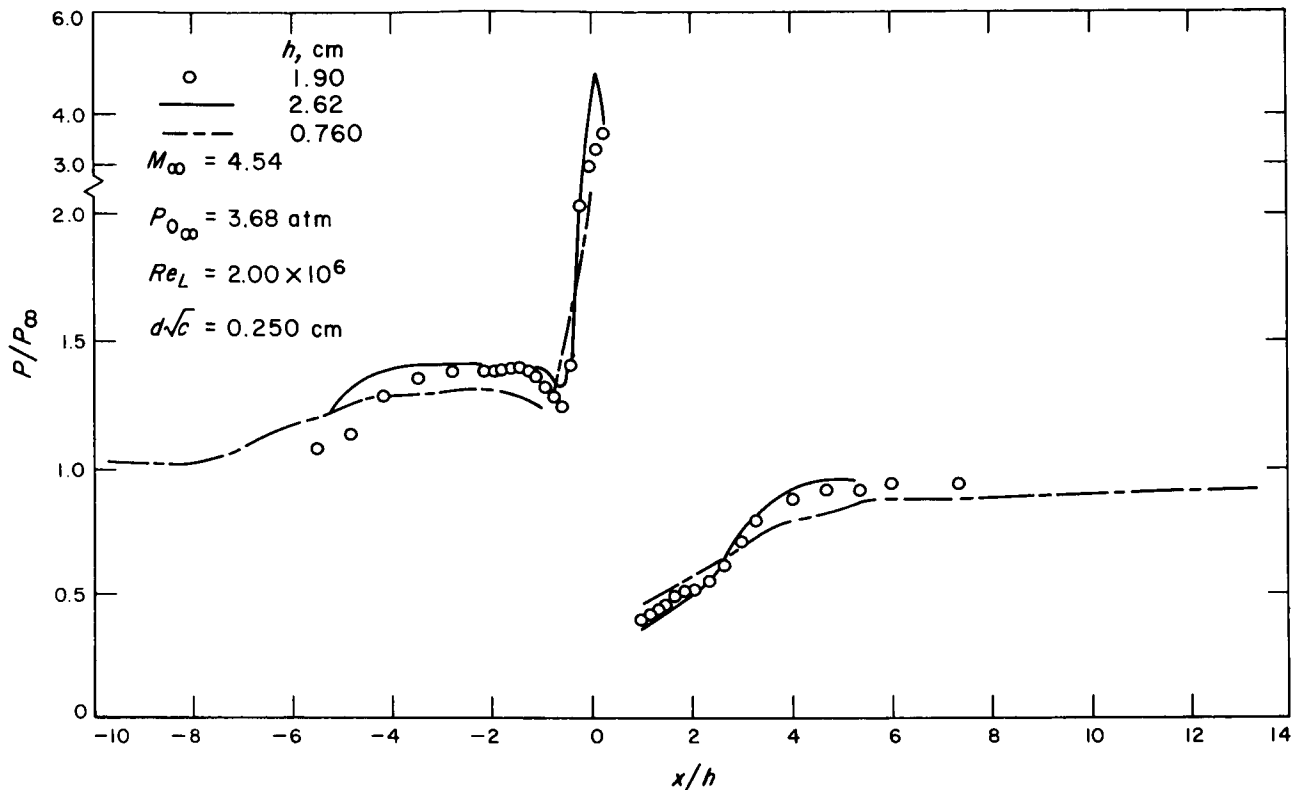


Fig. 32. Flat-plate static-pressure measurements in the plane $(y/h) = 0$ at $M_\infty = 4.54$ with nitrogen as injectant; laminar boundary layer

2.61, 3.50, and 4.54 are given. Downstream of the injector, the data correlate about as well as they did for the turbulent case and show the same systematic discrepancy in the reattachment region. However, upstream of the injector the data do not correlate at all. This is clearly due to the fact that the boundary-layer separation distance does not scale with h .

To supplement the pressure data discussed up to this point, pressure maps are presented in Fig. 22a and 33-36 for the range of test conditions shown in Fig. 27-32. In all cases, the data were obtained in the JPL facility. Note in particular that the region of pressure overshoot, shown for instance in Fig. 22a about the point $x/h = 3.5$, $y/h = 0$, is small and hence would not make a great contribution to the integrated value of pressure force on the wall.

In summary, these data indicate that for a turbulent boundary layer the proposed scaling procedure is accurate except (1) when h is "small" and (2) for the reattachment region around the point $x/h = 4$, $y/h = 0$. For the

laminar case, the pressures in the boundary-layer separation region do not scale properly, but farther downstream the flows are similar with the same exceptions noted for the turbulent case.

The value of penetration height at which scaling fails in the JPL tests was in the range of 0.1-0.3 cm. For these tests, the thickness of the boundary layer on the wall, δ , is about 0.3 cm, and in addition, the diameter d of the injection holes used in the experiments is about 0.250 cm. It is reasonable to expect that the proposed scaling procedure would begin to fail when either $h \leq \delta$ or $h \leq d$. Comparison of data obtained with small h and a range of hole sizes from $d \approx .076$ to 0.25 cm shows that the boundary-layer separation point begins to move forward when h/d approaches 1. For example, when $h = 0.30$ cm for the test conditions given in Fig. 23 and when $d = 0.250$ cm, the broken curve shown in Fig. 23 is obtained. A second test with the same boundary layer and with $h = 0.309$ cm but with $d = 0.076$ cm gave a distribution almost identical to the dashed curve in Fig. 23. Examples of pressure distribution obtained with these small-diameter

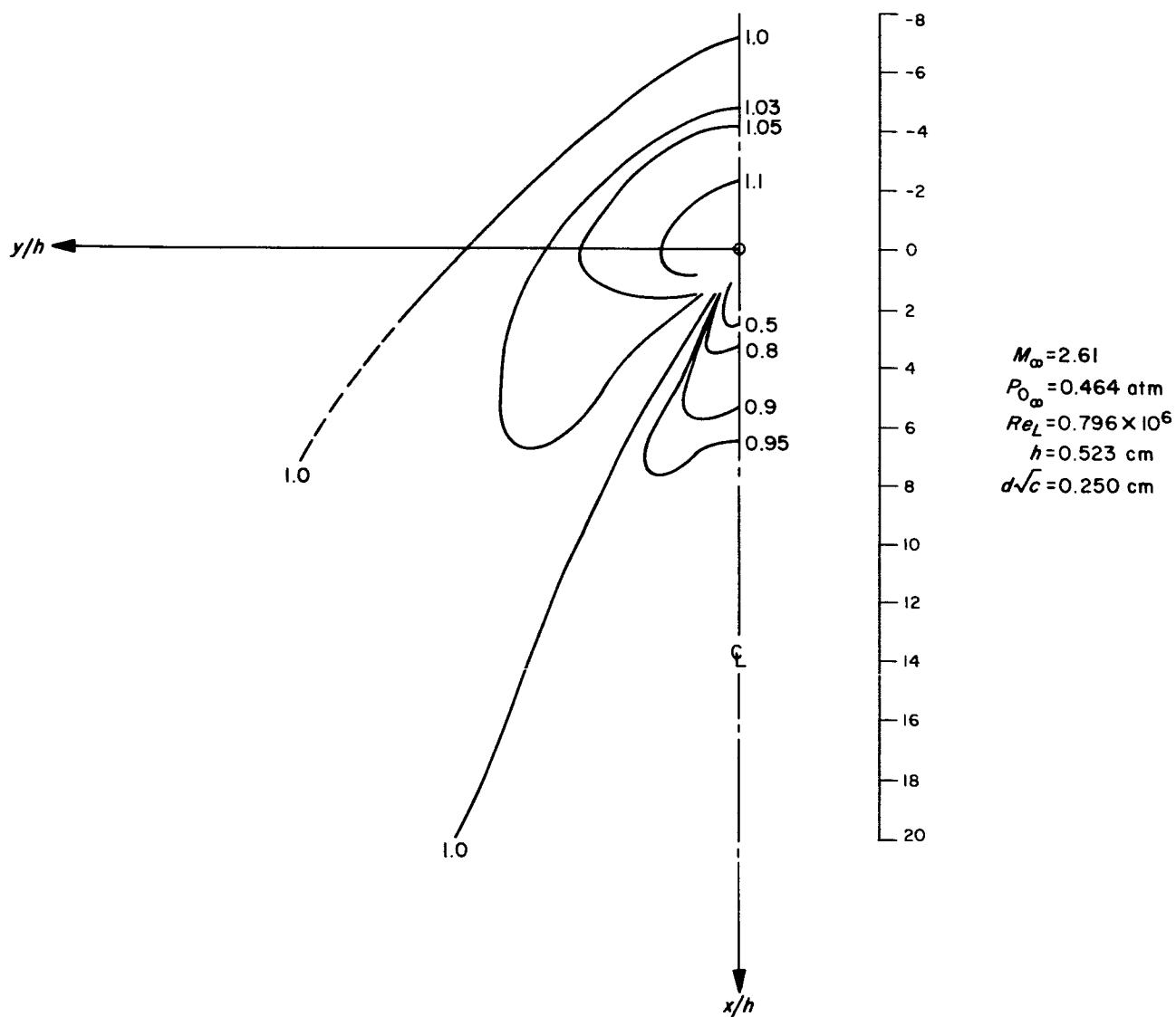


Fig. 33. Pressure map for flat-plate measurements at $M_\infty = 2.61$ with nitrogen as injectant; laminar boundary layer

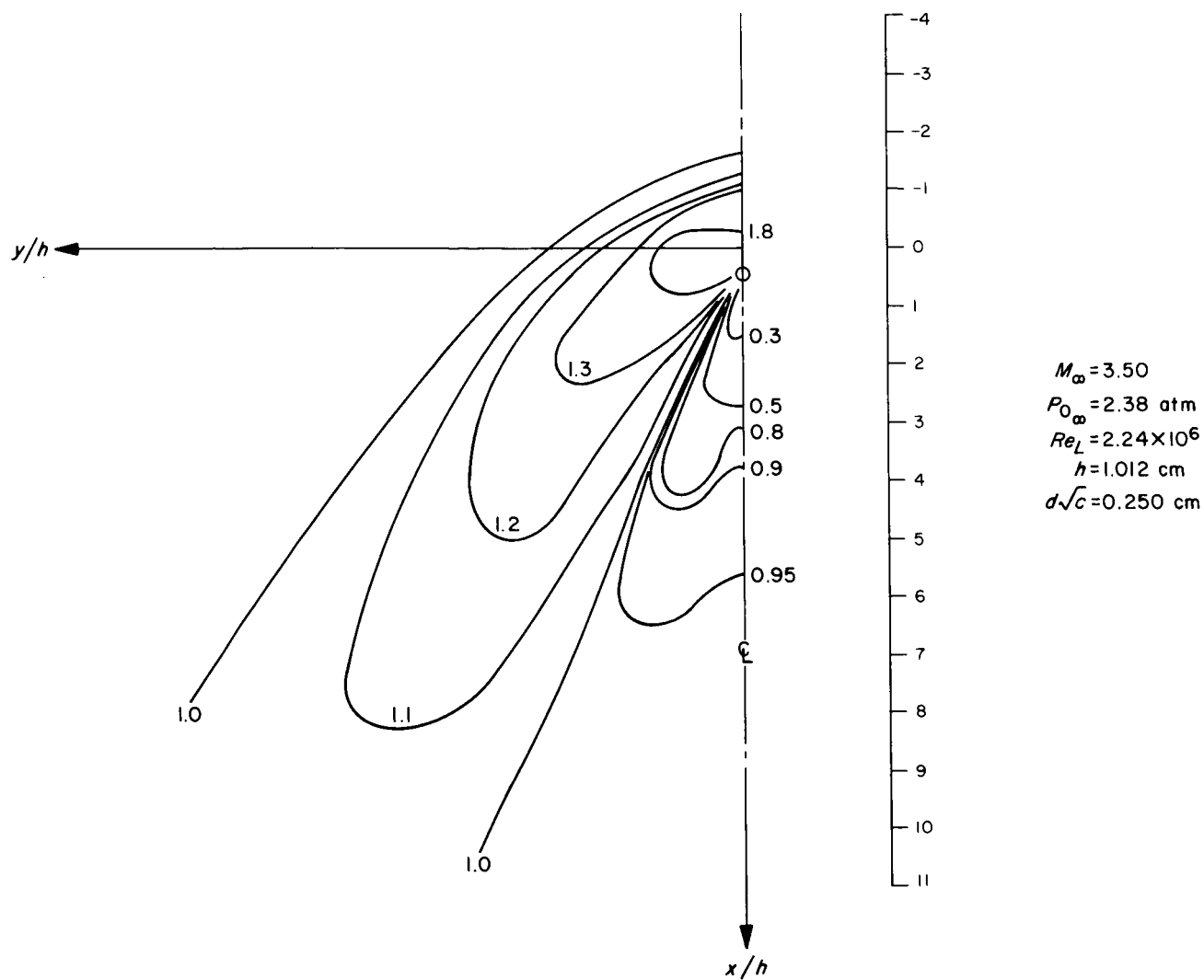


Fig. 34. Pressure map for flat-plate measurements at $M_\infty = 3.50$ with nitrogen as injectant; turbulent boundary layer

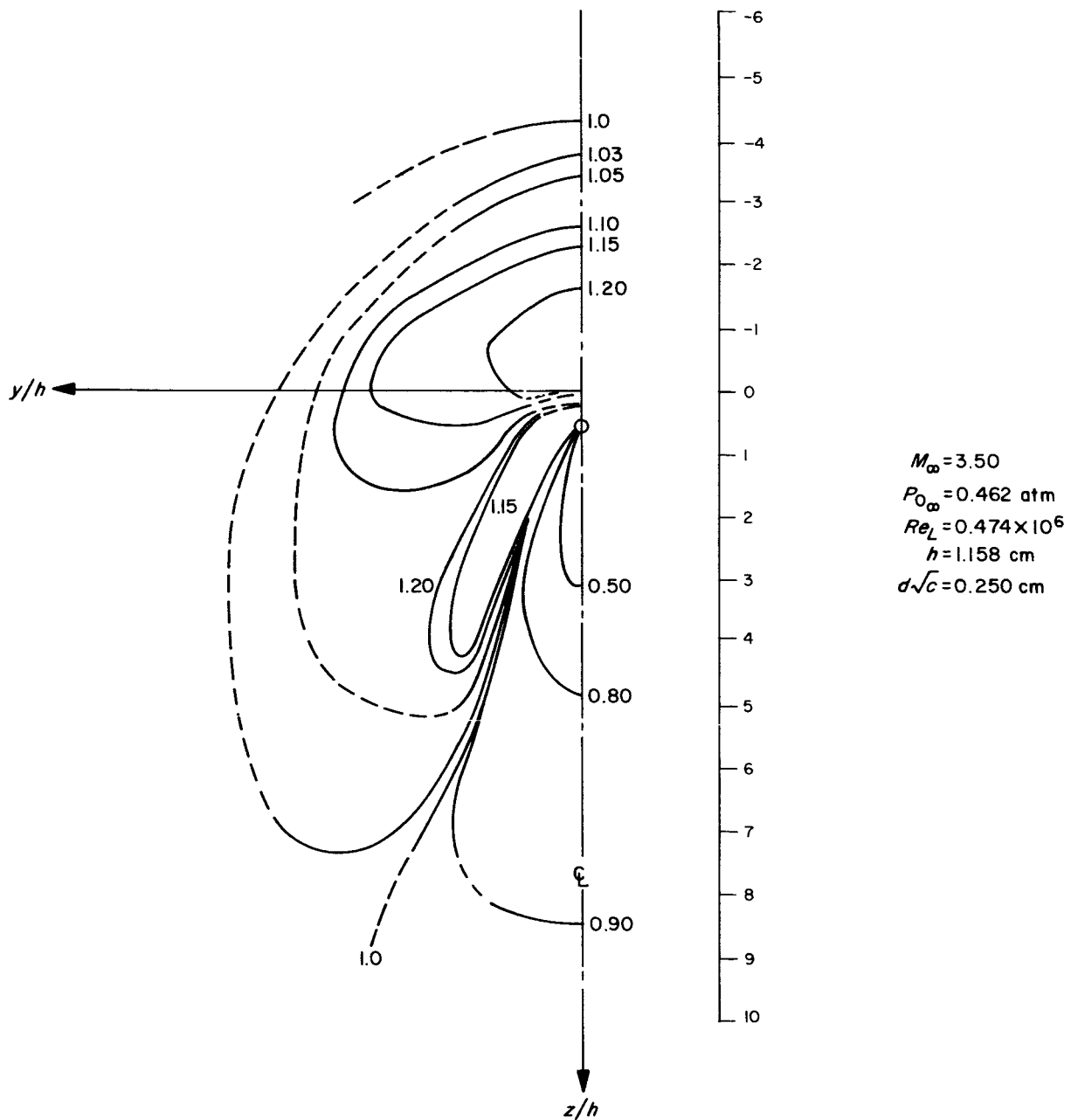


Fig. 35. Pressure map for flat-plate measurements at $M_\infty = 3.50$ with nitrogen as injectant; laminar boundary layer

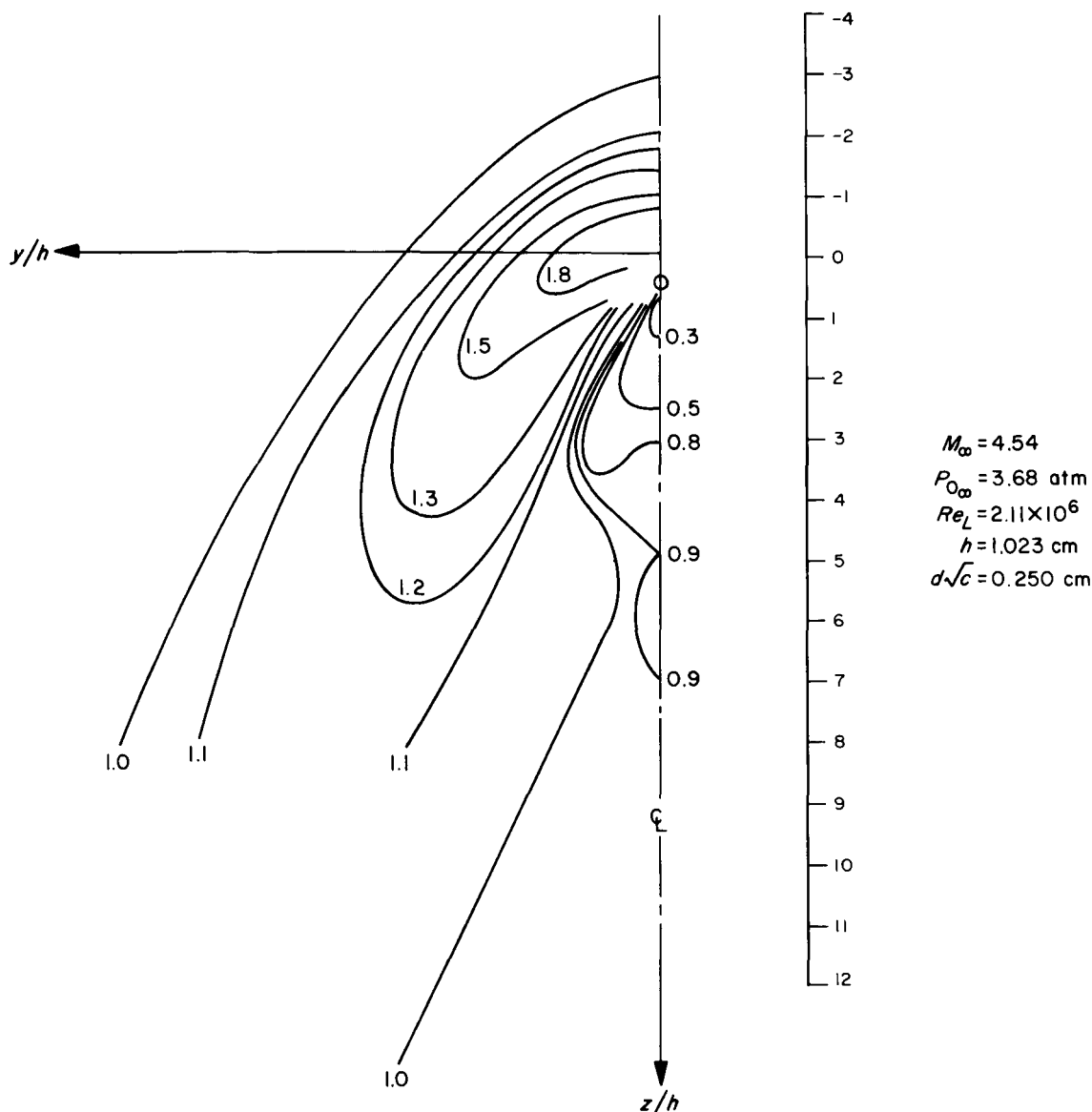


Fig. 36. Pressure map for flat-plate measurements at $M_\infty = 4.54$ with nitrogen as injectant; turbulent boundary layer

injectors, $d = 0.075 \text{ cm}$, are shown in Fig. 37a, b, and c, for a turbulent boundary layer about 0.5 cm thick. In all cases where it is possible to identify the upstream separation point, the normalized value agrees well with that with the "large" h data given in Fig. 37a and in previous figures. Hence, h/d appears to be the parameter that governs the observed phenomena, and when this parameter is close to or less than unity it is important in fixing the boundary-layer separation point.

This dependence on the ratio h/d is reasonable from the following point of view. The gases leaving the injec-

tor port have the shape of a frustum of a cone with the small end covering the port. As long as $h \gg d$, the geometry of the obstacle will be independent of d and hence the separation phenomena will scale with h . However, as h approaches d , the geometry of the obstacle will depend on d as well as h and consequently the proposed scaling law will break down.

Similar tests were carried out to determine the influence of h on the pressure distribution in the reattachment region. In Ref. 6, it was suggested that the pressure variation in this region was caused by the fact that h was

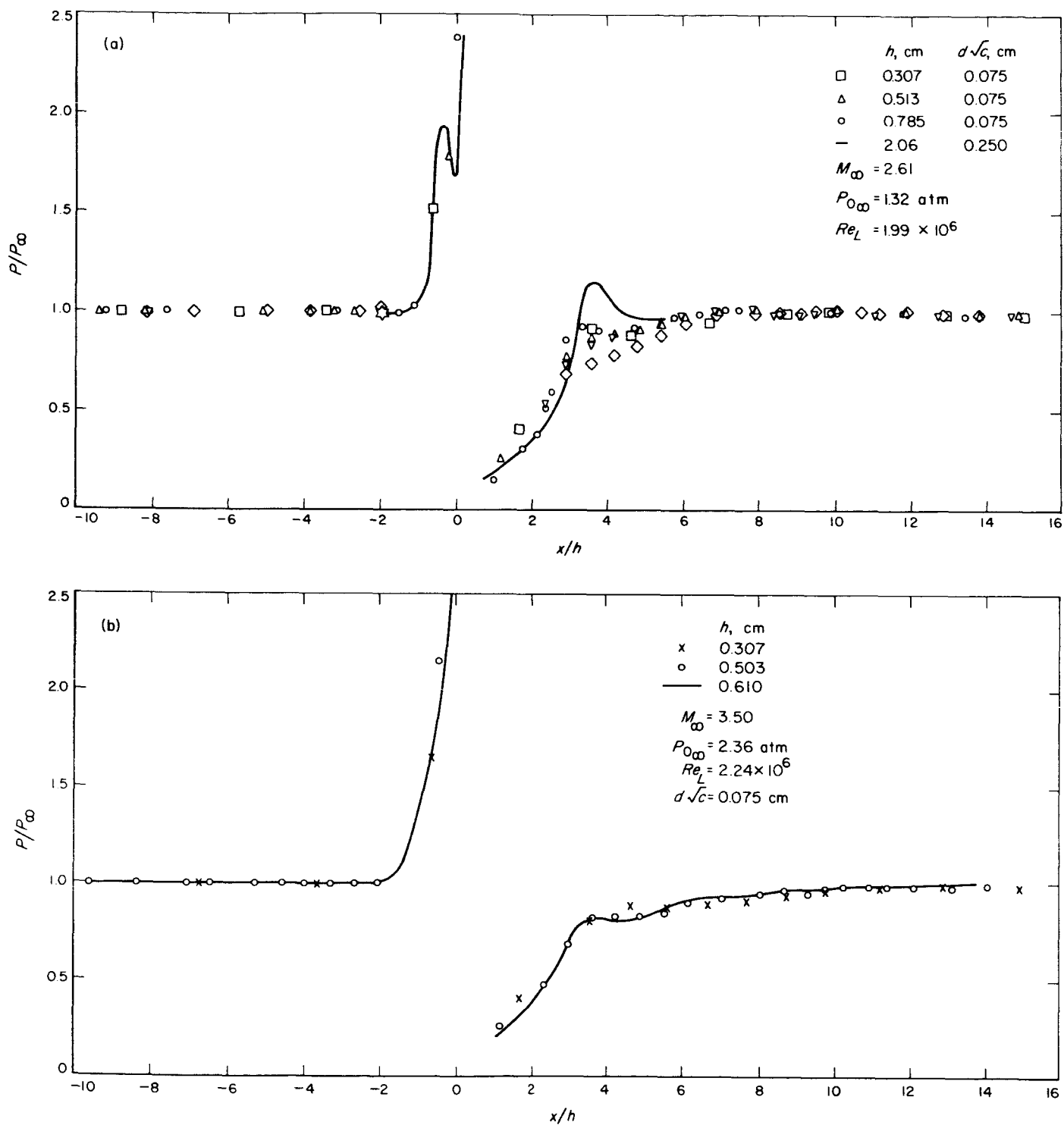


Fig. 37. Flat-plate static-pressure measurements in the plane $(y/h) = 0$ with nitrogen as injectant, turbulent boundary layer; data for small-diameter injector

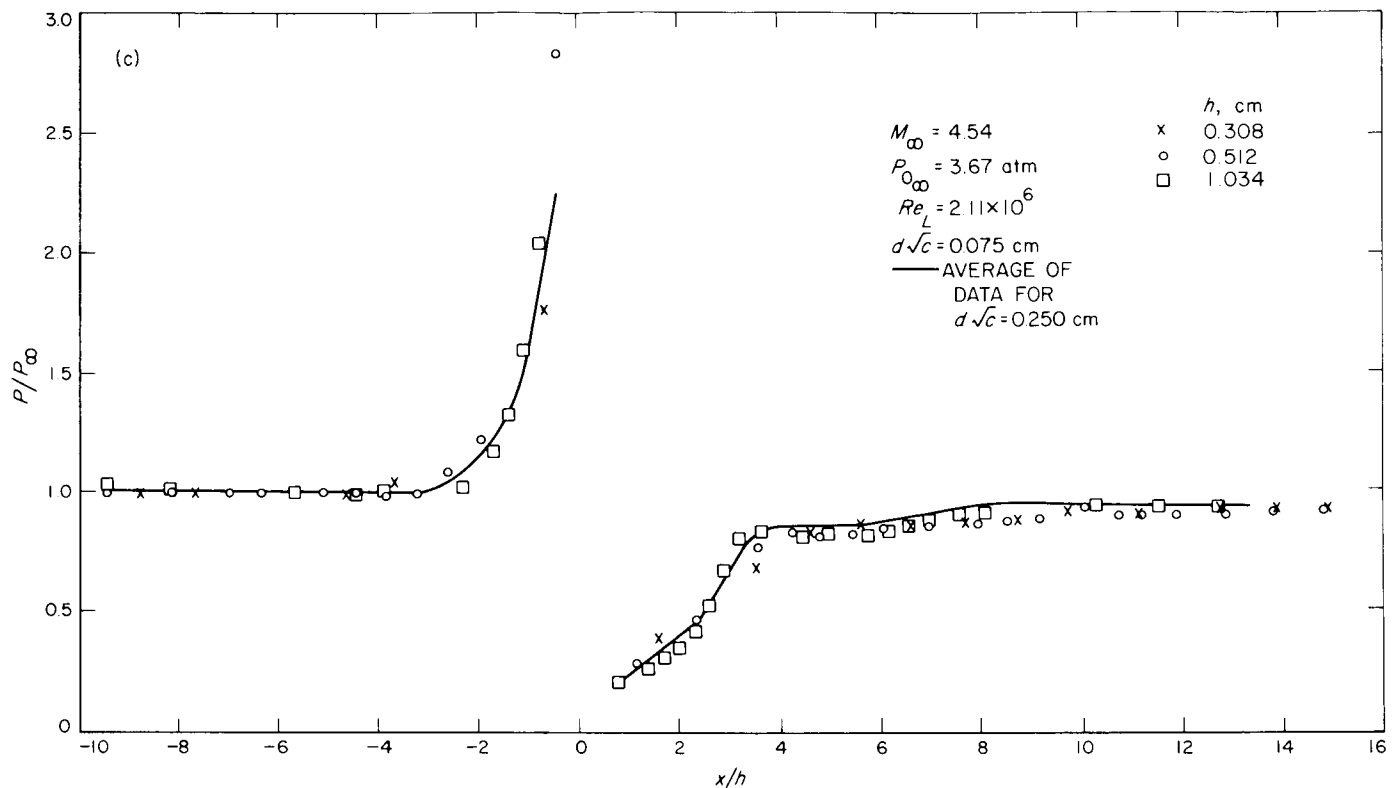


Fig. 37 (Cont'd)

changed by changing the injectant total pressure P_{0j} . Therefore, the pressure ratio through which the injectant expands increases with increasing h . This increase in pressure ratio was believed to be accompanied by an increase in the average Mach number of the injectant flow just upstream of reattachment. Since the attachment of the jet to the wall was believed to be associated with a turning of the injectant flow through a compression-wave system, the resulting pressure overshoot on the wall would increase as the injection pressure and the local upstream Mach number is increased. In the present work, the validity of this argument was tested by comparing pressure distributions of flows in which the total pressure of the injectant was held fixed and for which h was changed by changing the diameter of the injector. The results (see Fig. 38) clearly show that the pressure overshoot changes rapidly with hole size, and therefore that the hypothesis suggested in Ref. 6 is incorrect.

A second hypothesis is that the boundary-layer thickness is the important parameter. This was checked by comparing pressure distributions for tests in which the injection total pressure and hole size were changed so that h was held fixed. Since the boundary-layer thickness

was also held fixed, h/δ was constant. The results, presented in Fig. 39a, 39b, and 40 for Mach number 2.61 and 3.50, are in very good agreement despite the two-to-one change in injector diameter. This suggests that the ratio h/δ is important in fixing the phenomena responsible for the pressure overshoot at the reattachment point.

The only direct measure of the influence of boundary-layer thickness that can be made from the present test results is that given by comparing the JPL and Caltech data. The boundary-layer thickness for a turbulent boundary layer at $M_\infty = 2.61$ was about 0.3 cm in the JPL tests and about 0.50 cm in the Caltech tests. For none of the Caltech tests carried out with a turbulent boundary layer (see Fig. 24) was $h/\delta > 1.0$, and for none of these was a pressure overshoot observed. This is in agreement with the JPL tests, in which no overshoot was found when $h/\delta < 1$. (In subsequent tests reported in Ref. 2, values of $h/\delta \approx 2$ were obtained in the Caltech facility and the overshoot was observed.)

The data presented in Fig. 39 and 40 can be interpreted on the basis that the parameter governing the pressure rise in the reattachment region is the ratio of

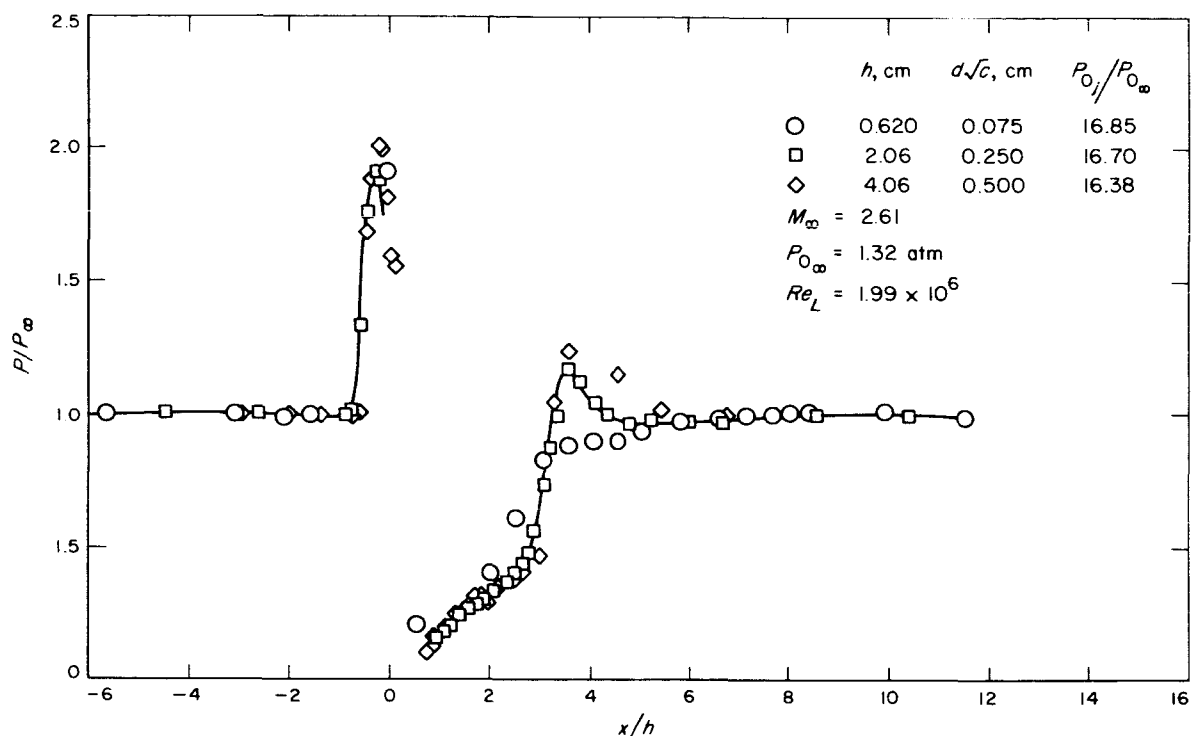


Fig. 38. Flat-plate static-pressure measurements in the plane $(y/h) = 0$ at $M_\infty = 2.61$ with nitrogen as injectant, turbulent boundary layer, showing effect of changing injector diameter

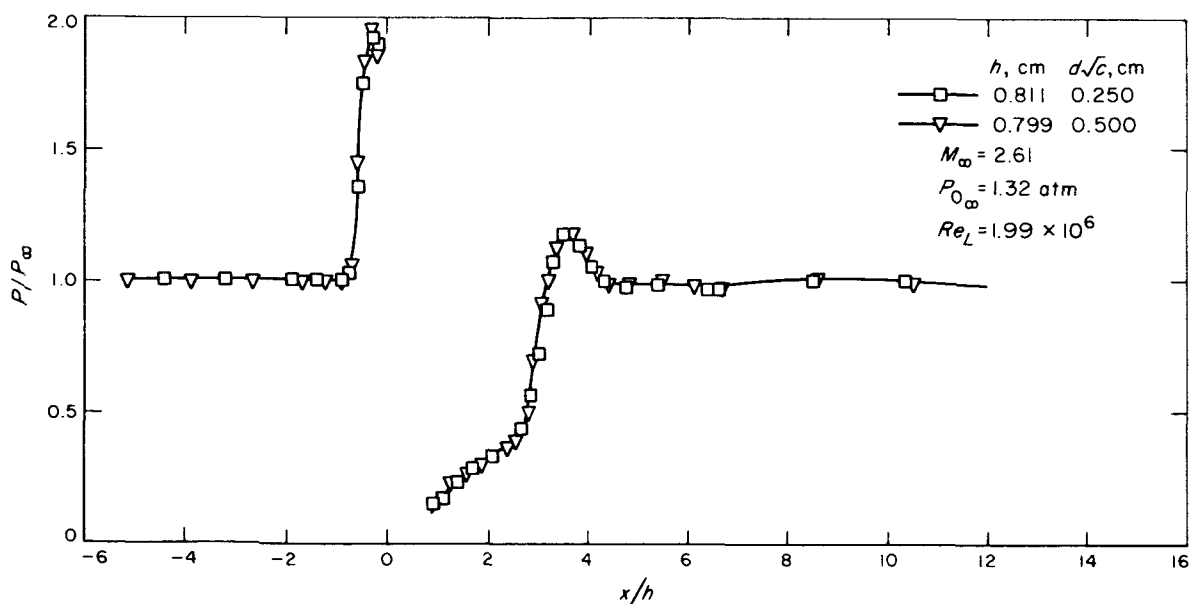


Fig. 39a. Flat-plate static-pressure measurements in the plane $(y/h) = 0$ at $M_\infty = 2.61$ with nitrogen as injectant, turbulent boundary layer, showing effect of changing injector diameter when penetration distance is held fixed

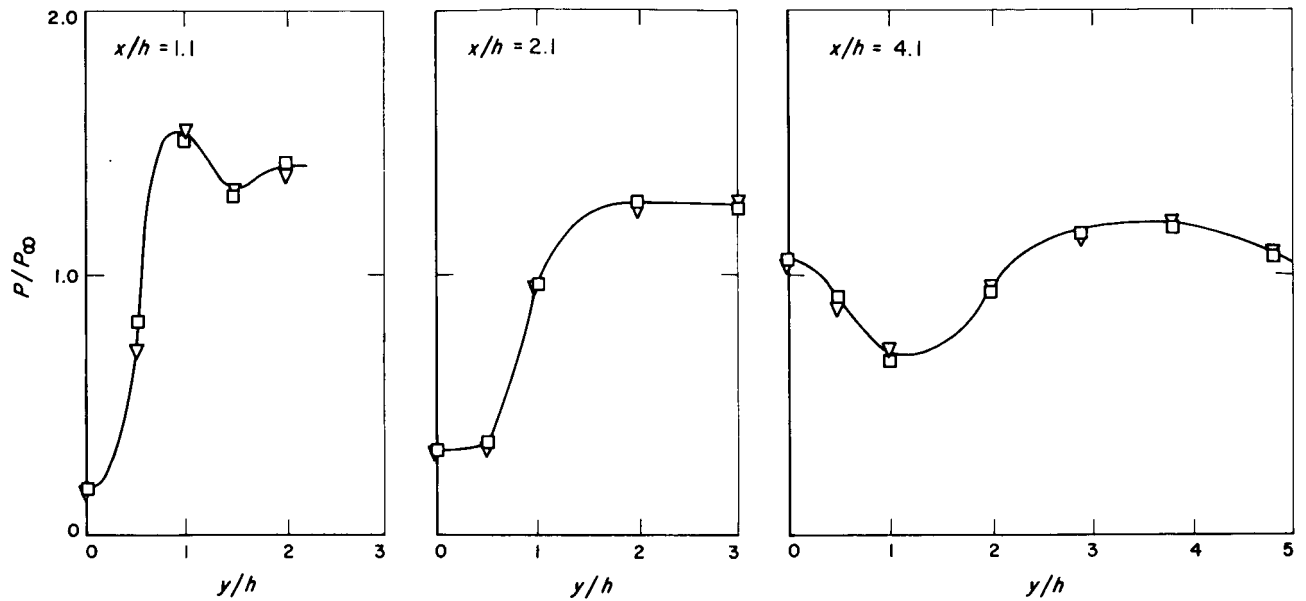


Fig. 39b. Pressure measurements in off-axis planes for conditions given in Fig. 39a

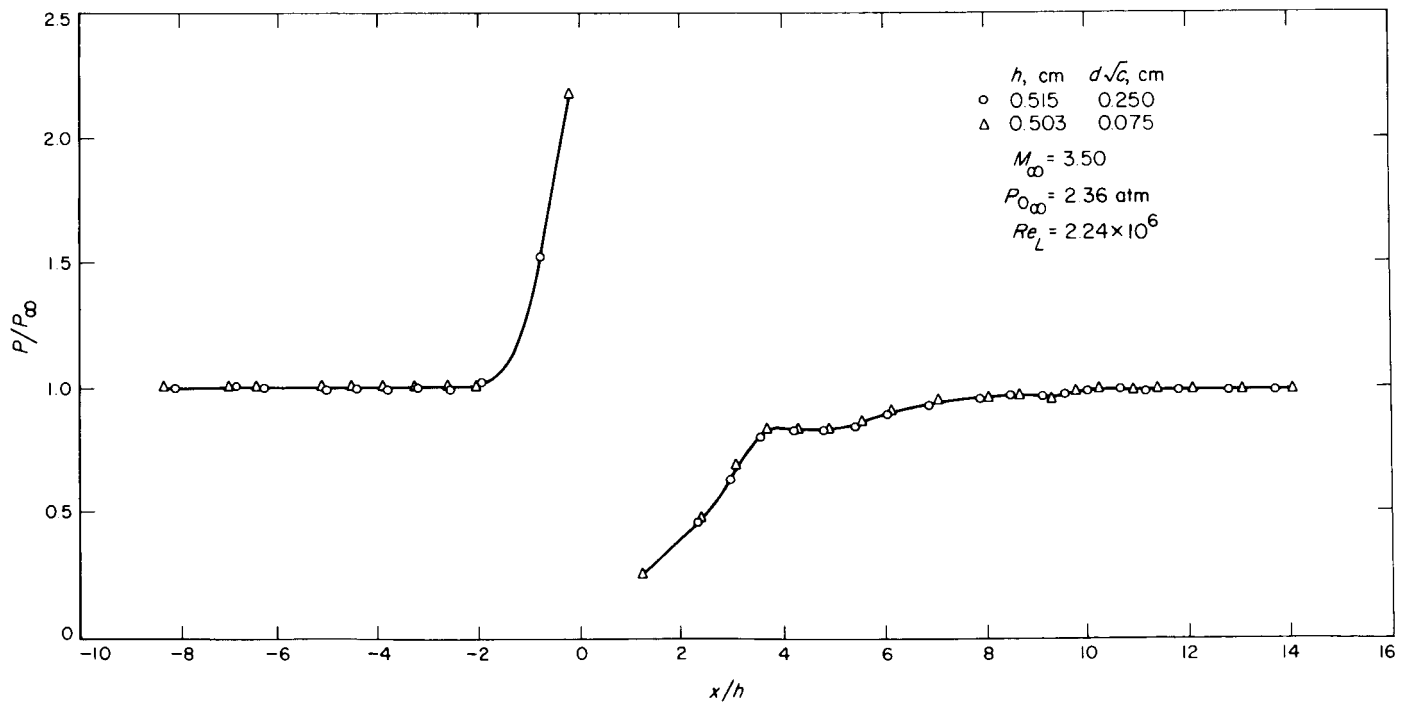


Fig. 40. Flat-plate static-pressure measurements in the plane $(y/h) = 0$ at $M_\infty = 3.50$ with nitrogen as injectant, turbulent boundary layer, showing effect of changing injector diameter when penetration distance is held fixed

penetration height to boundary-layer thickness. A more direct test is required to conclusively prove this hypothesis.

F. Helium Injection

The pressure measurements discussed up to this point were carried out with nitrogen as the injectant. The influence of changing molecular weight and specific heat ratio γ were investigated by making tests with helium as injectant.

Comparison of pressure distributions at Mach numbers 2.61 and 3.50 are given in Fig. 41, 42a, 42b, and 43 for turbulent and a laminar boundary layers. At both conditions, the normalized distributions upstream of the injector for nitrogen and helium injection are identical. However, there are systematic differences in the downstream distributions and these become more important as the Mach number increases. The off-axis cuts at Mach number 3.50 show that these differences are most important along the x -axis and in the reattachment region. This fact is also evident when pressure maps for nitrogen

(Fig. 22a, 34, 35) and those for helium (Fig. 44, 45, and 46) are compared. In particular, compare Fig. 22a and 44, for which the free-stream conditions and the values of h are nearly the same.

These data indicate that the shock system and boundary-layer separation caused by injection of helium and nitrogen are the same when equal values of h are used and, hence, show that the effective obstacles created by injection are the same. However, differences of pressure distribution in the reattachment region indicate that this zone is strongly affected by the composition of the injectant. In general, higher pressures were obtained in this region with helium than with nitrogen.

G. Scaling of Other Published Data

Several papers appearing in the literature have presented pressure distributions on flat plates with secondary injection (Ref. 5, 9, 10, 11), which are similar to the results of experiments described in this Report. Data from the paper by Cubbison, Anderson, and Ward

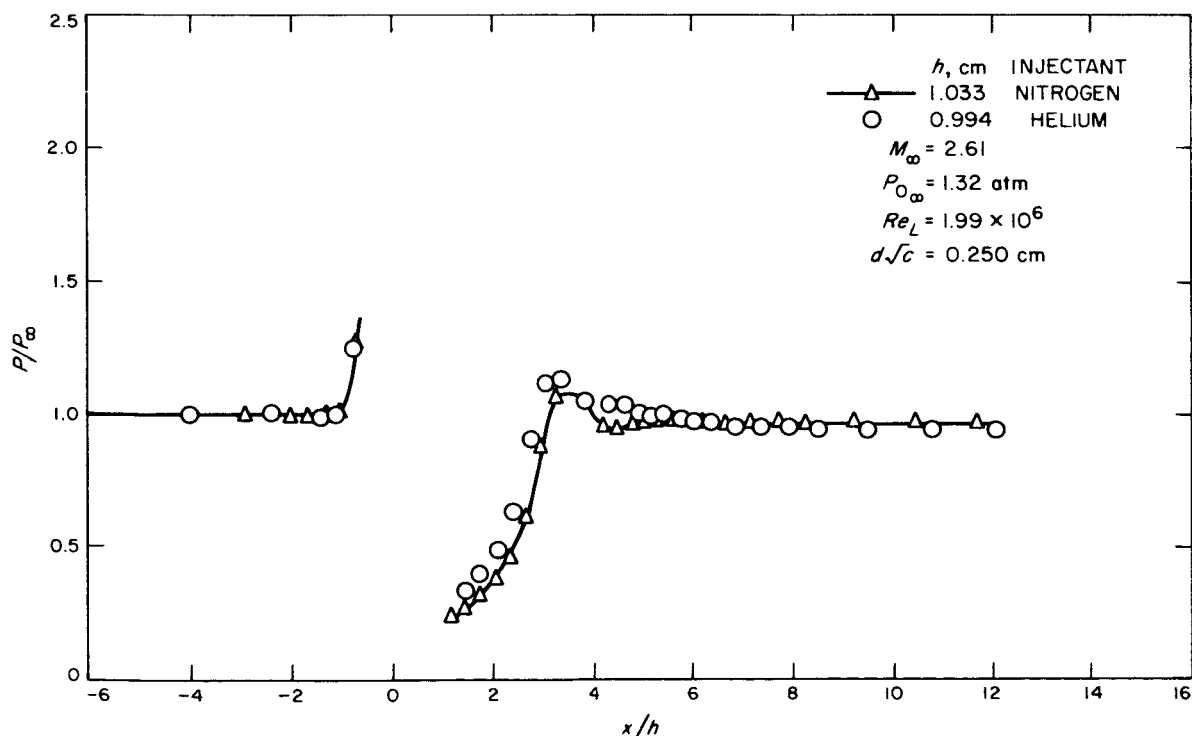


Fig. 41. Effect of injectant properties on flat-plate static-pressure measurements in the plane (y/h) = 0 at $M_\infty = 2.61$ with nitrogen and helium as injectant; turbulent boundary layer

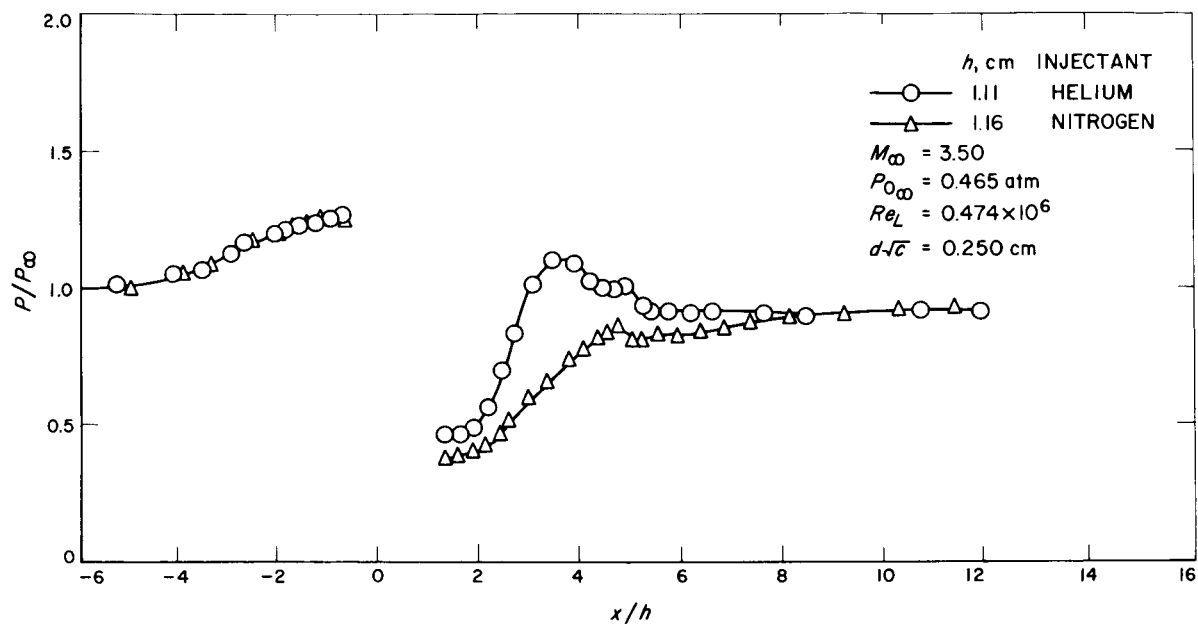


Fig. 42a. Effect of injectant properties on flat-plate static-pressure measurements in the plane (y/h) = 0 at $M_\infty = 3.50$ with nitrogen and helium as injectant; turbulent boundary layer

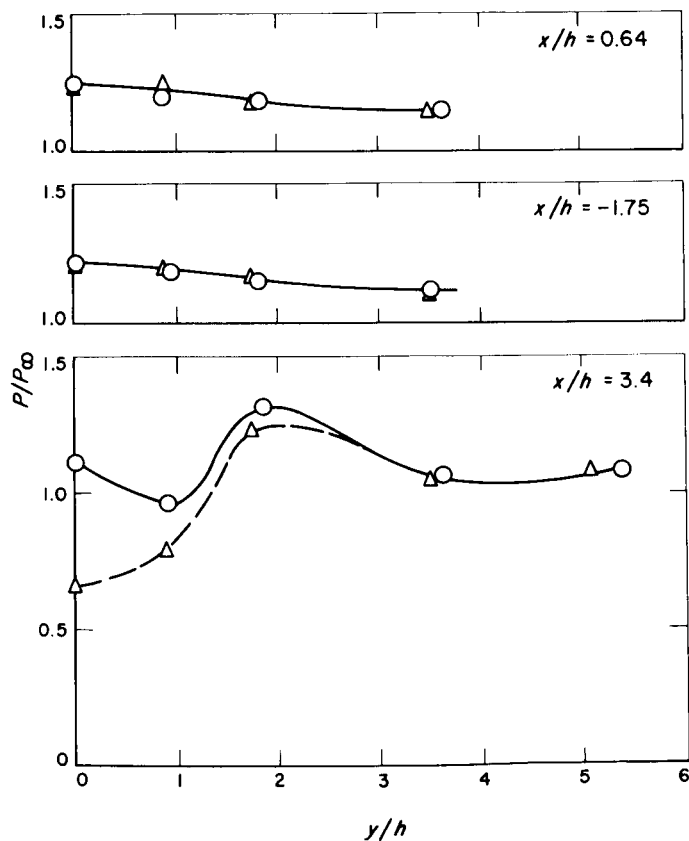


Fig. 42b. Pressure measurements in off-axis planes for conditions given in Fig. 42a

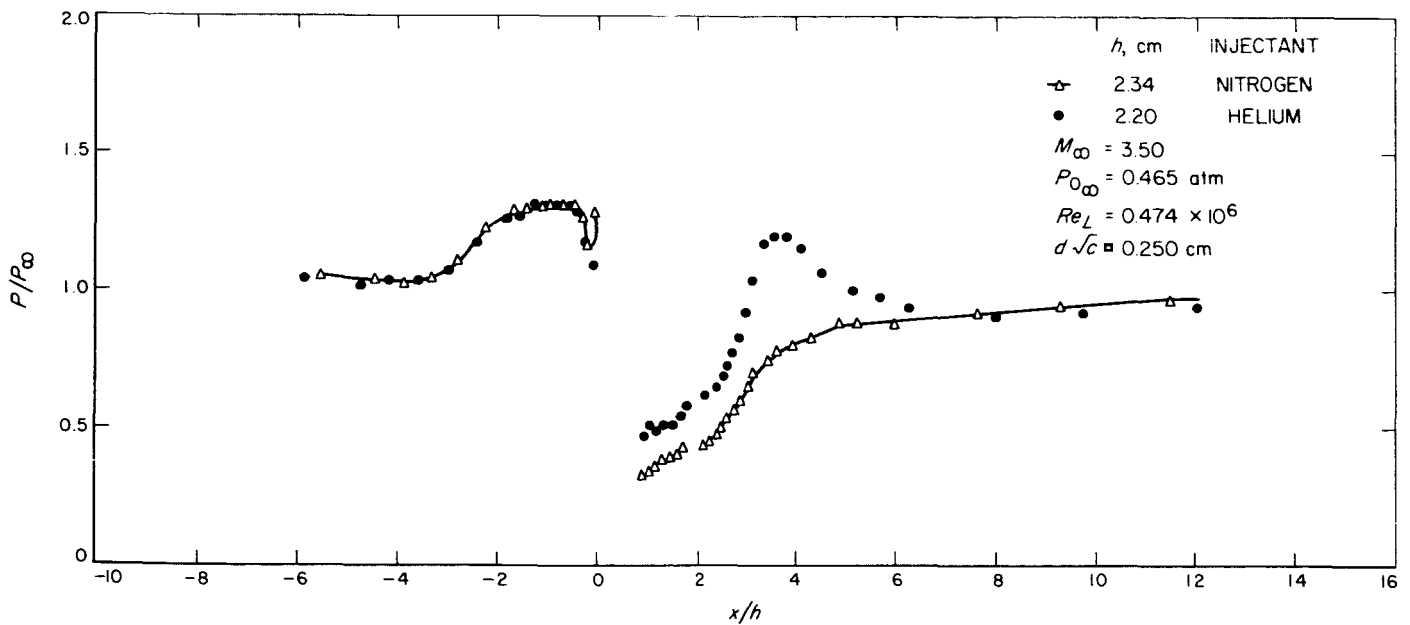


Fig. 43. Effect of injectant properties on flat-plate static-pressure measurements in the plane $(y/h) = 0$ at $M_\infty = 3.50$ with nitrogen and helium as injectant; turbulent boundary layer

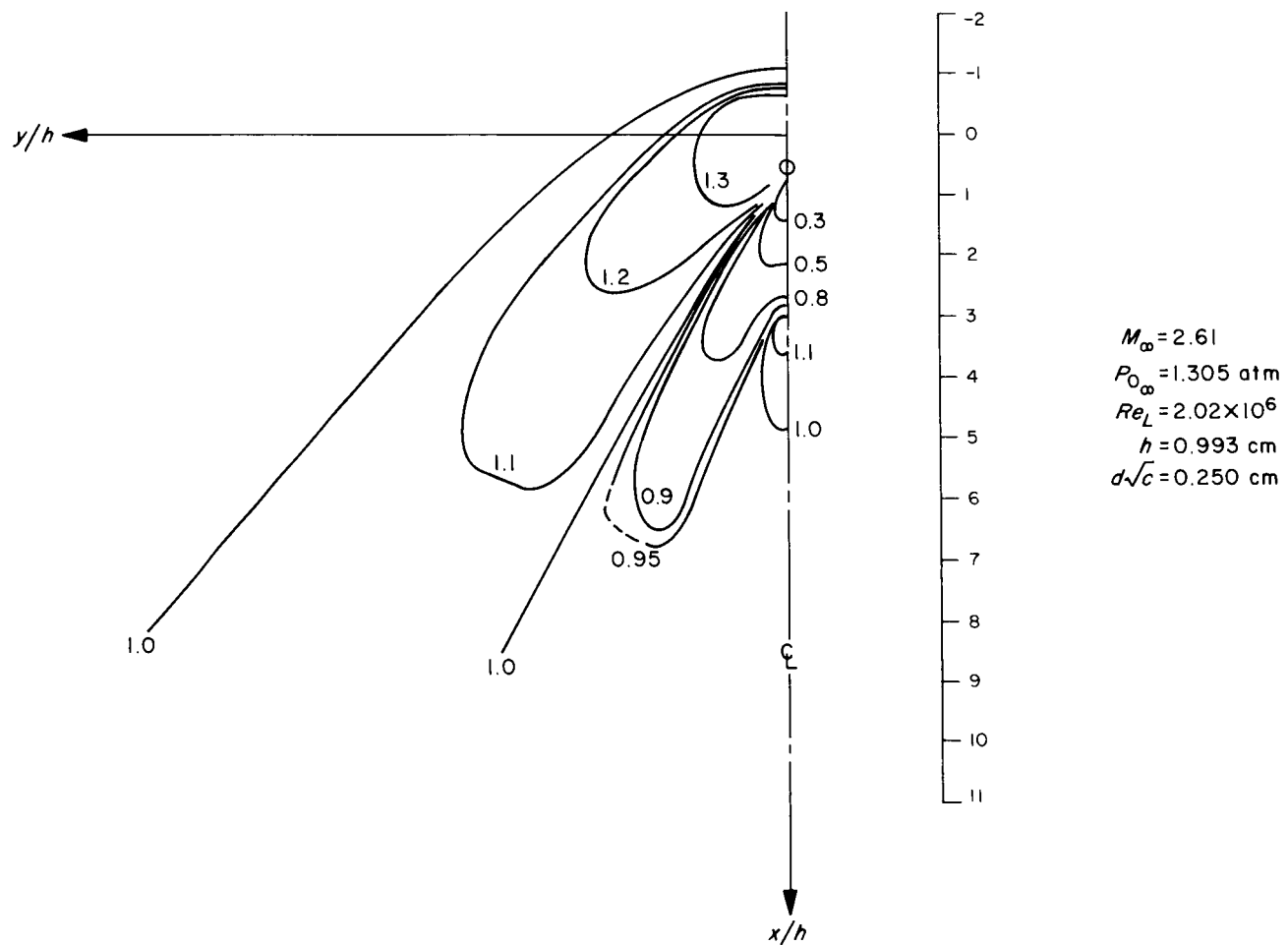


Fig. 44. Pressure map for flat-plate measurements at $M_\infty = 2.61$ with helium as injectant; turbulent boundary layer

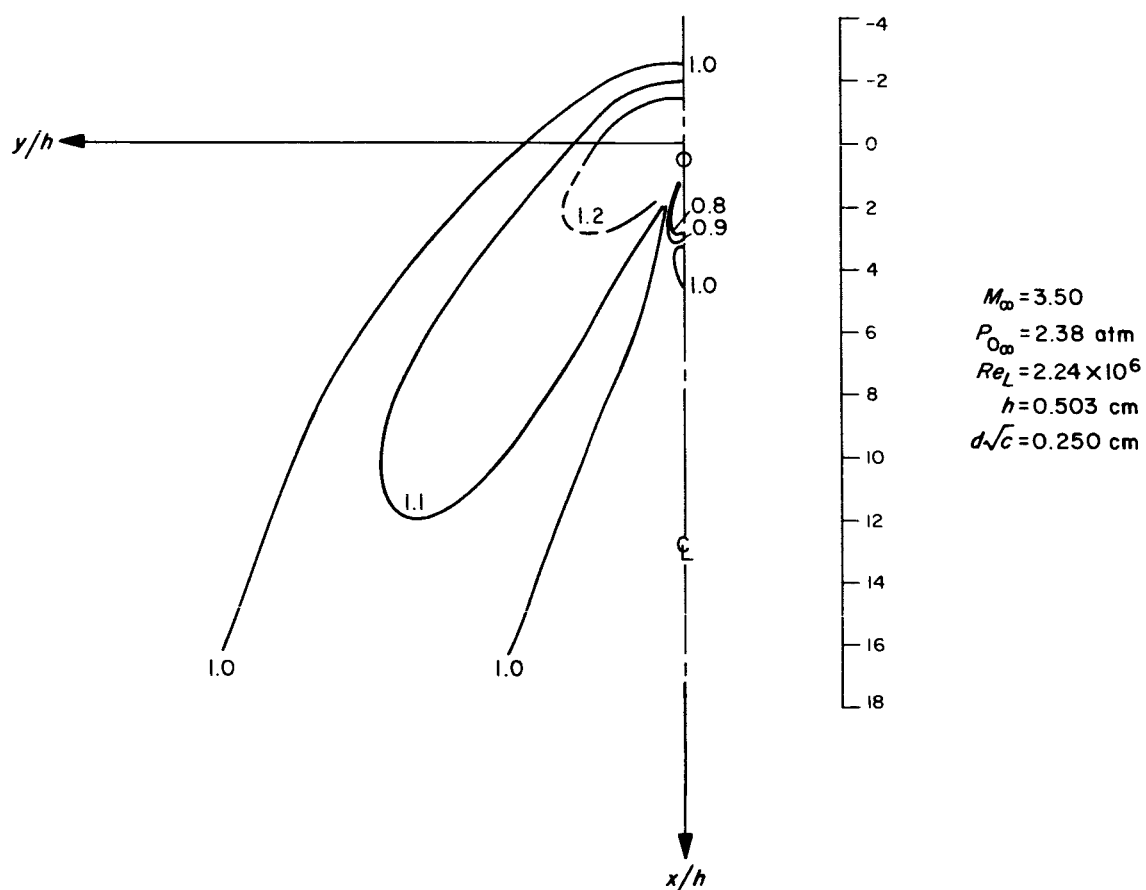


Fig. 45. Pressure map for flat-plate measurements at $M_\infty = 3.50$ with helium as injectant; turbulent boundary layer

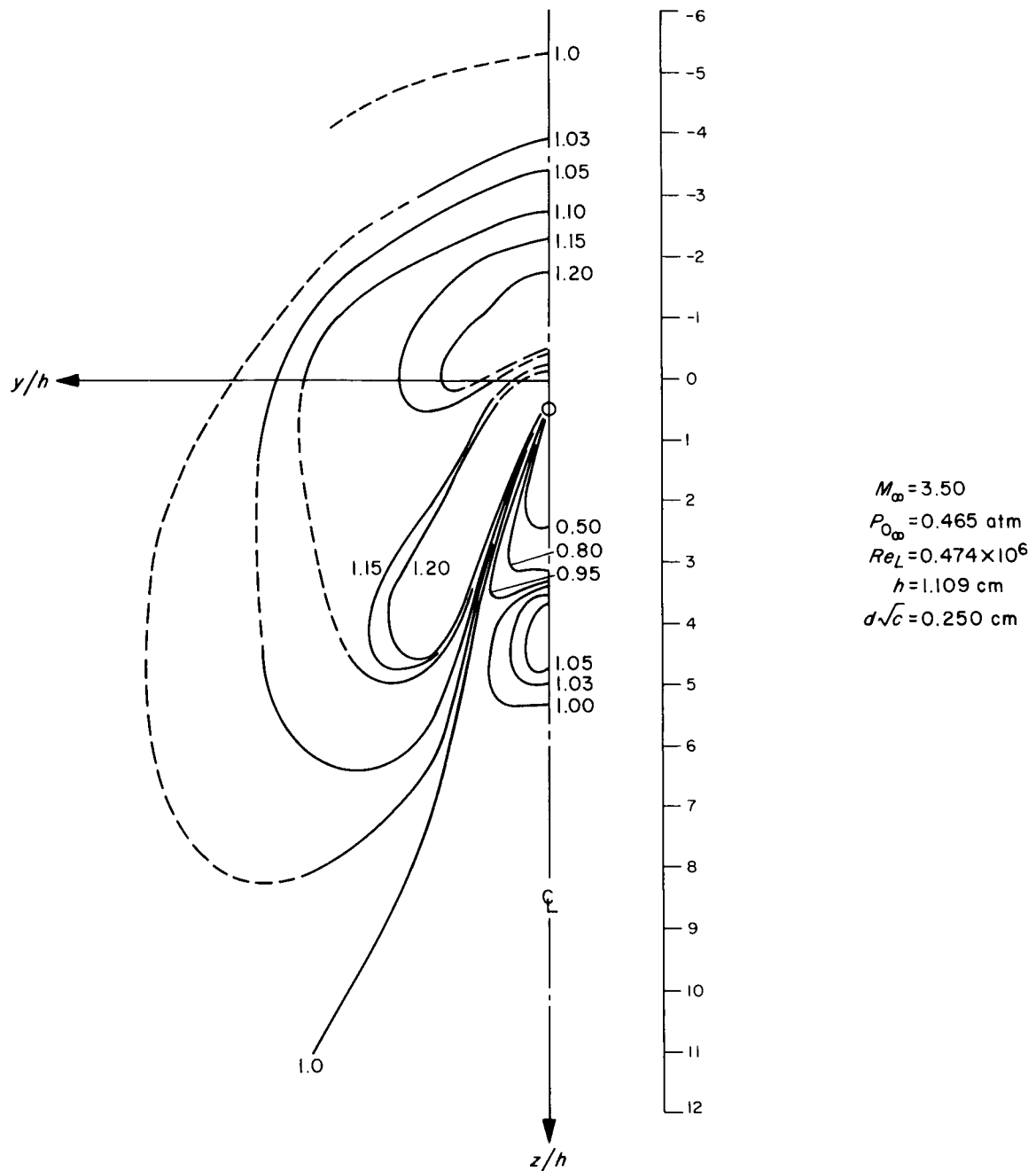


Fig. 46. Pressure map for flat-plate measurements at $M_\infty = 3.50$ with helium as injectant; laminar boundary layer

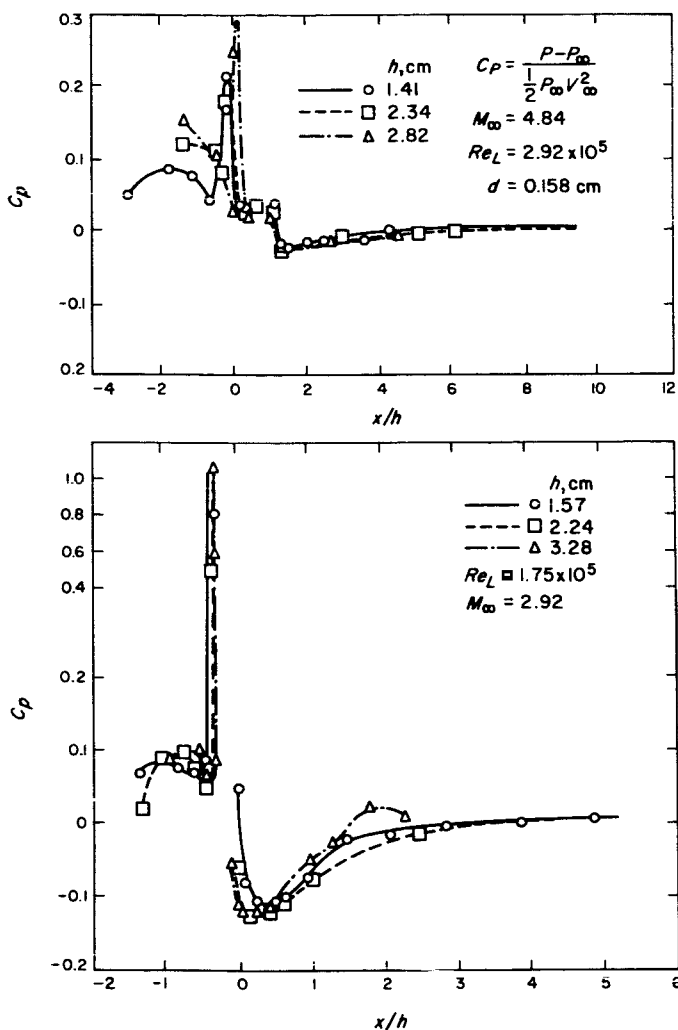


Fig. 47. Correlation of pressure data from Ref. 9

(Ref. 9) were considered to be the most directly comparable to those presented here. Figure 47 presents six pressure distributions in the plane $y = 0$ for two Mach numbers; the data are plotted in the manner of Fig. 23, except that the original pressure-coefficient notation was retained. The correlation of the data is seen to be quite good, except in the separation region upstream of the injector at free-stream Mach number 4.84. It should be

noted that for the two largest values of h , at $M_\infty = 4.84$, the boundary layer was separated up to the leading edge of the plate, thus precluding any similarity in that region.

H. Two-Hole Injectors

Exploratory experiments were made to investigate the pressure distribution when nitrogen was injected through two holes separated by a few diameters. The holes were aligned so that their common centerline was perpendicular to the flow direction. Shadowgraphs of the interaction produced by injection with this geometry are shown in Fig. 48a through 48c for a turbulent boundary layer and Mach number 2.61. The interaction region upstream of the bow shock is greatly enlarged for this case due to the interference effects between the two jets.

A pressure map for a typical example is shown in Fig. 49. There is a large region of interference between the injection ports, which greatly enhances the areas of the high-pressure region upstream of the injectors and the areas of the low-pressure region downstream of the injectors.

Comparison of pressure distributions along the x -axis, whose origin was taken upstream of the center of one of the holes, is shown in Fig. 50 and 51. In both figures, data are presented for geometries in which the distance between hole centers, Y_0 , normalized by h is held constant. The correlation is good even when different values of h are used.

The data presented in Fig. 48-51 were obtained for Mach number 2.61 and a turbulent boundary layer. Similar tests were made at Mach number 4.54, and the resulting pressure maps are shown in Fig. 52, 53, and 54.

In conclusion, these brief tests with the two-hole injector indicate that the scaling laws set up for the single-hole geometry are satisfactory for scaling the interaction produced by injection through two holes and, hence, probably for an array of holes.

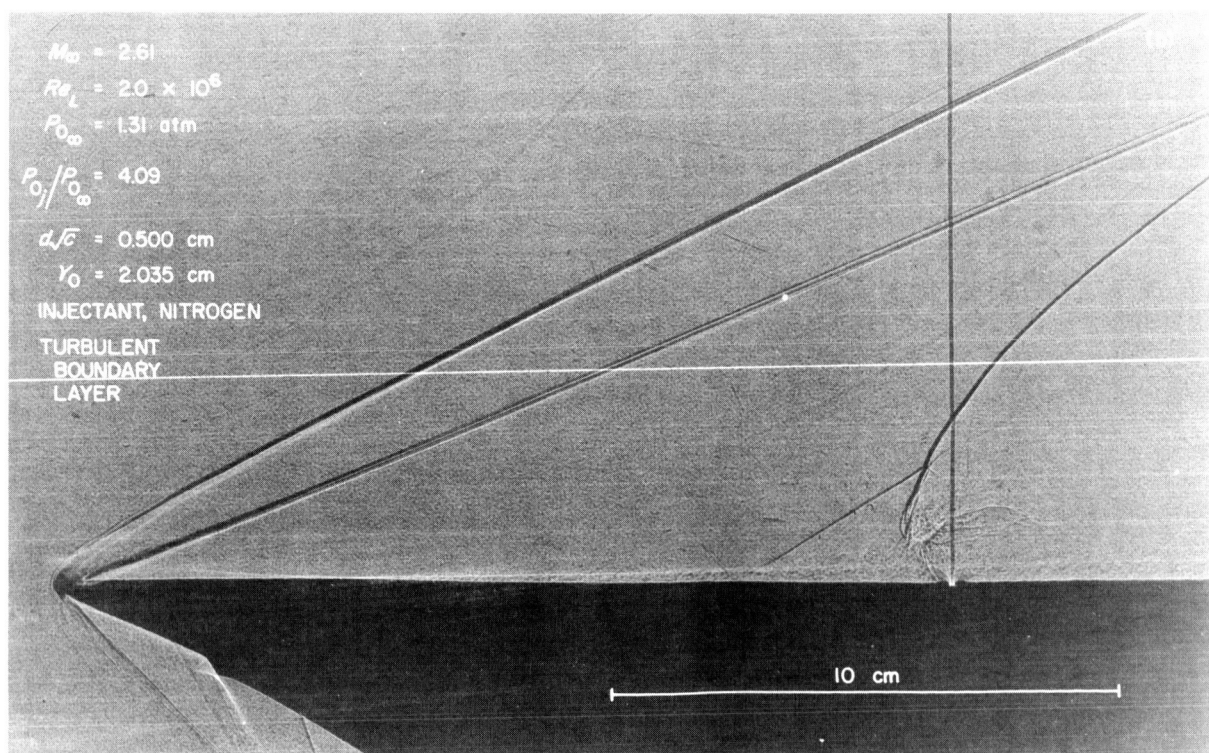
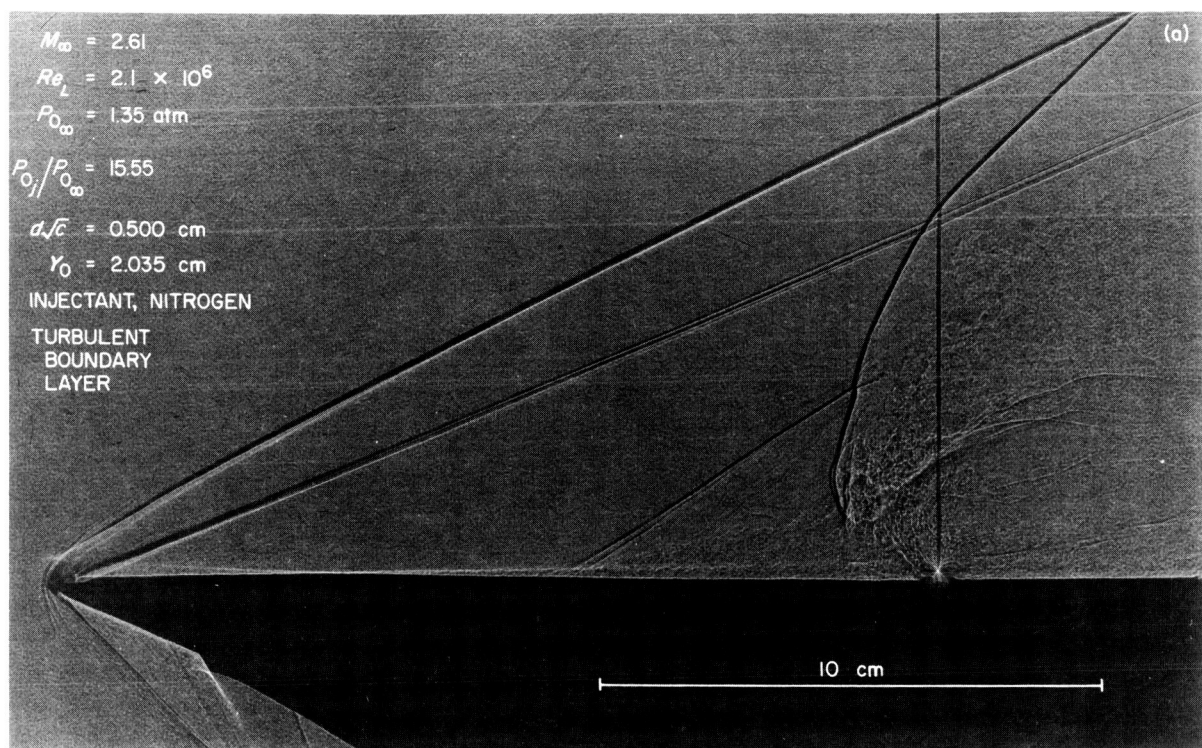


Fig. 48. Shadowgraph photographs; flat-plate data; double-hole injectors

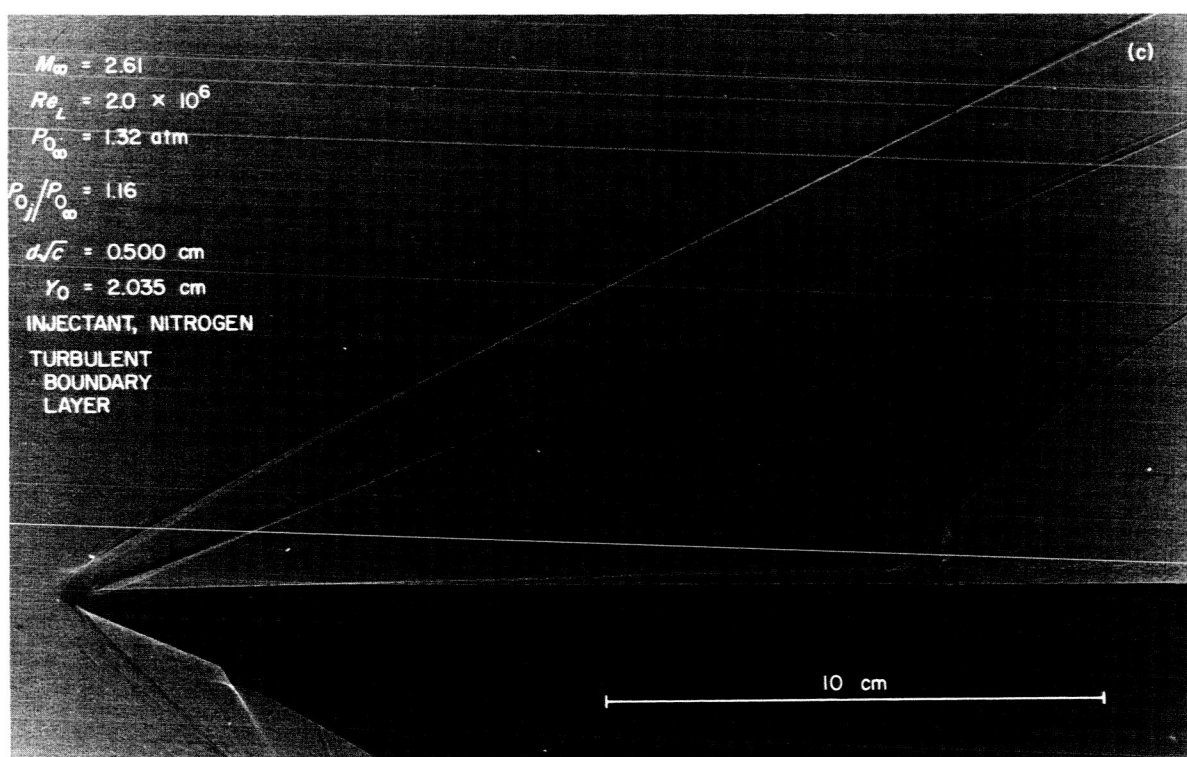


Fig. 48. (Cont'd)

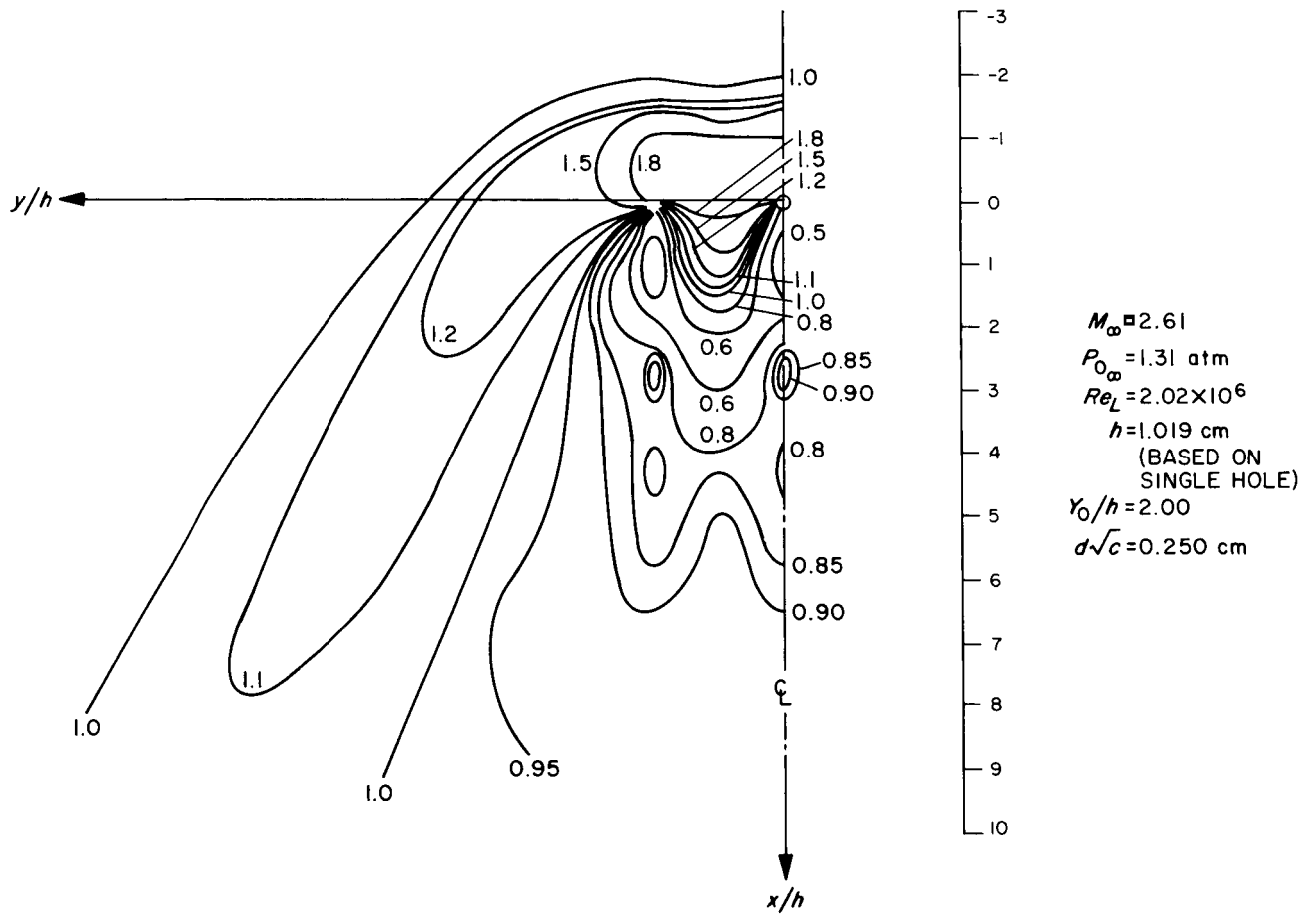


Fig. 49. Pressure map for flat-plate measurements at $M_\infty = 2.61$ with nitrogen as injectant; turbulent boundary layer; injection through two holes

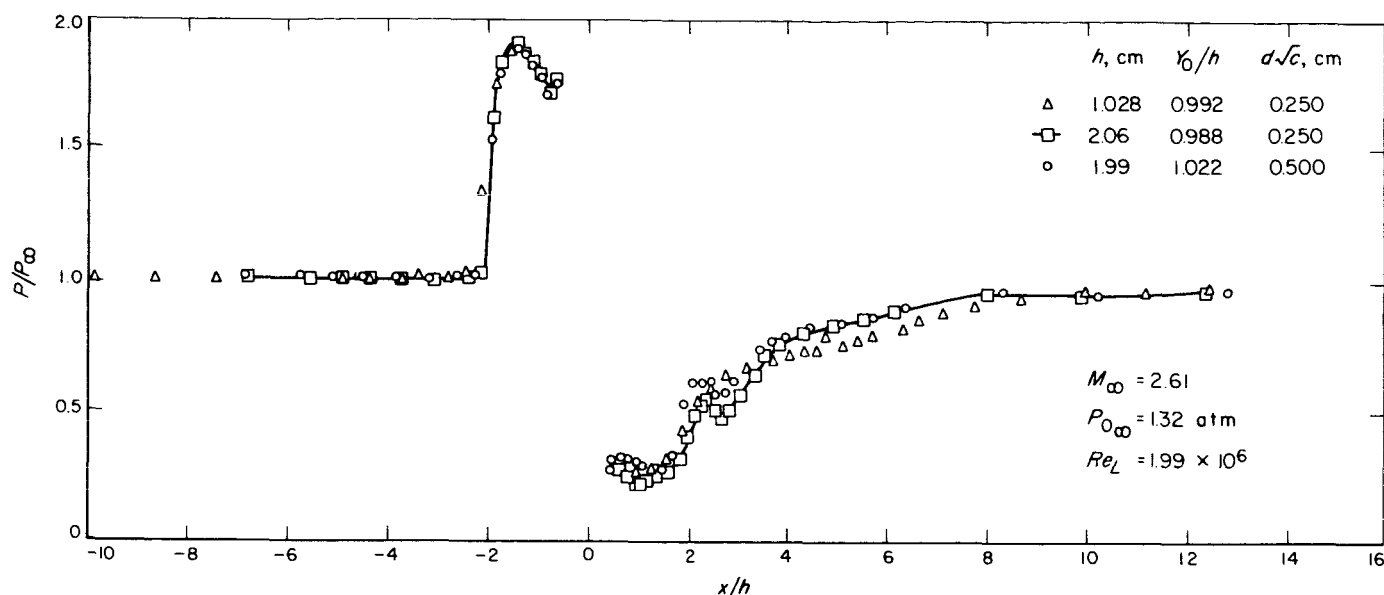


Fig. 50. Flat-plate static-pressure measurements in the plane $(y/h) = 0$ at $M_\infty = 2.61$ with nitrogen as injectant; turbulent boundary layer; injection through two holes, with the x -axis aligned with the centerline of one hole

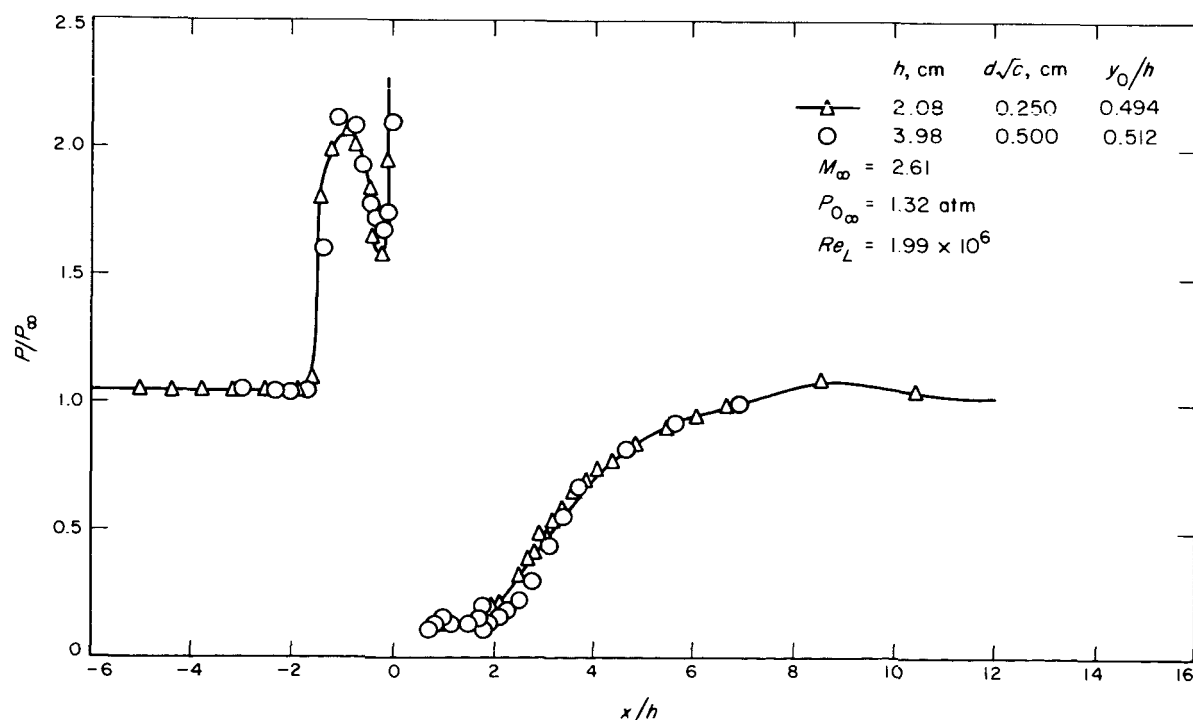


Fig. 51. Flat-plate static-pressure measurements in the plane $(y/h) = 0$ at $M_\infty = 2.61$ with nitrogen as injectant; turbulent boundary layer; injection through two holes, with the x -axis aligned with the centerline of one hole

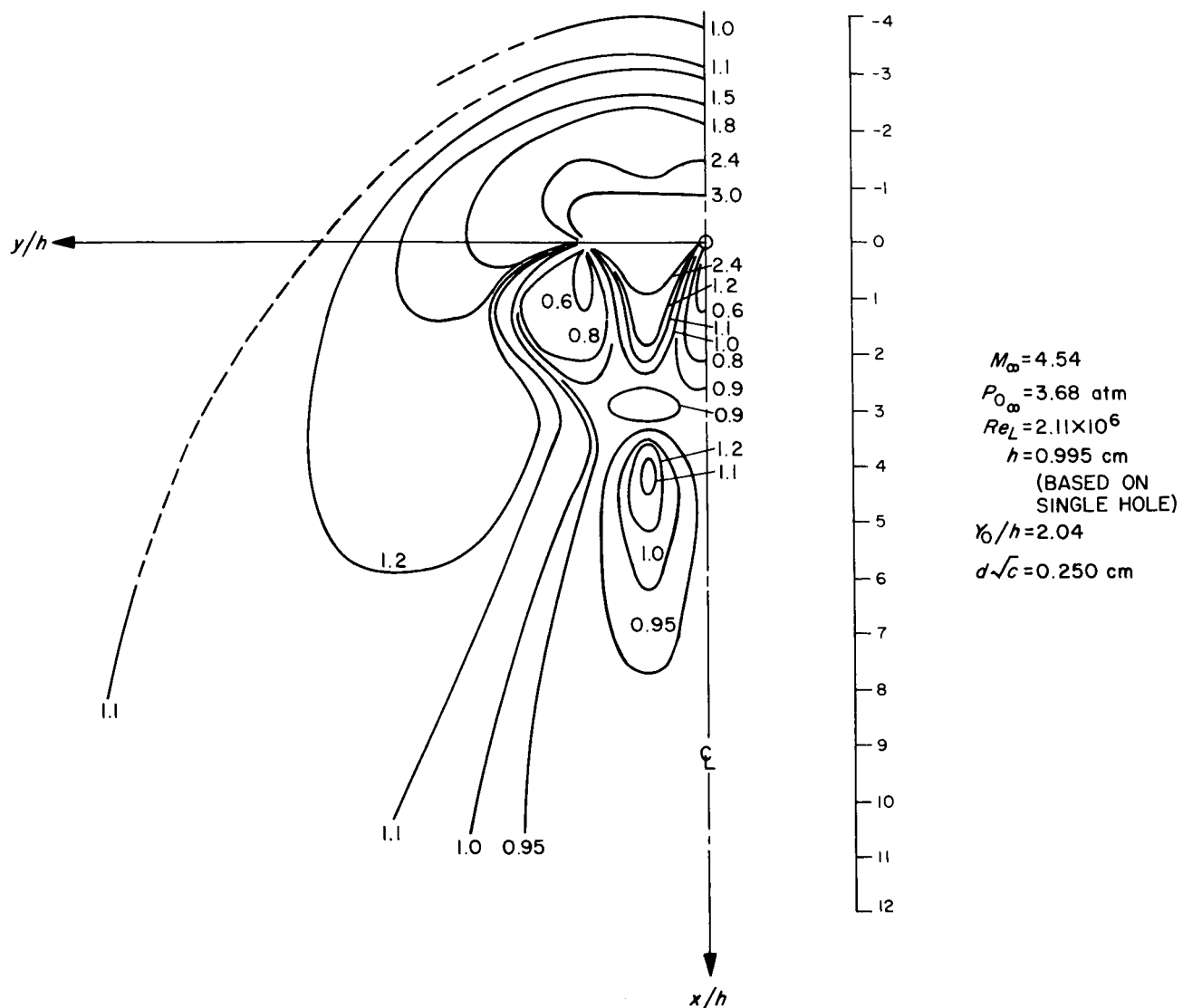


Fig. 52. Pressure map for flat-plate measurements at $M_\infty = 4.54$ with nitrogen as injectant; injection through two holes; turbulent boundary layer

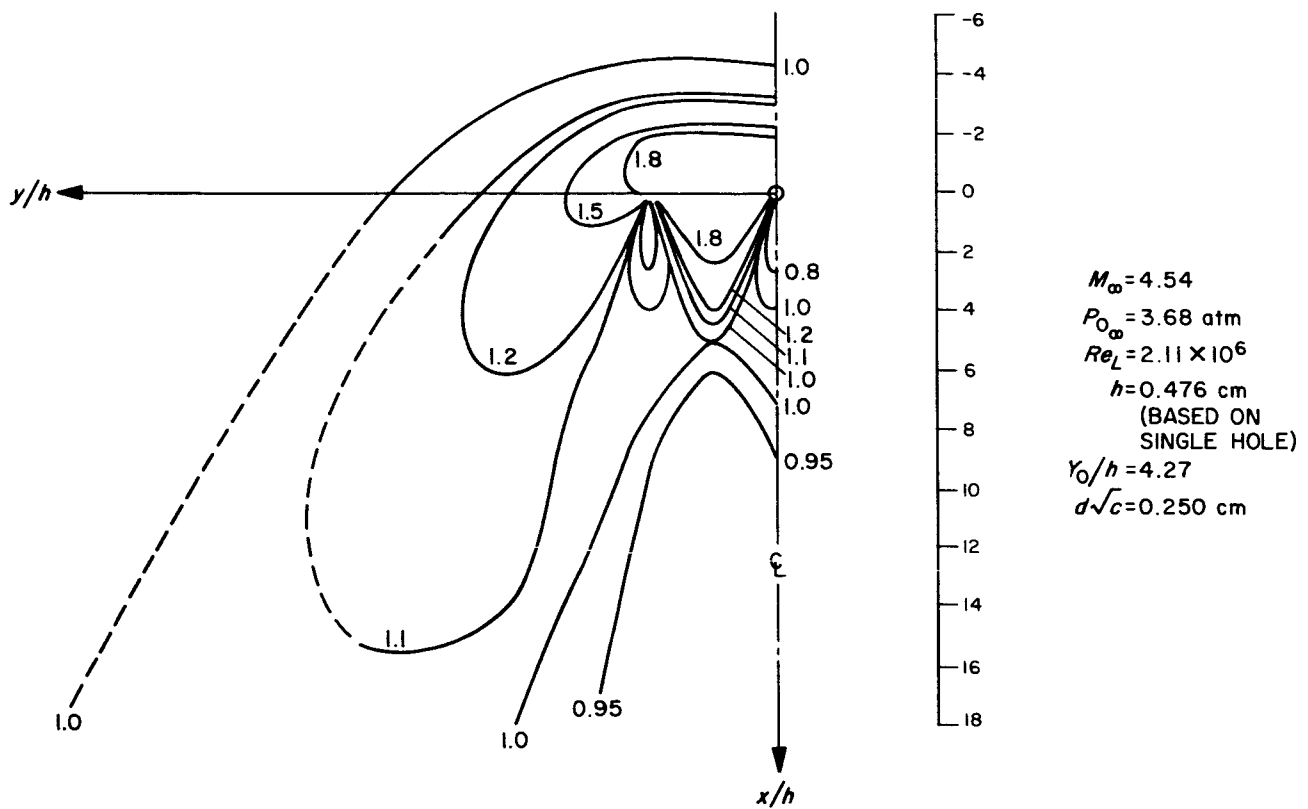


Fig. 53. Pressure map for flat-plate measurements at $M_\infty = 4.54$ with nitrogen as injectant; injection through two holes; turbulent boundary layer

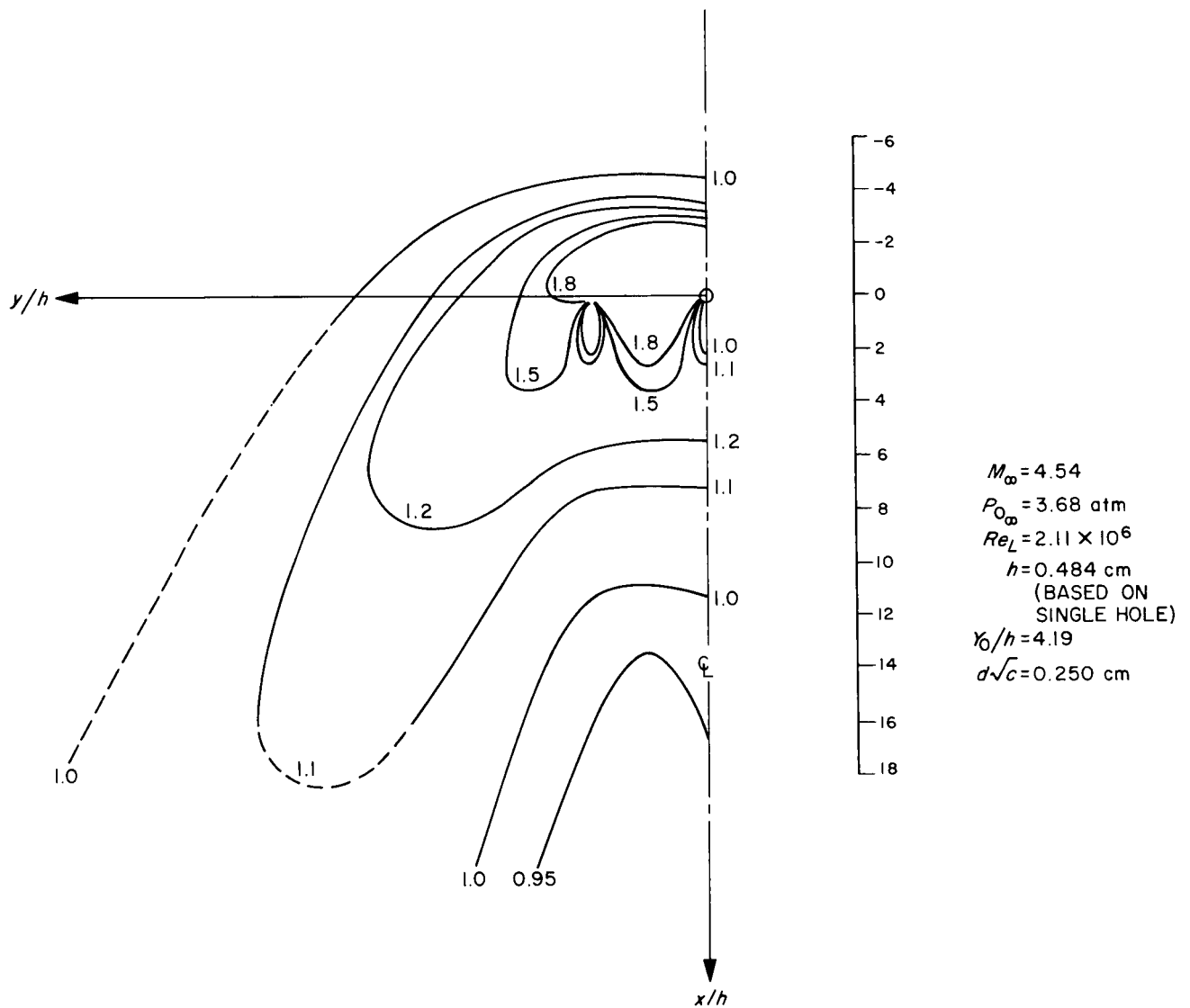


Fig. 54. Pressure map for flat-plate measurements at $M_\infty = 4.54$ with helium as injectant; injection through two holes; turbulent boundary layer

VI. DISCUSSION AND CONCLUSIONS

Quantitatively, the results of the shock-shape, concentration, and pressure measurements indicate that the scaling parameter h is satisfactory for the range of variables investigated, with the previously mentioned restriction that it be about equal to or greater than the separated boundary-layer thickness and larger than the injector-hole diameter. The correlation of the shock and concentration data was excellent, but it appears that the restrictions to the applicability of the scale parameter are more severe for the static-pressure distribution on the wall. Lack of similarity in the pressure data was observed in the laminar boundary-layer separation region and in the reattachment region downstream of the injector. In these regions, it is apparent that a simple one-parameter scale transformation cannot give a detailed correlation of the pressure data and that the ratios of scale height to boundary-layer thickness and to injector diameter can be important parameters when these ratios are equal to or less than one.

A. Review of Flow Models

A number of models have been suggested by other authors that lead to a calculation of a scale height for secondary injection (for example, see Ref. 12-15). Unfortunately, most of these models are for two-dimensional flow and are not directly applicable. However, it is still possible to compare their approach to the one used in this Report.

The assumption used in one type of model was that the penetration height is fixed by the area required to pass the mass flow of injectant after it expands isentropically to the local ambient pressure (Ref. 12). In the model proposed in this Report, this assumption leads to the result that the penetration height depends only on the ambient static pressure and injectant specific heat ratio, and is independent of the momentum of the free stream. These conclusions are not in agreement with the experimental results.

A second type of model (e.g., Ref. 13) is based on the assumption that the separated boundary layer is tangent to the top of the injectant stream, and that side force is only generated upstream of the injector port. The experimental work presented in this Report indicates that such a model is valid only when the scale height is less than the boundary-layer thickness. Furthermore, analysis of the results of Newton and Spaid (Ref. 16) shows that with gaseous injection, the major portion of

the side force is applied downstream of the injector port. They found that there was still a small positive contribution to the side force for $(x/h) > 12$. Although this work was carried out in a conical rocket nozzle, the results should apply at least qualitatively to the present discussion.

Additional information is furnished by analysis of the results of Walker, et al. (Ref. 17), who worked with a conical nozzle that had injector ports of various diameters located close to the nozzle exit. The values of specific impulse of side injection I_s , from Ref. 17, are given in Fig. 55 as a function of the ratio of distance between injector port and nozzle exit to values of the scale parameter calculated from Eq. (6). In these experiments, the ratio of the distance between the injector and nozzle exit to h varied from about 2.9 to 8.5, and the corresponding specific impulse for secondary injection increased by a factor of about 1.4. These results can also be interpreted as showing the effect of systematically increasing the wall area on which the pressure disturbances act from an area corresponding to $(x/h) = 2.9$ to $(x/h) = 8.5$. For this configuration the contribution to side force is small when $(x/h) > 7$. This result agrees with the analysis of the data of Newton and Spaid (Ref. 16), discussed in the preceding paragraph, and shows that the downstream contribution to side force is very important.

A third model is that proposed by Broadwell (Ref. 14), in which the blast-wave theory was used to obtain a pressure field on a flat plate. The scale of this pressure field was determined by calculating a value for drag produced by injection and equating this to the energy added to the free stream per unit length. This drag is therefore completely analogous to the change in the x -component of momentum of the jet in the present model [Eq. (3), (4), and (5)]. A value of drag, then, corresponds to a scale height, so that these two approaches can be compared. In Ref. 14 the drag, or energy per unit length, is calculated by assuming first, that the injected material reaches the velocity of the undisturbed free stream, and second, that the effect of adding mass can be taken into account by adding heat to a part of the free-stream flow sufficient to produce the same volume change that would be produced by mass addition. The result of this calculation is as follows:

$$D = m_i V_\infty \left[1 + \frac{2 + (\gamma_\infty - 1) M_\infty^2}{2(\gamma_\infty - 1) M_\infty^2} \frac{\rho_{\infty}}{\rho_i} \frac{T_{o_i}}{T_{o_\infty}} \right] \quad (10)$$

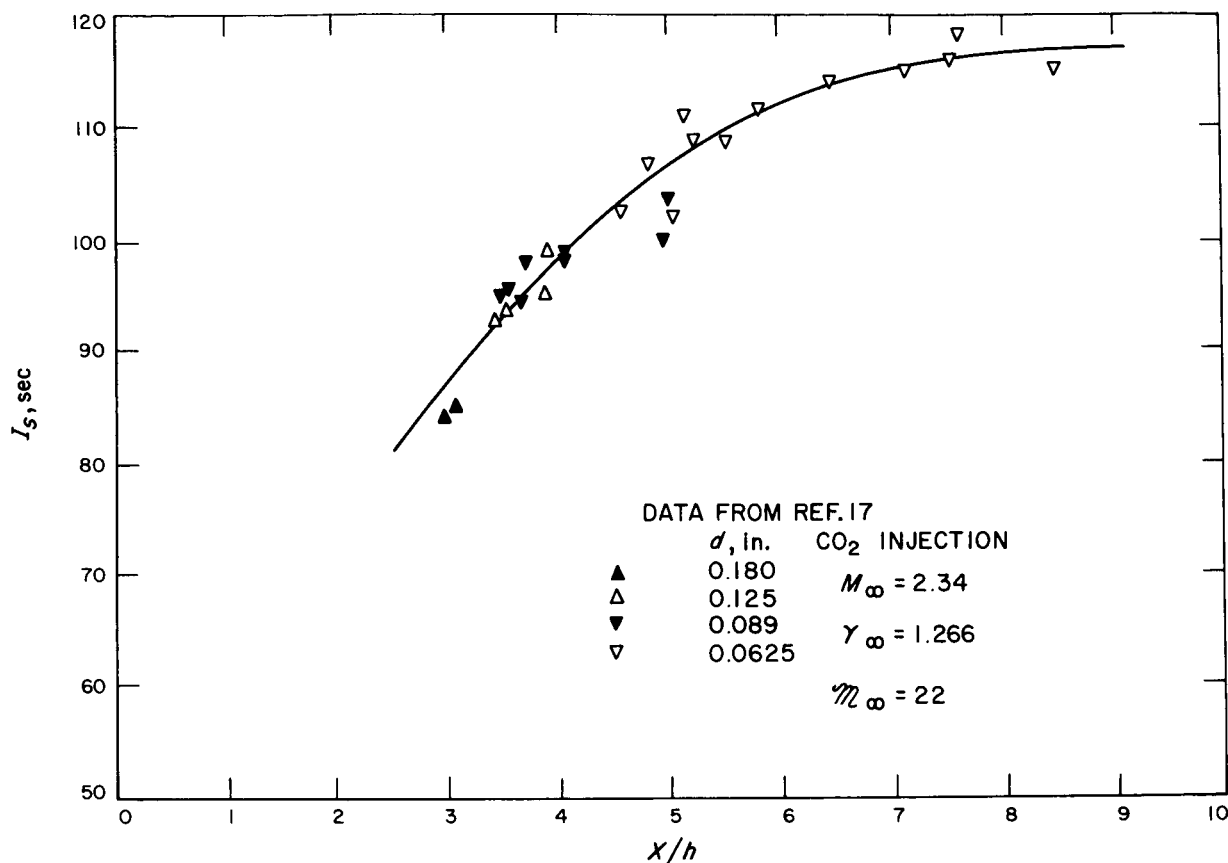


Fig. 55. Variation of side specific impulse with normalized distance from injector to nozzle exit

In order to compare the effect of these assumptions with the present model, an equation for scale height similar to Eq. (6) was derived by substituting Eq. (10) for Eq. (5) in the present derivation. The resulting equation, analogous to Eq. (6), gave very nearly the same Mach number dependence as Eq. (6), but showed a strong dependence upon the molecular weight of the injectant at a constant value of ratio of free-stream pressure to injection pressure. This dependence was not observed. These results indicate that the scale of the flow field is probably determined by an isentropic expansion of the jet in the immediate vicinity of the injector, rather than by the acceleration and mixing process between the jet and the free-stream material, which occurs farther downstream. These results and conclusions are also in accord with the fact that the drag of a slender, blunt-nosed body at high Mach numbers is determined almost entirely by the characteristic nose-bluntness dimension (Ref. 18).

B. Review of the Flow-Field Characteristics

The concentration and pressure data have now made it possible to add some details to the qualitative description

of the flow field presented in Section IV. It has been shown that the jet mixes very rapidly as it leaves the injector, and much more slowly for (x/h) greater than about 4. The jet is approximately parallel to the wall at $(x/h) \approx 3$.

A pair of vortices appear to be shed from the jet near the injector; these accelerate the mixing process and result in a region of low concentration of injectant material in a region immediately downstream of the jet near the wall. The flow is separated just downstream of the injector and appears to reattach to the wall in the region $3 \lesssim (x/h) \lesssim 4$. This reattachment may be accompanied by a compression-wave system, increasing in strength with the ratio of jet to free-stream stagnation pressure and with decreasing free-stream Mach number.

The character of the boundary-layer separation for injection into a turbulent boundary layer is quite different from the separation of a laminar boundary layer. The pressure rise due to turbulent separation extends only slightly upstream of the bow shock, but the laminar boundary layer separates far upstream. In neither case,

however, does the height of the separated boundary layer approach the height of the jet, if the jet height is much greater than the undisturbed boundary-layer thickness. This result is quite different from the results obtained in boundary-layer separation studies with a two-dimensional step (Ref. 19). Part of this difference seems to be the result of the inherent difference between two- and three-dimensional obstructions; the boundary layer can simply go around the three-dimensional object, but the flow must all go over the top of the two-dimensional one. In addition, the jet shape near the wall, discussed at the end of Section IV, tends to provide clearance for the boundary layer.

C. Applications of the Scaling Law to Scaling of Forces

If the scaling law, as developed earlier in Eq. (6), can be taken as a good approximation, then it is easy to predict the variation of the side force generated on an infinite flat surface by the variation of the jet parameters. For many purposes, it is desirable to know the change in force produced on the wall by secondary injection.

The side-force contribution from the pressure field resulting from secondary injection from an infinite flat plate can be expressed as

$$\Delta F = \int_{x=-\infty}^{\infty} \int_{y=-\infty}^{\infty} (P - P_{\infty}) dx dy \quad (11)$$

Dividing through $P_{\infty} h^2$ we have

$$\frac{\Delta F}{P_{\infty} h^2} = \int_{(x/h)=-\infty}^{\infty} \int_{(y/h)=-\infty}^{\infty} \frac{P - P_{\infty}}{P_{\infty}} \frac{dx}{h} \frac{dy}{h} \equiv \Phi \quad (12)$$

The integral in Eq. (12) is evaluated in the normalized coordinates, and therefore will depend only upon the free-stream Mach number and specific heat ratio. That is,

$$\Phi = \Phi \{M_{\infty}, \gamma_{\infty}\}$$

The total side force due to injection, F_s , is the sum of the interaction force ΔF and the thrust of the injectant F_j .

The thrust of a sonic jet is given by

$$F_j = P_{0j} A_j C_I \{M = 1\} \quad (13)$$

where

$$C_I \{M = 1\} = \left(\frac{2^{\gamma_j}}{\gamma_j + 1} \right)^{1/(\gamma_j - 1)} - \frac{P_{\infty}}{P_{0j}} \quad (14)$$

It is useful to compare the total force due to injection with the thrust that would be produced by the jet alone if it were expanded isentropically in a nozzle to the free-stream static pressure. This quantity will be denoted $F_{j_{mar}}$, and is given as follows:

$$F_{j_{mar}} = P_{0j} A_j C_{\gamma_j} \times \left\{ \frac{2}{\gamma_j - 1} \left(\frac{2}{\gamma_j + 1} \right)^{(\gamma_j + 1)/(\gamma_j - 1)} \left[1 - \left(\frac{P_{\infty}}{P_{0j}} \right)^{(\gamma_j - 1)/\gamma_j} \right] \right\}^{1/2} \quad (15)$$

Combining Eq. (6), (12), (13), (14), and (15), we have

$$\frac{F_s}{F_{j_{mar}}} = \frac{8\Phi}{\pi M_{\infty}^2 \gamma_{\infty} C_p^*} + \frac{\left(\frac{2^{\gamma_j}}{\gamma_j + 1} \right)^{1/(\gamma_j - 1)} - \frac{P_{\infty}}{P_{0j}}}{\gamma_j \left\{ \frac{2}{\gamma_j - 1} \left(\frac{2}{\gamma_j + 1} \right)^{(\gamma_j + 1)/(\gamma_j - 1)} \left[1 - \left(\frac{P_{\infty}}{P_{0j}} \right)^{(\gamma_j - 1)/\gamma_j} \right] \right\}^{1/2}} \quad (16)$$

and

$$\frac{\Delta F}{F_{j_{mar}}} = \frac{8\Phi}{\pi M_{\infty}^2 \gamma_{\infty} C_p^*} \quad (17)$$

The second term in Eq. (16) is the ratio $F_j/F_{j_{mar}}$, the ratio of the thrust of a sonic jet to the thrust of a jet with optimum expansion.

The usual form for presentation of rocket-motor tests has been to give the ratio of side force to axial force as a

function of the ratio of secondary to primary mass flow rates. That is,

$$F_s/F_p = f \left(\frac{m_j}{m_p} \right)$$

Results from Eq. (16) can be compared with rocket-motor data by using the expression for $F_{j_{mar}}$ written in terms of m_j , as follows:

$$F_{j_{mar}} = m_j \left\{ \frac{2\gamma_j R_j T_{0j}}{\gamma_j - 1} \left[1 - \left(\frac{P_{\infty}}{P_{0j}} \right)^{(\gamma_j - 1)/\gamma_j} \right] \right\}^{1/2} \quad (18)$$

Equations (16) and (18) can be used to correlate side-force measurements if the dimensionless pressure integral Φ is known.

Even when Φ is not known, correlation can be made if $F_s/F_{j_{max}}$ is held constant, keeping in mind that the first term in Eq. (16) depends only upon free-stream parameters. This condition implies that valid comparisons can be made when any of the following parameters are changed: injectant molecular weight and total temperature, injector diameter, and primary-stream molecular weight and total temperature. In addition, the dependence of Eq. (16) and (18) upon P_{oj} is very weak, particularly if $P_{oj} \gg P_\infty$. Hence, a change in the ratio P_{oj}/P_∞ will only introduce a slight error in scaling.

Subject to these restrictions, it is evident that

$$F_s \propto m_j (R_j T_{oj})^{1/2}$$

In addition, if changes in axial thrust of the primary flow caused by nonoptimum expansion and by secondary injection are neglected, then

$$F_p \propto m_p (R_p T_{op})^{1/2}$$

and therefore

$$\frac{F_s}{F_p} \propto \frac{m_j}{m_p} \left[\frac{R_j T_{oj}}{R_p T_{op}} \right]^{1/2} = \frac{m_j}{m_p} \left[\frac{T_{oj}/M_j}{T_{op}/M_p} \right]^{1/2} \quad (19)$$

This result indicates that the thrust ratio depends directly on the mass flow rate and on the square root of the ratio of injectant total temperature to molecular weight. The ratio is independent of injector diameter.

The discussion given in the earlier Sections of this Report indicates that a number of restrictions must be placed on the scaling procedure. Clearly, the procedure is strictly applicable only if the wall on which the pressure disturbances exist is of sufficient extent that the pressure at its boundaries has returned to the free-stream static pressure. In practice, this means that the boundaries must be at least $10h$ away from the injector.

In addition to this geometric limitation, it will be useful to summarize again the limitations on the scaling procedure itself. First, it is necessary that the scale height be at least as large as the separated boundary-layer thickness and as large as the injector diameter.

Second, if the boundary layer is turbulent, scaling appears to be excellent except in the reattachment region.

The data discussed in this Report suggest that if scaling of a nozzle is carried out in such a manner as to keep the ratio of penetration height to boundary-layer thickness constant, then the reattachment phenomena will also be similar and no scaling errors will be introduced.

Third, if the boundary layer is laminar, upstream-separation phenomena are more important, and scaling may be less satisfactory. In this case, there is some indication that pressure changes compensate each other (Ref. 15); however, no information on such compensation can be deduced from the present work.

Some direct comparison can be made of the scaling law developed here with experimental rocket-engine tests. Even though the flow field in a nozzle is not directly comparable to that treated here, it is felt that the general conclusions drawn from the present work are useful.

Rodriguez (Ref. 20) and many other experimenters have found that the side force is independent of the injector-port area for fixed mass flow and depends linearly on the mass flow of injectant when the primary flow parameters are held fixed. This result agrees with that obtained from Eq. (19).

Some work has been carried out in which injectants with different total temperatures and different molecular weights were used (Ref. 17, 21, 22). The correlation proposed by Lingen (Ref. 21) and later approximately verified by Chamay and Sederquist (Ref. 22) agrees exactly with Eq. (19).

Figure 56 shows data from Ref. 21 for gas injection into a rocket nozzle. The parameter T_{oj}/T_{op} was changed by a factor of more than 6 for the two cases, and the agreement is excellent, although the data are badly scattered. Figure 57 shows data from Ref. 22 for nitrogen and hydrogen injection into a rocket nozzle. The scatter here is much smaller than in Fig. 56, but the correlation is not quite so good. It can be seen that the correlation improves with increasing m_j , so that there is about 10% difference between the nitrogen and hydrogen data at the higher injection rates.

In the previously mentioned paper by Walker, et al. (Ref. 17), data are reported for injection of different gases into a rocket nozzle. The correlation of these data by the present treatment is presented in Fig. 58. Only data for sonic injection are presented. The choice of h^2 as a correlating parameter was made because it accounts for

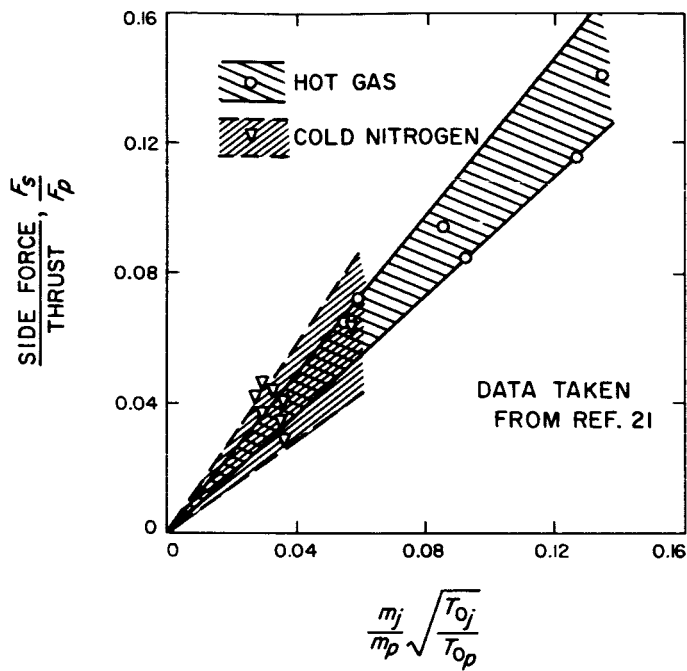


Fig. 56. Correlation of rocket-motor thrust-vector-control performance for different gases and temperatures (from Ref. 21)

variations in γ_j and P_∞/P_{0j} . It can be seen that the effect of injector diameter is accounted for quite well, but considerable systematic variation remains among data for different gases. It is interesting to note that the correlation is in error by about the same factor over the entire range of h^2 , or injection rate, in contrast to the data of Ref. 22.

The different treatment proposed by Broadwell (Ref. 23) gives a somewhat better correlation of the data of

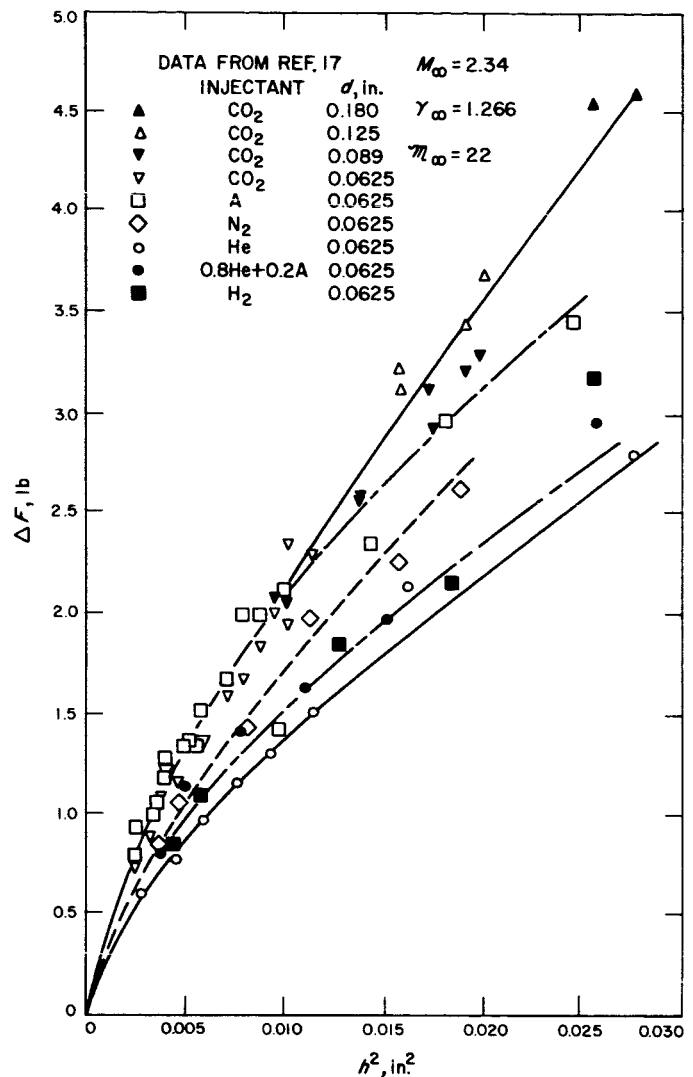


Fig. 58. Correlation of rocket-motor thrust-vector-control data (from Ref. 17), present method

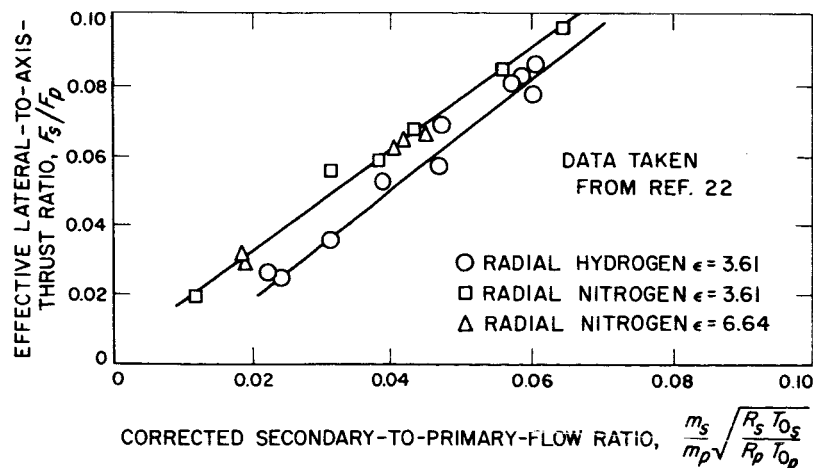


Fig. 57. Correlation of rocket-motor thrust-vector-control data (from Ref. 22)

Ref. 17, particularly at the higher injection rates (see Fig. 59). Figure 59 also includes data for subsonic injection, but does not include the effect of injector-port diameter. In another figure of Ref. 23, Broadwell shows a correlation of this effect, which is as good as that in Fig. 59.

Because of the disagreement between the various sets of experimental data of Ref. 17, 21, and 22, it is difficult to judge the value of the present technique in correlating rocket-motor data for different gaseous injectants. Both the technique proposed by Broadwell and that proposed by the authors appear to be in approximate agreement with experimental data, although both techniques predict greater increases in performance with decreasing molecular weight of injectant than are actually realized.

In the case of the technique developed here, the explanation for this discrepancy is believed to be as follows. The assumption of isentropic expansion of the

secondary flow appears to be quite satisfactory in the vicinity of the injector. However, it has been demonstrated for gaseous injection into a rocket exhaust that in many configurations, a major portion of the side force is developed quite far downstream of the injector. The concentration and total-pressure measurements presented in this Report show that mixing of the injectant with the free stream is quite rapid, and that the speed of the injected gas downstream of the injector is strongly affected by the free-stream flow. The effective scale of the obstruction downstream of the injector will then be less than that predicted by Eq. (6) if the speed of the injectant corresponding to an isentropic expansion to the free-stream static pressure is significantly greater than the speed of the free stream. This effect of mixing will then result in lower performance for a light gas than for a heavy gas when the gases are compared at the same value of the scale parameter h for rocket-nozzle injection configurations for which the side-force contribution downstream of the injector is important.

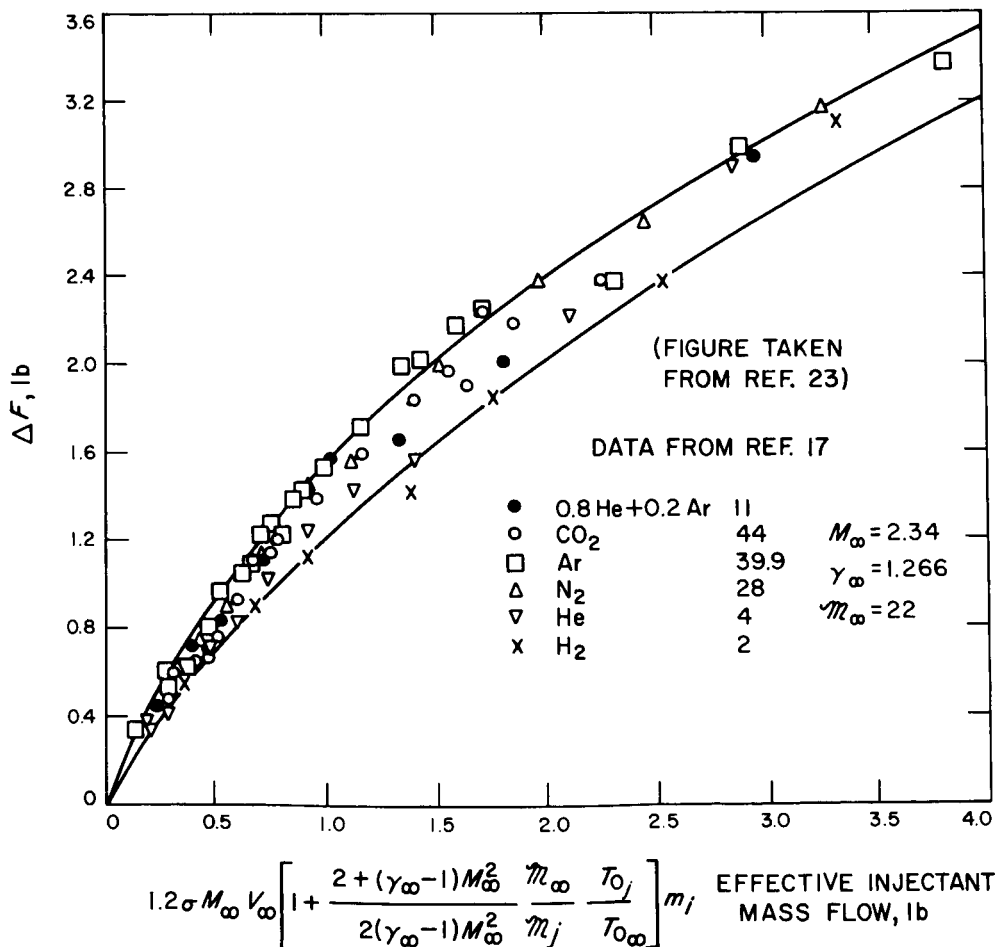


Fig. 59. Correlation of rocket-motor thrust-vector-control data, method of Broadwell (from Ref. 23)

NOMENCLATURE

A_j	injector area	Re_L	Reynolds number based on distance between leading edge of plate and injector centerline
c	discharge coefficient	R_i	gas constant for species i
C_D	drag coefficient	T	static temperature
C_p	pressure coefficient, $\{(P - P_\infty)/(1/2) \rho_\infty V^2\}$	T_0	stagnation temperature
C_p^*	pressure coefficient at the stagnation point [see Eq. (1)]	V	velocity
d	hole diameter or slot width	X	axial distance from injector port to nozzle exit (see Fig. 55)
D	probe diameter (see Fig. 11a)	x	} coordinate axes (see Fig. 3)
F_i	force on body surface in i direction	y	
F_j	thrust of a sonic injectant jet	z	
F_p	total axial thrust of the primary stream	Z_s	z coordinate of bow shock in x - z plane (see Fig. 10a and 10b)
F_s	total side thrust	α	angle between body surface and free-stream flow
h	scale height	γ	specific heat ratio
I_s	effective specific impulse of injectant, F_s/m_j	δ	boundary-layer separation angle
K_A	mass fraction of argon	ΔF	$F_s - F_j$
K_{He}	mass fraction of helium	ε	ratio of nozzle area at injection station to nozzle-throat area
M_i	Mach number	θ	$\pi/2 - \alpha$ (see Fig. 46)
m	mass flow rate	σ	parameter from blast-wave theory (Ref. 14 and 22)
M_i	molecular weight of i th species	Φ	dimensionless pressure integral, defined in Eq. (12)
P	static pressure	ψ	dimensionless pressure integral, defined in Eq. (29)
P_0	stagnation pressure	Subscripts	
R	distance, in y - z plane, to bow shock from the line ($z = h, y = 0$)	j	injectant
		∞	primary stream
		p	conditions in primary rocket flow

REFERENCES

1. Puckett, Allan, E., *Final Report, Model Supersonic Wind Tunnel Project*, GALCIT Report No. 40, California Institute of Technology, Pasadena, Calif., 1943.
2. Burden, H. W., *Some Effects of Secondary Injection into a Supersonic Flow*, A. E. Thesis, Graduate Aeronautical Laboratories, California Institute of Technology, Pasadena, Calif., June 1964.
3. Dowdy, M. W., and Newton, J. F., Jr., *Investigation of Liquid and Gaseous Secondary Injection Phenomena on a Flat Plate with $M = 2.01$ to $M = 4.54$* , Technical Report No. 32-542, Jet Propulsion Laboratory, Pasadena, Calif., December 23, 1963.
4. Wind Tunnel Staff of the Jet Propulsion Laboratory, *Wind Tunnel Facilities at the Jet Propulsion Laboratory*, Technical Release No. 34-257, Jet Propulsion Laboratory, Pasadena, Calif., January 1, 1962.
5. Amick, J. L., and Hayes, P. B., *Interaction Effects of Side Jets Issuing From Flat Plates and Cylinders Aligned with a Supersonic Stream*, Technical Report No. 60-329, Wright Air Development Division, Wright-Patterson Air Force Base, Ohio, June 1960.
6. Spaid, F. W., *A Study of Secondary Injection of Gases Into a Supersonic Flow*, PhD Thesis, California Institute of Technology, Pasadena, Calif., 1964.
7. Lees, L., "Hypersonic Flow," *Proceedings of the 5th International Aerospace Conference*, Los Angeles, Institute of the Aerospace Sciences, New York, 1955, pp. 241-276.
8. Keffer, J. F., and Baines, W. D., "The Round Turbulent Jet in a Cross-Wind," *Journal of Fluid Mechanics*, Vol. 15, No. 4, April 1963, pp. 481-496.
9. Cubbison, R. W., Anderson, B. H., and Ward, J. J., *Surface Pressure Distributions With a Sonic Jet Normal to Adjacent Flat Surfaces at Mach 2.92 to 6.4*, NASA TN D-580, National Aeronautics and Space Administration, Washington, D. C., February 1961.
10. Janos, J. J., *Loads Induced on a Flat-Plate Wing by an Air Jet Exhausting Perpendicularly Through the Plate and Normal to a Free-Stream Flow of Mach Number 2.0*, NASA TN D-649, National Aeronautics and Space Administration, Washington, D. C., March 1961.
11. Letko, W., *Loads Induced on a Flat Plate at a Mach Number of 4.5 With a Sonic or Supersonic Jet Exhausting Normal to the Surface*, NASA TN D-1935, National Aeronautics and Space Administration, Washington, D. C., July 1963.
12. Vinson, P. W., Amick, J. L., and Liepmann, H. P., *Interaction Effects Produced by Jet Exhausting Laterally Near Base of Ogive-Cylinder Model in Supersonic Main Stream*, NASA Memo 12-5-58W, National Aeronautics and Space Administration, Washington, D. C., February 1959.
13. Wu, J. M., Chapkis, R. L., and Mager, A., "Approximate Analysis of Thrust Vector Control by Fluid Injection," *ARS Journal*, Vol. 31, No. 12, December 1961, pp. 1677-1685.

REFERENCES (Cont'd)

14. Broadwell, J. E., *An Analysis of the Fluid Mechanics of Secondary Injection for Thrust Vector Control (Revised)*, Report No. 6120-7744-MU-00, Space Technology Laboratories, Inc., Redondo Beach, Calif., March 15, 1962.
15. Ferrari, C., *Interference Between a Jet Issuing Laterally From a Body and the Enveloping Supersonic Stream*, Bumblebee Report No. 286, Johns Hopkins University, Applied Physics Lab., Baltimore, Md., April 1959.
16. Newton, J. F., Jr., and Spaid, F. W., *Experiments on the Interaction of Secondary Injectants and Rocket Exhaust for Thrust Vector Control*, Technical Report No. 32-203, Jet Propulsion Laboratory, Pasadena, Calif., February 12, 1962; also in *ARS Journal*, Vol. 32, No. 8, August 1962, pp. 1203-1211.
17. Walker, R. E., Stone, A. R., and Shandor, M., "Secondary Gas Injection in a Conical Rocket Nozzle, I. Effect of Orifice Diameter and Molecular Weight of Injectant," *AIAA Journal*, Vol. 1, No. 2, February 1963, pp. 334-338.
18. Chernyi, G. G., *Introduction to Hypersonic Flow*, R. F. Probstein, ed., Academic Press, New York, 1961.
19. Vas, I. E., and Bogdonoff, S. M., *Interaction of a Turbulent Boundary Layer With a Step at $M = 3.85$* , TN 55-200, Air Force Office of Scientific Research, Washington, D. C., April 1955.
20. Rodriguez, C. J., *An Experimental Investigation of Jet-Induced Thrust Vector Control Methods*, paper presented at the 17th Annual JANAF-ARPA-NASA Solid Propellant Meeting, Denver, Colorado, May 23-25, 1961.
21. Lingen, A., *Jet-Induced Thrust-Vector Control Applied to Nozzles Having Large Expansion Ratios*, Report R-0937-33, United Aircraft Corp., Research Dept., East Hartford, Conn., March 1, 1957.
22. Chamay, A. J., and Sederquist, R. A., *An Experimental Investigation of Shock Vector Control With Gaseous Secondary Injection*, ARS Preprint 2216-61, American Rocket Society, New York, August 1961.
23. Broadwell, J. E., "Correlation of Rocket Nozzle Gas Injection Data," *AIAA Journal*, Vol. 1, No. 8, August 1963, pp. 1911-1913.